
**Mathematical modeling of
micro-textured lubricated contacts**

Alfredo Del Carmen Jaramillo Palma

SERVIÇO DE PÓS-GRADUAÇÃO DO ICMC-USP

Data de Depósito:

Assinatura: _____

Alfredo Del Carmen Jaramillo Palma

Modelação matemática de contatos lubrificados micro-texturizados

Dissertação apresentada ao Instituto de Ciências
Matemáticas e de Computação - ICMC-USP, como
parte dos requisitos para obtenção do título de
Mestre em Ciências - Ciências de Computação e
Matemática Computacional. *VERSÃO REVISADA.*

Área de Concentração: Ciências de Computação e
Matemática Computacional.

Orientador: Prof. Dr. Gustavo Carlos Buscaglia.

USP – São Carlos
Julho de 2015

Ficha catalográfica elaborada pela Biblioteca Prof. Achille Bassi
e Seção Técnica de Informática, ICMC/USP,
com os dados fornecidos pelo(a) autor(a)

J37m Jaramillo Palma, Alfredo Del Carmen
Mathematical modeling of micro-textured
lubricated contacts / Alfredo Del Carmen Jaramillo
Palma; orientador Gustavo Carlos Buscaglia. -- São
Carlos, 2015.
129 p.

Dissertação (Mestrado - Programa de Pós-Graduação
em Ciências de Computação e Matemática
Computacional) -- Instituto de Ciências Matemáticas
e de Computação, Universidade de São Paulo, 2015.

1. Textured surfaces. 2. Reynolds equation. 3.
Friction reduction. 4. Cavitation. 5. Numerical
simulation. I. Buscaglia, Gustavo Carlos , orient.
II. Título.

SERVIÇO DE PÓS-GRADUAÇÃO DO ICMC-USP

Data de Depósito:

Assinatura: _____

Alfredo Del Carmen Jaramillo Palma

Mathematical modeling of micro-textured lubricated contacts

Master dissertation submitted to the Instituto de Ciências Matemáticas e de Computação - ICMC-USP, in partial fulfillment of the requirements for the degree of the Master Program in Computer Science and Computational Mathematics. *FINAL VERSION.*

Concentration Area: Computer Science and Computational Mathematics.

Advisor: Prof. Dr. Carlos Gustavo Buscaglia.

USP – São Carlos
July 2015

Para Ida y Victor...

Acknowledgements (Agradecimientos)

Agradezco a mis padres, quienes a la distancia me han apoyado durante este proceso, como durante toda mi vida; a Paola, por su cariño, paciencia y apoyo; a Hugo Checo, colega de pesquisa, y al profesor Mohammed Jai, por su ayuda y disposición; a Gustavo Buscaglia, mi orientador, por compartir su visión científica y su paciencia; al profesor Sérgio Monari, por su ayuda en el estudio de EDP elípticas. Finalmente, agradezco a las agencias CAPES (Coordenação de Aperfeiçoamento de Pessoal de Nível Superior, processo DS-8434433/M) y CNPQ (Conselho Nacional de Desenvolvimento Científico e Tecnológico, processo 134105/2013-3), que apoyaron económicamente este trabajo de maestría.

“...La copa se hundió en el sol. Recogió un poco de la carne de Dios, la sangre del universo, el pensamiento deslumbrante, la enceguecedora filosofía que había amamantado a una galaxia, que guiaba y llevaba a los planetas por sus campos y emplazaba o acallaba vidas y subsistencias ...”

Las doradas manzanas del sol, Ray Bradbury.

Resumo

No desenho de mecanismos lubrificados, tais como Mancais hidrodinâmicos ou anéis de pistões de Motores a Combustão, atrito e desgaste são efeitos não desejados. Por exemplo, é sabido que aproximadamente 5% da energia perdida em um motor a combustão esta associada ao atrito presente no sistema de anéis/cilindro do pistão. Após vários trabalhos experimentais e teóricos, as superfícies texturizadas hão mostrado serem capazes de reduzir o atrito em algumas condições de funcionamento. O estudo da relação entre o atrito e os parâmetros de texturização é um problema difícil e de interesse tanto industrial como acadêmico. O contexto matemático e computacional destes trabalhos apresentam desafios por si mesmos, como o estudo da boa colocação dos modelos matemáticos, a consideração adequada das descontinuidades das superfícies. Este trabalho enfoca-se no contexto matemático, apresentando e estudando a equação de Reynolds junto com diferentes modelos de cavitação que podem encontrar-se na literatura. Começamos estudando a matemática da equação de Reynolds. Depois disso, modelos de cavitação são inclusos, aumentando a complexidade da matemática envolvida. Seguidamente, como aplicação da teoria apresentada, um rolamento deslizante será estudado junto com uma texturização da superfície móvel. Os resultados deste estudo revelam mecanismos básicos de redução de atrito e propriedades gerais que não haviam sido reportadas anteriormente. Possíveis trabalhos futuros são apresentados, tal como o uso de Métodos Descontínuos de Galerkin em vez dos Métodos de Volumes Finitos. O último em procura de uma melhor acomodação da formulação matemática, tentando melhorar a flexibilidade da malha e a precisão.

Palavras-chave: superfícies texturizadas, Equação de Reynolds, redução de atrito, cavitação, simulação numérica.

Abstract

In the design of lubricated mechanisms, such as Journal Bearings or Piston Rings of Combustion Engines, friction and wear are undesirable effects. It is known, for instance, that about 5% of the energy loss in a Combustion Engine is associated to friction taking place in the Piston Rings/Cylinder system. Textured surfaces, after a significant number of experimental and theoretical studies, have shown to reduce friction in some operating conditions. The study of the relation between the friction and the texture parameters is a challenging problem with both industrial and academic interest. The mathematical and computational frameworks involved present challenges by themselves, such as establishing the well-posedness of the mathematical models with suitable consideration of discontinuous surfaces. In this work we focus on the mathematical framework, presenting and studying the Reynolds equation along with different state-of-the-art cavitation models. We begin by studying the Reynolds equation and then incorporate two different cavitation models of increasing mathematical complexity. Next, as an application of the theory already presented, a slider bearing is numerically studied considering a sinusoidal texture on the runner. The results of this study unveil basic mechanisms of friction reduction and global quantitative trends that had not been previously reported. In this way, the applicability of numerical tools for texture selection is established. Future research directions are also identified, such as using Discontinuous Galerkin methods instead of Finite Volume Methods, aiming at improving the mesh flexibility and thus the accuracy of the discrete formulation.

Keywords: textured surfaces, Reynolds equation, friction reduction, cavitation, numerical simulation.

Contents

Acknowledgements (Agradecimientos)	viii
Abstract	x
Contents	xii
List of Figures	xvii
List of Tables	xix
List of Algorithms	xxi
Symbols	xxii
1 Motivation and scope of this manuscript	1
1.1 Representative Lubricated systems	2
1.2 Lubrication regimes	3
1.2.1 Hydrodynamic Lubrication	5
1.2.2 Elastohydrodynamic Lubrication	5
1.2.3 Boundary Lubrication	5
1.2.4 Mixed Lubrication	5
1.2.5 Fully-flooded and starving conditions	5
1.3 Lubrication Theory Hypothesis	6
2 The equations of lubrication	9
2.1 Lubrication Hypothesis in Navier-Stokes equation	9
2.2 Reynolds Equation	11
2.3 Friction forces	13
2.4 Comparison with Navier-Stokes equations	16
2.4.1 Reynolds and Stokes roughness	16
2.4.2 Numerical comparison addressing a sinusoidal texture case	16
2.5 Some representative analytic solutions	22
2.5.1 Step wedge and Rayleigh step	22
2.5.2 Disc wedge	27
3 Mathematics of Reynolds equation	31
3.1 From Stokes equations to Reynolds equation	31

3.2 Weak formulation for Reynolds equation	36
3.2.1 Stability Analysis	39
3.2.2 Spatial regularity	41
3.3 Maximum Principle for Reynolds equation	41
4 Cavitation and cavitation models	45
4.1 Basic cavitation physics	45
4.2 Reynolds model	46
4.2.1 Variational Formulation for Reynolds cavitation model	48
4.3 Mass conservation in cavitation models	53
4.4 Elrod-Adams model	55
4.5 Analytical solution examples	58
4.5.1 Cavitation in Pure Squeeze Motion	58
4.5.2 Cavitation in a flat pad with a traveling pocket	62
5 Numerical methods and illustrative examples	71
5.1 Finite volume discretization	71
5.2 Numerical implementation of Reynolds equation and cavitation models .	73
5.2.1 Reynolds equation without cavitation	73
5.2.2 Reynolds model	80
5.2.3 Elrod-Adams model	81
5.3 Numerical solution examples	82
5.3.1 Numerical solution to the analytic examples	83
5.3.2 Incorporating dynamics	86
6 Application: a study of sinusoidal textured slider bearings	91
6.1 Introduction	91
6.2 Simulation details and untextured cases	92
6.2.1 Quantities of interest	94
6.2.2 Untextured cases	95
6.3 Textures effects	96
6.3.1 General observations	97
6.3.2 An effect of the traveling bubbles	97
6.3.3 Hysteresis of the slider	98
6.3.4 Cavitation induced oscillations	99
7 Conclusions and future work	101
A Second order MAC scheme for Navier-Stokes equations	105
A.1 Discretization of advection and diffusion	106
A.2 Projection Method	108
B Mathematical background	111
B.1 Duality and Reflexivity	112
B.2 Hilbert Spaces	112
B.3 L^p spaces	114
B.4 Sobolev Spaces	115

Bibliography	123
--------------	------------

List of Figures

1.1	Journal Bearing scheme	3
1.2	Piston-Ring contact scheme	4
1.3	Surface roughness scheme	4
1.4	Conformity of the circular-shaped slider bearing	4
1.5	Starved and fully-flooded conditions example.	6
2.1	Two parallel lubricated surfaces scheme	9
2.2	Channel Problem scheme	12
2.3	2D surface normal orientations scheme	15
2.4	An infinite 1D bearing with a sinusoidal texture.	17
2.5	Dimensionless pressure from Navier-Stokes equations and from Reynolds equation for different Reynolds number.	20
2.6	Dimensionless pressure from Navier-Stokes equations and Reynolds equation for different depths.	20
2.7	Dimensionless pressure differences (absolute and relative) between Reynolds and Navier Stokes Equations with different Reynolds number	21
2.8	Relative differences in friction between Reynolds and Navier Stokes Equations with several Reynolds number for the correct and wrong formulas	21
2.9	Step wedge pad scheme.	23
2.10	Scheme of the “naive step wedge” versus the Rayleigh Step wedge	26
2.11	Disc pad scheme.	27
2.12	Disc pad scheme and pressure profile.	29
3.1	Domain dependent on ϵ for studying the convergence of Stokes system solutions.	32
3.2	Disc pad scheme and pressure profile.	42
4.1	Illustration of gaseous cavitation	46
4.2	Scheme of a solution using Half-Sommerfeld cavitation model.	47
4.3	Obstacle problem for an elastic membrane.	48
4.4	2D cavitating domain scheme.	53
4.5	1D rupture and reformation scheme with Reynolds model	54
4.6	1D rupture and reformation scheme with Elrod-Adams model	57
4.7	Pure Squeeze problem scheme.	58
4.8	Characteristic lines for Pure Squeeze Motion	60
4.9	Comparison of cavitation models for a Pure Squeeze problem	61
4.10	Scheme of the rectangular wedges problem	62
4.11	Scheme of the solution for a single honed pocket without cavitation.	63

4.12	Scheme of an ansatz solution for a single honed pocket with Reynolds cavitation model.	64
4.13	Characteristics lines of the transport equation of $h\theta$	67
4.14	Initial conditions of θ and p for the problem of a traveling pocket	67
4.15	Characteristic lines to find $\theta_+(\beta)$	68
4.16	Analytic solutions of Elrod-Adams and Reynolds cavitation models for three different times of the traveling pocket	69
5.1	Finite volume control	73
5.2	Scheme of flux functions 1D.	74
5.3	Convergence of the numerical solution for the Disc wedge presented in Section §2.5.2.	79
5.4	Numerical solution of the cavitation boundary for Elrod-Adams model with $N = 100, 450$	84
5.5	Numerical solution of the cavitation boundary for Reynolds model with $N = 100, 450$	84
5.6	Numerical ($N=450$) and analytic solution of the saturation θ for $t = 0.3146$, just before the reformation time t_{ref}	85
5.7	Analitic solutions of Elrod-Adams and Reynolds cavitation models for three different times as done in Section §4.5.2	85
5.8	Convergence analysis for p and θ in the $H_0^1(0, 1)$ and $L^2(0, 1)$ norms resp. for the traveling pocket problem solved in Section §4.5.2.	86
5.9	Scheme of the rectangular wedges problem	86
5.10	Profiles of p and θ for different time instants with dynamic behavior of the slider	89
6.1	Slider bearing over and a sinusoidal textured runner scheme.	91
6.2	Slider evolution for the untextured case for load W^a and $R = 32$	95
6.3	Comparison of C_{\min} and \bar{f} for several values of λ and d by relative differences V_f (left side) and V_C (right side) for $R=32, 256$ (upper and lower figures resp.).	96
6.4	Sudden change of p and θ with a small change of d and λ fixed	97
6.5	Hysteresis of the statationary state.	98
6.6	Hydrodynamic force and slider position oscillations induced by sudden cavitation bubbles collapse	99
A.1	Staggered MAC discretization scheme	106
A.2	Staggered MAC control volumes for velocities	107

List of Tables

2.1	Non-dimensional variables for the stationary Reynolds equation (2.32)	18
2.2	Non-dimensional variables for the step wedge problem.	22
2.3	Non-dimensional variables for the disc wedge problem.	28
5.1	Convergence of the truncation errors and global error for the numerical example of the Disc wedge.	79
5.2	Basic and derived scales for traveling pocket with dynamic behavior of the slider	88
6.1	Basic and derived scales for the dynamic slider with sinusoidal textures.	93
6.2	Friction coefficient \bar{f} and clearance C_{\min} for several values of R once they reached the stationary state.	95

List of Algorithms

1	Gauss-Seidel for Reynolds equation	80
2	Gauss-Seidel for Reynolds equation with Reynolds cavitation model	81
3	Gauss-Seidel for Reynolds equation with Elrod-Adams cavitation model	83
4	Dynamic Gauss-Seidel for Reynolds equation with Elrod-Adams cavitation model	90

Symbols

$\partial\Omega$	Boundary of the domain Ω
$\mathring{\Omega}$	Topological interior of Ω
$\overline{\Omega}$	Closure of Ω : $\overline{\Omega} = \partial\Omega \cup \Omega$
$C^0(\Omega)$	Set of continuous functions over Ω
$C^k(\Omega)$	Set of functions over Ω having all derivatives of order $\leq k$ continuous in Ω
$C^\infty(\Omega)$	Set of infinitely differentiable functions over Ω
$C_0^k(\Omega)$	Functions in $C^k(\Omega)$ with compact support
$C_0^\infty(\Omega)$	Functions in $C^\infty(\Omega)$ with compact support
C_B^j	$\{u \in C^j(\Omega) : \partial^\alpha u \text{ is bounded for } \alpha \leq j\}$
$L^1(\Omega)$	Lebesgue integrable functions on Ω
$L^q(\Omega)$	$f : \Omega \rightarrow \mathbb{R}$ is in $L^q(\Omega)$ if $ f ^q \in L^1(\Omega)$
$H^1(\Omega)$	Sobolev space of functions in $L^2(\Omega)$ with first order weak derivatives in $L^2(\Omega)$
$H^{-1}(\Omega)$	Dual space of $H^1(\Omega)$
$\mathcal{D}'(\Omega)$	Dual space of $C_0^\infty(\Omega)$
∂_x	Denotes the operator $\frac{\partial}{\partial x}$
∇	∇f is the vector with components $\partial_x f$ for each Cartesian coordinate
∇^2	Denotes the Laplacian operator $\sum_{i=1}^N \frac{\partial^2}{\partial x_i^2}$. N is the dimension of the problem.

Chapter 1

Motivation and scope of this manuscript

For many mechanical systems, designers deal with the proximity of surfaces in relative motion in such a way that *wear* and *friction* appear. In general, to prevent such undesirable effects, some substance (e.g., oil, grease, gas) is suitably placed to carry part of the applied load. This way of addressing wear and friction is called *lubrication* and the science that studies wear, friction and lubrication is called *Tribology*.

In the last ten years, novel fabrication techniques have opened the possibility of tailoring surfaces at micrometric scale [38]. Precision micromachining and high energy pulsed lasers can engrave surfaces with micrometric motifs of practically any shape. Envisioning large potential gains, industry has been promoting the scientific exploration of engineered surfaces, designed so as to improve the friction, wear, stiction and lubricant consumption characteristics of tribological systems. In fact, Holmberg [56] showed that between 5 and 10% of a passenger car power is lost due to friction on the Piston-Ring System (see Figure 1.2) and thus the better understanding of how engineered surfaces work in those systems may have a great socio-economic impact.

For helping designers and engineers in the elaboration of efficient tribological systems, computational simulations are need to provide insight on the dependence of those systems on their design variables. However, not only the analysis of simulation results would be required but also the improvement of the mathematical models of the physics involved and the numerical methods related to it. With this motivation, this work addresses the mathematical models and numerical methodologies involved in Lubrication Theory.

Apart from this mathematical study, simple tribological systems, such as the slider bearing, were simulated and the results are exposed and analyzed. For these simulations, an in-house computational program was used. Its source file can be found at www.lcad.icmc.usp.br/~buscaglia/download.html.

Next, the structure of this document is summarized:

Chapter 1 The scope of the work is given along with the description of some basic tribological systems and some basic definitions of Lubrication Theory.

Chapter 2 The Reynolds equation and the friction formulas are deduced from a simple asymptotic analysis. Also, results of both Navier-Stokes equations and Reynolds equation are compared.

Chapter 3 Mathematical properties of the Reynolds equation are studied, showing well-posedness (*existence, uniqueness* and *stability*) under the hypothesis of no cavitation.

Chapter 4 Cavitation is considered and different mathematical models of it are presented and analyzed along with some analytical solutions.

Chapter 5 Numerical methods for Reynolds equation and cavitation models are studied and some numerical solutions are shown.

Chapter 6 A set of simulations are performed for the slider bearing tribological system. Considering sinusoidal textures, the effects of several textures are measured and some effects are presented when considering the Elrod-Adams cavitation model (presented in Chapter 4).

Chapter 7 Conclusions and future work are presented.

1.1 Representative Lubricated systems

Journal Bearing (see Figure 1.1) This system consists of a rotating cylindrical shaft (journal) enclosed by a cylindrical bush. The journal adopts an eccentric position that creates a convergent-divergent profile for the fluid and in this way generates pressure. This pressure, when integrated in the axial and circumferential directions, yields the *load-carrying capacity* of the journal.

Piston-Ring (see Figure 1.2) This system performs different important functions: the Top Ring provides a gas seal and the Second Ring below assists in the sealing and adjusts the action of the oil film. The rings also act carrying heat into the

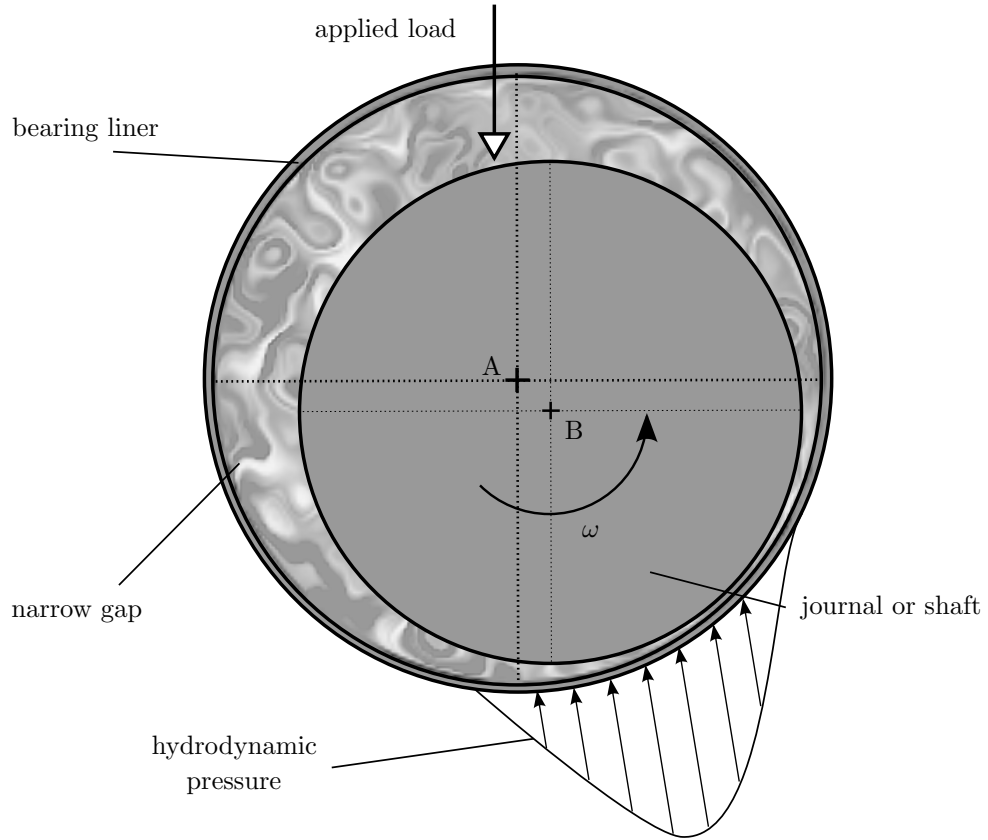


FIGURE 1.1: Journal Bearing scheme. Point A is the bush center (fixed). Point B is the center of the journal (dynamically varying). The journal is rotating with angular speed ω .

cooled cylinder wall (liner). This heat transfer function maintains acceptable temperatures and stability in the piston and piston rings, so that sealing ability is not impaired. Finally, the Oil Control Ring (OCL) acts in a scrapping manner, keeping excess oil out of the combustion chamber. In this way, oil consumption is held at an acceptable level and harmful emissions are reduced.

1.2 Lubrication regimes

This work is focused in fluid film lubrication phenomena, which take place when opposing surfaces are separated by a lubricant film. We characterize the roughness of the surfaces by a parameter σ that is the *composite standard deviations of asperity height distribution*, given by $\sigma = \sqrt{\sigma_1^2 + \sigma_2^2}$ [69]. For characterizing the distance between the surfaces we denote as \bar{h} the average distance between them. Both parameters σ and \bar{h} are schematized in Figure 1.3.

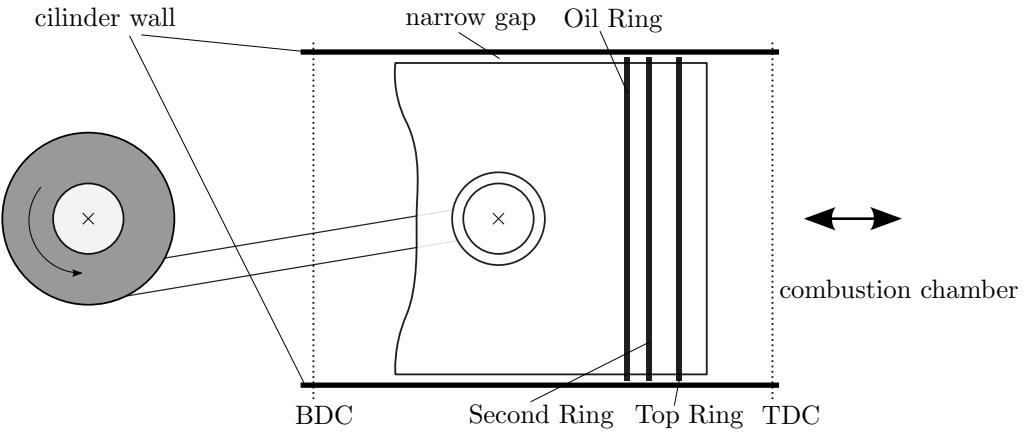


FIGURE 1.2: Piston-Ring contact scheme. The piston has an oscillatory motion between the TDC (Top Dead Center) and BDC (Bottom Dead Center) points.

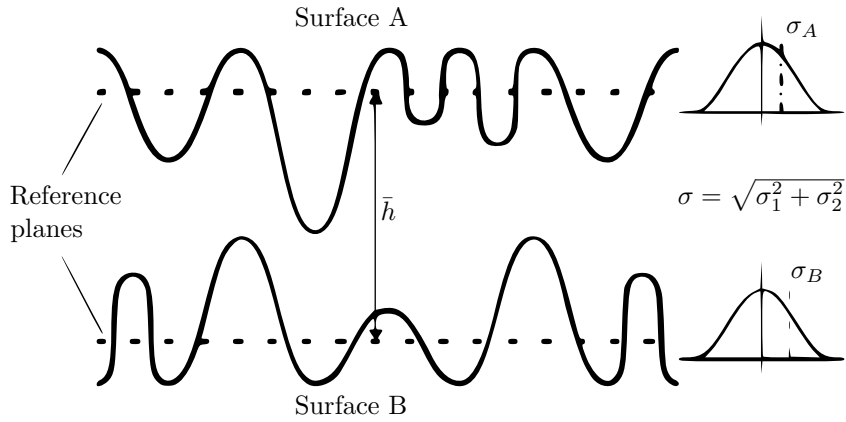


FIGURE 1.3: Surface roughness scheme. Adapted from [69].

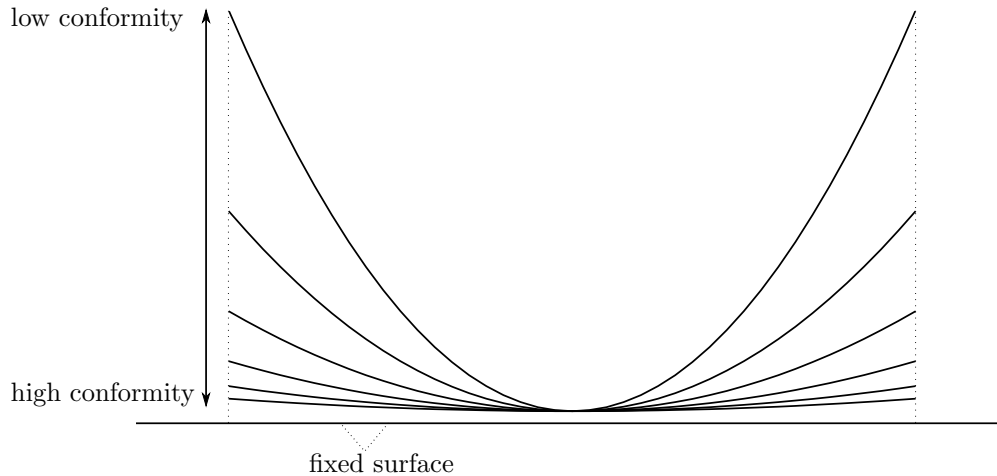


FIGURE 1.4: Conformity is a measure relating the curvatures of two surfaces in proximity. Adapted from [21].

Another important measure of surfaces in proximity is its degree of *conformity*. Roughly speaking, we say that two surfaces are conformal if their curvatures are similar. On the

contrary, the more dissimilar the curvatures are, the less conformal (see Figure 1.4). A more accurate use of this concept can be found in Chapter 6.

Depending on how effective the fluid film is for separating the surfaces, the next classification arises:

1.2.1 Hydrodynamic Lubrication

In this case the fluid film separates the surfaces completely. Moreover, the generated pressure is low enough to prevent the deformation of the surfaces. In this regime there is no direct contact between the surfaces.

1.2.2 Elastohydrodynamic Lubrication (EHL)

As in Hydrodynamic Lubrication, in EHL the surfaces are completely separated ($\bar{h} \gg \sigma$). In contrast, the pressure field deforms the surfaces. Material hardness and dependence of viscosity on temperature play important roles.

1.2.3 Boundary Lubrication

This case ($\bar{h} \approx \sigma$) is associated with the highest levels of friction and wear due to direct contact between the surfaces. These (normal) contact forces are calculated with some model like the Greenwood-Williamson model [52, 69]. Some *dry friction coefficient* C_f is used to calculate the contact friction force as $F = C_f N$.

1.2.4 Mixed Lubrication

As the name would suggest, Mixed Lubrication occurs between boundary and hydrodynamic lubrication. The fluid film thickness (\bar{h}) is slightly greater than the surface roughness (σ), so that asperity contacts are not as important as in Boundary Lubrication, but the surfaces are still close enough as to affect each other (e.g., surface deformations would take place).

1.2.5 Fully-flooded and starving conditions

In this work, the oil inflow rate Q is assumed to be high enough to assure Hydrodynamic Lubrication regime and, at the same time, allow the tribological properties to not depend

on Q (in the sense that if Q is augmented, the tribological properties will not change). We name this condition as *fully-flooded* condition.

Figure 1.5 shows a numerical experiment that illustrates starved and fully-flooded conditions. Focusing on Figure 1.5 a), the first red line from below represents a barrel-shaped

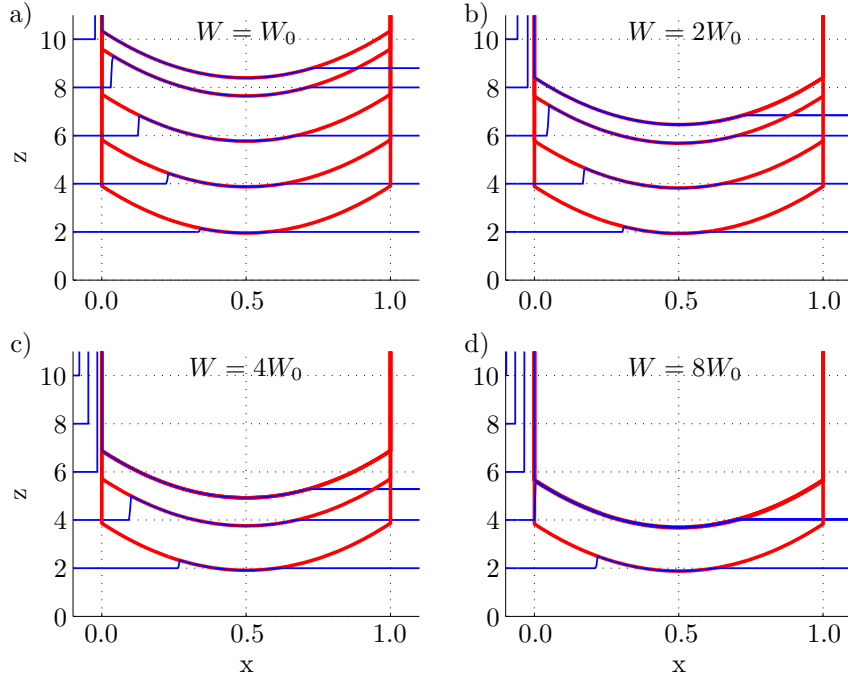


FIGURE 1.5: Starved and fully-flooded conditions example.

pad placed between $x = 0$ and $x = 1$ over which a vertical load of module $W = W_0$ is acting downwards. The pad, running to the left, is being separated from a second fixed surface placed along $z = 0$ by an oil film entering from the left, which height is represented by the blue line with height-entry $h_d = 2$. For this load and height-entry, the minimum distance C_{\min} from the pad to the lower surface is approximately $C_{\min} = 2$. When h_d is incremented C_{\min} rises also. Notice that this rising is accompanied with an augment of the area of contact between the fluid and the pad. As it can be observed from Figure 1.5 b) to d), for each h_d , the bigger is W the smaller is the minimal distance C_{\min} . For each of the showed cases, the steady state behavior of the pad does not changes if we choose $h_d \geq 10$. Thus, setting $h_d = 10$ we are assuring fully-flooded conditions for any load W chosen for this example.

1.3 Lubrication Theory Hypothesis

In Chapter 2 we derive Reynolds equation for hydrodynamic lubricated systems. Before doing so, the assumptions needed on the system are presented (see [18] Chapter 3):

1. Body forces, such as gravitational forces, are neglected, i.e., there are no extra fields of forces acting on the fluid. This is true except for magneto-hydrodynamics.
2. The pressure is constant through the thickness of the film.
3. The curvature of the surfaces being lubricated is large compared to the film thickness.
4. There is no slip at the boundaries. The velocity of the oil layer adjacent to the boundary is the same as that of the boundary. There has been much work on this and it is universally accepted [18]. Nevertheless, some works criticizing this condition have been done recently by Salant and Fortier [80, 42].

The next assumptions are put in for simplification. They are not necessarily true but without them the equations get more complex, sometimes impossibly so.

5. Flow is laminar.
6. Fluid inertia is neglected. For the studied cases, the Reynolds number is of order 10 (see Section §2.4).
7. The lubricant is Newtonian.

Chapter 2

The equations of lubrication

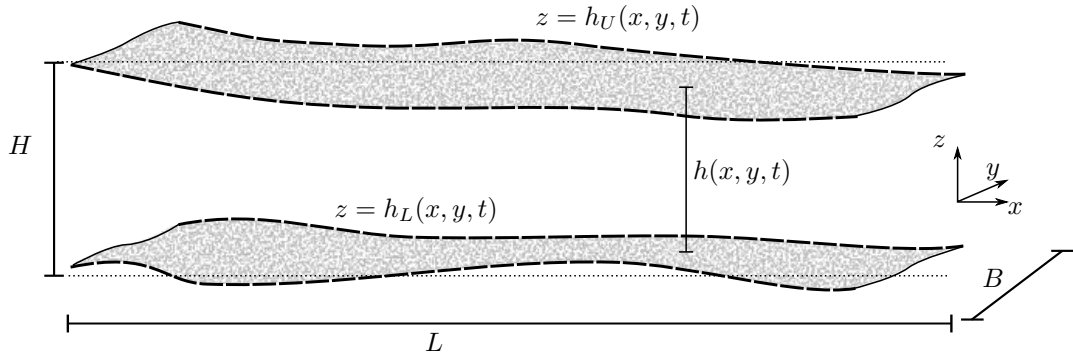


FIGURE 2.1: Proximity scheme of two lubricated surfaces.

Fluid film bearings are mechanisms that support loads on a thin layer of liquid or gas. Journal Bearings (Figure 1.1) and Piston Rings (Figure 1.2) are examples of fluid film bearings with rotating or reciprocating motion. The space between the surfaces (see Figure 2.1) is filled by fluid or gas, in order to avoid contact. The bearing dynamics is essential to predict the machine behavior under different operating conditions, such as different rotating speeds, applied loads or surface texturing. Therefore, the research for an accurate mathematical model of the motion equations is very important, and it has been part of several publications since Reynolds' pioneering work [77].

2.1 Lubrication Hypothesis in Navier-Stokes equation

As a particular case of lubrication, the case where the material between both surfaces is a lubricant oil is studied here. Moreover, the oil is assumed to be an incompressible Newtonian fluid, so it has associated some dynamic viscosity μ and a density ρ .

As the surfaces are very near each other, we suppose L , the characteristic length of the *longitudinal movement* (x direction) of the surfaces, as being much greater than H , which is the characteristic length of the *transverse movement* (z direction), i.e., $\epsilon = H/L \ll 1$ (typically $\epsilon \approx 10^{-3}$).

Denoting by $\vec{\mathbf{u}} = (u, v, w)^T$ the lubricant velocity and p its pressure, Navier-Stokes Equations for Newtonian fluids are valid, which can be written as

$$\rho \left(\frac{\partial \vec{\mathbf{u}}}{\partial t} + (\vec{\mathbf{u}} \cdot \nabla) \vec{\mathbf{u}} \right) = -\nabla p + \mu \nabla^2 \vec{\mathbf{u}} + \vec{\mathbf{f}}. \quad (2.1)$$

Also, we consider the boundary conditions $u(z = h_U) = U_H$, $u(z = h_L) = U_L$, $v(z = h_U) = V_H$ and $v(z = h_L) = V_L$,

$$\begin{aligned} w(z = h_U) = W_H &= \frac{\partial h_U}{\partial t} + U_H \frac{\partial h_U}{\partial x} + V_H \frac{\partial h_U}{\partial y}, \\ w(z = h_L) = W_L &= \frac{\partial h_L}{\partial t} + U_L \frac{\partial h_L}{\partial x} + V_L \frac{\partial h_L}{\partial y}, \end{aligned}$$

where we used that W_U can be written as the sum of a squeeze part $\partial h_U / \partial t$ and a shape part $U_H \cdot \partial h_U / \partial x$ (analogously for W_L).

Neglecting external forces $\vec{\mathbf{f}}$, the hypothesis of surfaces proximity is introduced by making the next non-dimensionalization

$$\hat{x} = \frac{x}{L}, \hat{y} = \frac{y}{L}, \hat{z} = \frac{z}{H}, \hat{u} = \frac{u}{U}, \quad (2.2)$$

$$\hat{v} = \frac{v}{U}, \hat{w} = \frac{w}{U \frac{H}{L}}, \hat{t} = \frac{t}{L}, \hat{p} = p \frac{H^2}{\mu L U}. \quad (2.3)$$

This way, we obtain

$$\begin{aligned} \rho \frac{U^2}{L} \left(\frac{\partial \hat{u}}{\partial \hat{t}} + \hat{u} \frac{\partial \hat{u}}{\partial \hat{x}} + \hat{v} \frac{\partial \hat{u}}{\partial \hat{y}} + \hat{w} \frac{\partial \hat{u}}{\partial \hat{z}} \right) &= -\frac{1}{L} \frac{\mu L U}{H^2} \frac{\partial \hat{p}}{\partial \hat{x}} \\ &\quad + \mu \left(\frac{U}{L^2} \frac{\partial^2 \hat{u}}{\partial \hat{x}^2} + \frac{U}{L^2} \frac{\partial^2 \hat{u}}{\partial \hat{y}^2} + \frac{U}{H^2} \frac{\partial^2 \hat{u}}{\partial \hat{z}^2} \right), \end{aligned} \quad (2.4)$$

$$\begin{aligned} \rho \frac{U^2}{L} \left(\frac{\partial \hat{v}}{\partial \hat{t}} + \hat{u} \frac{\partial \hat{v}}{\partial \hat{x}} + \hat{v} \frac{\partial \hat{v}}{\partial \hat{y}} + \hat{w} \frac{\partial \hat{v}}{\partial \hat{z}} \right) &= -\frac{1}{L} \frac{\mu L U}{H^2} \frac{\partial \hat{p}}{\partial \hat{y}} \\ &\quad + \mu \left(\frac{U}{L^2} \frac{\partial^2 \hat{v}}{\partial \hat{x}^2} + \frac{U}{L^2} \frac{\partial^2 \hat{v}}{\partial \hat{y}^2} + \frac{U}{H^2} \frac{\partial^2 \hat{v}}{\partial \hat{z}^2} \right) \end{aligned} \quad (2.5)$$

$$\begin{aligned} \rho \frac{U^2 H}{L^2} \left(\frac{\partial \hat{w}}{\partial \hat{t}} + \hat{u} \frac{\partial \hat{w}}{\partial \hat{x}} + \hat{v} \frac{\partial \hat{w}}{\partial \hat{y}} + \hat{w} \frac{\partial \hat{w}}{\partial \hat{z}} \right) &= -\frac{\mu L U}{H^3} \frac{\partial \hat{p}}{\partial \hat{z}} \\ &\quad + \mu \frac{U}{L} \left(\frac{H}{L^2} \frac{\partial^2 \hat{w}}{\partial \hat{x}^2} + \frac{H}{L^2} \frac{\partial^2 \hat{w}}{\partial \hat{y}^2} + \frac{1}{H} \frac{\partial^2 \hat{w}}{\partial \hat{z}^2} \right). \end{aligned} \quad (2.6)$$

Introducing the Reynolds Number $\text{Re} = \frac{\text{inertia}}{\text{viscous}} = \rho U H / \mu$ these equations can be written as

$$\begin{aligned}\frac{\partial \hat{p}}{\partial \hat{x}} &= \frac{\partial^2 \hat{u}}{\partial \hat{z}^2} - \epsilon \text{Re} \left(\frac{\partial \hat{u}}{\partial \hat{t}} + \hat{u} \frac{\partial \hat{u}}{\partial \hat{x}} + \hat{v} \frac{\partial \hat{u}}{\partial \hat{y}} + \hat{w} \frac{\partial \hat{u}}{\partial \hat{z}} \right) + O(\epsilon^2) \\ \frac{\partial \hat{p}}{\partial \hat{y}} &= \frac{\partial^2 \hat{v}}{\partial \hat{z}^2} - \epsilon \text{Re} \left(\frac{\partial \hat{v}}{\partial \hat{t}} + \hat{u} \frac{\partial \hat{v}}{\partial \hat{x}} + \hat{v} \frac{\partial \hat{v}}{\partial \hat{y}} + \hat{w} \frac{\partial \hat{v}}{\partial \hat{z}} \right) + O(\epsilon^2) \\ \frac{\partial \hat{p}}{\partial \hat{z}} &= -\epsilon^3 \text{Re} \left(\frac{\partial \hat{w}}{\partial \hat{t}} + \hat{u} \frac{\partial \hat{w}}{\partial \hat{x}} + \hat{v} \frac{\partial \hat{w}}{\partial \hat{y}} + \hat{w} \frac{\partial \hat{w}}{\partial \hat{z}} \right) + \epsilon^4 \left(\frac{\partial^2 \hat{w}}{\partial \hat{x}^2} + \frac{\partial^2 \hat{w}}{\partial \hat{y}^2} \right) + \epsilon^2 \frac{\partial^2 \hat{w}}{\partial \hat{z}^2} = O(\epsilon^2).\end{aligned}$$

Now, neglecting terms of order ϵ and higher (including inertial terms!) and returning to the original variables we obtain

$$\frac{\partial p}{\partial x} = \mu \frac{\partial^2 u}{\partial z^2} \quad (2.7)$$

$$\frac{\partial p}{\partial y} = \mu \frac{\partial^2 v}{\partial z^2}, \quad (2.8)$$

$$\frac{\partial p}{\partial z} = 0. \quad (2.9)$$

From equation (2.9) we deduce that the pressure p only depends upon x and y . Integrating two times on z between $z = h_L$ and $z = h_U$, we have:

$$u(z) = \frac{1}{2\mu} \frac{\partial p}{\partial x} (z - h_L)(z - h_U) + \frac{z - h_L}{h_U - h_L} U_H + \frac{h_U - z}{h_U - h_L} U_L, \quad (2.10)$$

$$v(z) = \frac{1}{2\mu} \frac{\partial p}{\partial y} (z - h_L)(z - h_U) + \frac{z - h_L}{h_U - h_L} V_H + \frac{h_U - z}{h_U - h_L} V_L. \quad (2.11)$$

Integrating the last equations for $z \in [h_L, h_U]$ the flux functions are obtained:

$$Q_x = \int_{h_L}^{h_U} u dz = -\frac{h^3}{12\mu} \frac{\partial p}{\partial x} + \frac{U_L + U_H}{2} h, \quad (2.12)$$

$$Q_y = \int_{h_L}^{h_U} v dz = -\frac{h^3}{12\mu} \frac{\partial p}{\partial y} + \frac{V_L + V_H}{2}, \quad (2.13)$$

where $h = h_U - h_L$. Figure 2.2 shows a scheme of the linear and quadratic terms written on equation (2.10). The linear one corresponds to a Couette flow, which is due to relative motion between the surfaces, while the second represents a Poiseuille flow, which is due to the presence of a pressure gradient.

2.2 Reynolds Equation

To obtain Reynolds Equation, we introduce the *continuity equation*, which in the incompressible case reads:

$$\nabla \cdot \vec{u} = 0, \quad (2.14)$$

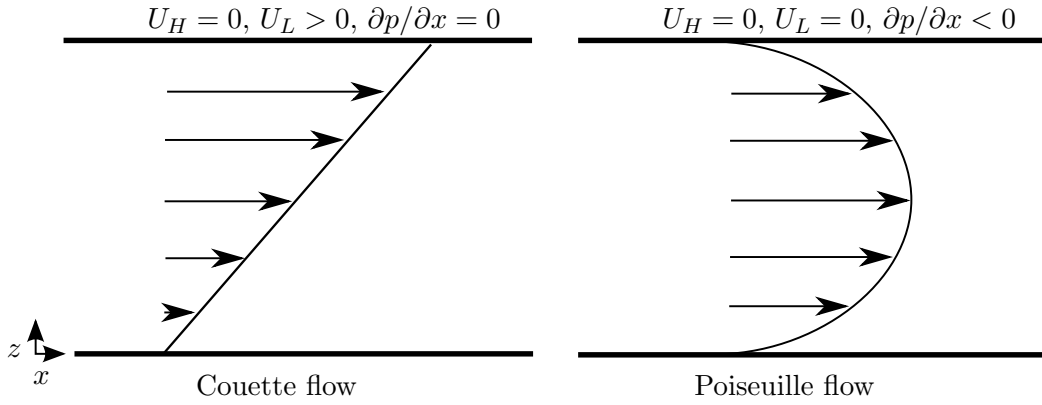


FIGURE 2.2: Couette and Poisseuille profile flows in a Channel.

integrating along z we obtain:

$$\int_{h_L(x,y,t)}^{h_U(x,y,t)} \left(\frac{\partial u}{\partial x} + \frac{\partial v}{\partial y} + \frac{\partial w}{\partial z} \right) dz = 0. \quad (2.15)$$

The first two integrals above can be calculated by using Leibniz's rule for time-dependent domains. By using equations (2.10) and (2.11), this is written as

$$\int_{h_L(x,y,t)}^{h_U(x,y,t)} \frac{\partial u}{\partial x} dz = \frac{\partial}{\partial x} Q_x - U_H \frac{\partial h_U}{\partial x} + U_L \frac{\partial h_L}{\partial x}, \quad (2.16)$$

$$\int_{h_L(x,y,t)}^{h_U(x,y,t)} \frac{\partial v}{\partial y} dz = \frac{\partial}{\partial y} Q_y - V_H \frac{\partial h_U}{\partial y} + V_L \frac{\partial h_L}{\partial y}. \quad (2.17)$$

Now, for the third integral we have:

$$\begin{aligned} \int_{h_L(x,y,t)}^{h_U(x,y,t)} \frac{\partial w}{\partial z} dz &= W_U - W_L \\ &= \frac{\partial h_U}{\partial t} + U_H \frac{\partial h_U}{\partial x} + V_H \frac{\partial h_U}{\partial y} - \left(\frac{\partial h_L}{\partial t} + U_L \frac{\partial h_L}{\partial x} + V_L \frac{\partial h_L}{\partial y} \right) \\ &= \frac{\partial h}{\partial t} + U_H \frac{\partial h_U}{\partial x} - U_L \frac{\partial h_L}{\partial x} + V_H \frac{\partial h_U}{\partial y} - V_L \frac{\partial h_L}{\partial y}, \end{aligned} \quad (2.18)$$

where $h = h_U - h_L$. Thus, summing equations (2.16), (2.17) and (2.18), equation (2.15) can be written as

$$\frac{\partial}{\partial x} Q_x + \frac{\partial}{\partial y} Q_y + \frac{\partial h}{\partial t} = \nabla \cdot Q + \frac{\partial h}{\partial t} = 0.$$

Finally, we replace the flux function $Q = [Q_x, Q_y]^T$ for the Newtonian case from equations (2.12) and (2.13) to obtain:

$$\frac{\partial}{\partial x} \left(\frac{h^3}{12 \mu} \frac{\partial p}{\partial x} - \frac{U_L + U_H}{2} h \right) + \frac{\partial}{\partial y} \left(\frac{h^3}{12 \mu} \frac{\partial p}{\partial y} - \frac{V_L + V_H}{2} h \right) = \frac{\partial h}{\partial t}, \quad (2.19)$$

which is known as Reynolds Equation in Lubrication Theory.

To simplify notation we assume $U_L = U$, $U_H = V_L = V_H = 0$, so Reynolds equation can be written in the conservative form

$$\frac{\partial h}{\partial t} + \nabla \cdot \vec{\mathbf{J}} = 0,$$

with

$$\vec{\mathbf{J}} = -\frac{h^3}{12\mu} \nabla p + \frac{U}{2} h \hat{\mathbf{e}}_1, \quad (2.20)$$

where $\hat{\mathbf{e}}_1$ is the unitary vector pointing positively in the x -axis. We say that $\vec{\mathbf{J}}$ corresponds to the *mass-flux* function.

2.3 Friction forces

Friction forces are some of the most important quantities to be analyzed in our study. The dependence of such forces on the design variables of tribological devices has been analyzed in several works during the last years [79, 86, 21, 64]. In this section, the formula that gives the total friction force over some surface, due to hydrodynamic pressure and viscosity effects, is calculated starting from the particular expression of the stress tensor under our working hypotheses.

For Newtonian incompressible fluids, the stress tensor $\boldsymbol{\tau}$, which gives the forces per unit area acting on a material surface, is given by the constitutive relation:

$$\tau_{ij} = -p \delta_{ij} + \mu \left(\frac{\partial u_i}{\partial x_j} + \frac{\partial u_j}{\partial x_i} \right), \quad (2.21)$$

where i and j are indices corresponding to the three Cartesian dimensions, and δ is the Kronecker delta. Since $\hat{\mathbf{n}}$ is a normal unit vector pointing outward from some surface, the force f exerted by the fluid over it in the direction $\hat{\mathbf{e}}$ is given by the projection of the total force $\vec{\mathbf{f}}$ on $\hat{\mathbf{e}}$:

$$f = \vec{\mathbf{f}} \cdot \hat{\mathbf{e}} = (\boldsymbol{\tau} \cdot \hat{\mathbf{n}}) \cdot \hat{\mathbf{e}} = \sum_{ij} \tau_{ij} \hat{n}_j \hat{e}_i = \sum_{ij} \tau_{ij} \hat{e}_j \hat{n}_i, \quad (2.22)$$

where the symmetry of $\boldsymbol{\tau}$ was used in the last equality. The *friction force* is a force opposing the motion when an object is moved or two objects are relatively moving [88]. To calculate the friction force, suppose the movement direction of a surface is given by the unit vector $\hat{\mathbf{i}}$ as in Figure 2.3. There, the lower surface is moving to the right so we

put $\hat{\mathbf{e}} = \hat{\mathbf{i}}$ and we get

$$\boldsymbol{\tau} \cdot \hat{\mathbf{i}} = \boldsymbol{\tau} \cdot \begin{pmatrix} 1 \\ 0 \\ 0 \end{pmatrix} = \begin{pmatrix} \tau_{xx} \\ \tau_{xy} \\ \tau_{xz} \end{pmatrix} = \begin{pmatrix} -p + 2\mu \frac{\partial u}{\partial x} \\ \mu \left(\frac{\partial u}{\partial y} + \frac{\partial v}{\partial x} \right) \\ \mu \left(\frac{\partial u}{\partial z} + \frac{\partial w}{\partial x} \right) \end{pmatrix}.$$

Using the proximity hypothesis, i.e., $\epsilon = H/L$ is very small, and the non-dimensionalizations equations (2.2) and (2.3) we get

$$\tau_{xx} = \mu \frac{U}{H} \left(-\frac{1}{\epsilon} \hat{p} + 2\epsilon \frac{\partial \hat{u}}{\partial \hat{x}} \right), \quad \tau_{xy} = \mu \frac{U}{H} \left(\epsilon \frac{\partial \hat{u}}{\partial \hat{y}} + \epsilon \frac{\partial \hat{v}}{\partial \hat{x}} \right), \quad \tau_{xz} = \mu \frac{U}{H} \left(\frac{\partial \hat{u}}{\partial \hat{z}} + \epsilon \frac{\partial \hat{w}}{\partial \hat{x}} \right).$$

Now, the non-dimensional vector $d\mathbf{S}$ normal to the surface $z = h_L(x, y)$ with length equal to the surface differential area element is given by

$$d\mathbf{S} = \hat{\mathbf{n}} dS = \left(-\epsilon \frac{\partial \hat{h}_L}{\partial \hat{x}} \hat{\mathbf{i}} - \epsilon \frac{\partial \hat{h}_L}{\partial \hat{y}} \hat{\mathbf{j}} + \hat{\mathbf{k}} \right) L^2 d\hat{x} d\hat{y}. \quad (2.23)$$

The non-dimensional element $d\hat{f}$ of the total friction force is given by

$$\begin{aligned} d\hat{f} &= \boldsymbol{\tau} \cdot \hat{\mathbf{i}} \cdot d\mathbf{S} \\ &= \mu \frac{U}{H} \left[\hat{p} \frac{\partial \hat{h}_L}{\partial \hat{x}} - 2\epsilon^2 \frac{\partial \hat{u}}{\partial \hat{x}} \frac{\partial \hat{h}_L}{\partial \hat{x}} - \epsilon^2 \left(\frac{\partial \hat{u}}{\partial \hat{y}} + \frac{\partial \hat{v}}{\partial \hat{x}} \right) \frac{\partial \hat{h}_L}{\partial \hat{y}} + \frac{\partial \hat{u}}{\partial \hat{z}} + \epsilon \frac{\partial \hat{w}}{\partial \hat{x}} \right] L^2 d\hat{x} d\hat{y}, \end{aligned}$$

dropping the terms of order ϵ and ϵ^2 and returning to the original variables we obtain for the dimensional force element

$$df \approx \left(p \frac{\partial h_L}{\partial x} + \mu \frac{\partial u}{\partial z} \right) dx dy. \quad (2.24)$$

Now, using equation (2.10) we calculate

$$\mu \frac{\partial u}{\partial z} \Big|_{z=h_L} = \frac{1}{2} \frac{\partial p}{\partial x} (2z - h_U - h_L) \Big|_{z=h_L} - \mu \frac{(U_L - U_H)}{h} = -\frac{h}{2} \frac{\partial p}{\partial x} - \mu \frac{(U_L - U_H)}{h}. \quad (2.25)$$

Thus, the local friction force on the lower surface by unit area reads

$$df_L = \left(p \frac{\partial h_L}{\partial x} - \frac{h}{2} \frac{\partial p}{\partial x} - \mu \frac{(U_L - U_H)}{h} \right) dx dy. \quad (2.26)$$

where Ω is the domain of interest. Analogously, for the upper surface we obtain

$$df_U = \left(-p \frac{\partial h_U}{\partial x} - \frac{h}{2} \frac{\partial p}{\partial x} + \mu \frac{(U_L - U_H)}{h} \right) dx dy. \quad (2.27)$$

Next, we analyze each term of equation (2.26). For this, please refer to Figure 2.3

where a curved portion of a surface h_L is shown. In the figure, the surface is moving on direction of vector $\hat{\mathbf{e}} = \hat{\mathbf{i}}$ with speed U_L .

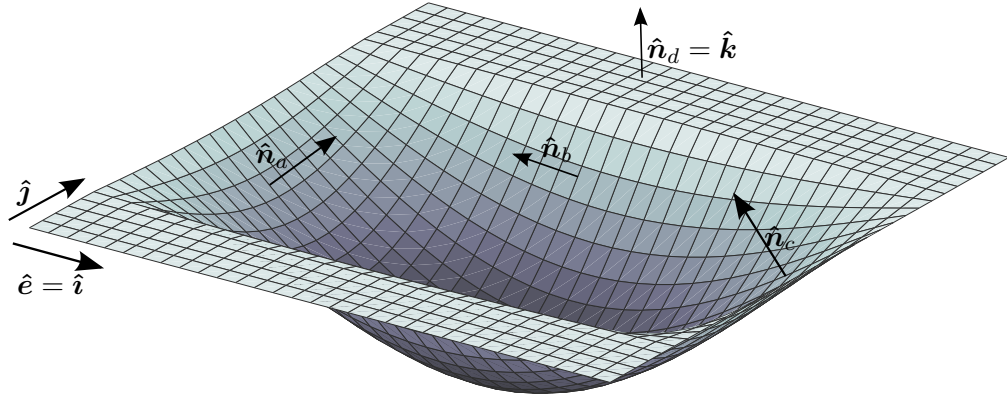


FIGURE 2.3: 2D surface normal orientations scheme.

$p \frac{\partial h_L}{\partial x}$: projection of the force due to the pressure acting on the surface. At point A, the normal vector $\hat{\mathbf{n}}_a$ is oriented positively with respect to $\hat{\mathbf{e}}$ ($\hat{\mathbf{n}} \cdot \hat{\mathbf{e}} > 0$), so pressure must generate a negative force, and this is what happens as $\partial h_L / \partial x$ is negative there. The opposite situation occurs at C, where a positive pressure force is expected and it happens since $\partial h_L / \partial x > 0$. On the other hand, at points B and D the movement direction is perpendicular to the surface orientation, $\hat{\mathbf{e}} \cdot \hat{\mathbf{n}}_b = \hat{\mathbf{e}} \cdot \hat{\mathbf{n}}_d = 0$, so a projection of any normal force is null. This is reflected by $\partial h_L / \partial x = 0$.

$-\frac{h}{2} \frac{\partial p}{\partial x}$: viscous shear due to a Poiseuille flow. A positive pressure gradient on the x -axis generates a parabolic profile negatively oriented which reduces $\partial u / \partial z$.

$-\mu \frac{(U_L - U_H)}{h}$: viscous shear due to a Couette flow. Notice the direction of the relative motion between the surfaces being reflected on the sign of this term.

It can be noticed from equations (2.26) and (2.27) that the local friction force might not be the same on both surfaces. On the other hand, take for simplicity $\Omega = [0, 1] \times [0, 1] \subset \mathbb{R}^2$ and write the periodic conditions $p(0, y) = p(1, y)$, $p(x, 0) = p(0, 1)$ for $x, y \in [0, 1]$, and $h(0, y) = h(1, y)$, $h(x, 0) = h(0, 1)$ for $x, y \in [0, 1]$. Now, let us integrate both friction formula in Ω so we obtain

$$f_L + f_U = - \int_{\Omega} p \frac{\partial h}{\partial x} dx dy - \int_{\Omega} h \frac{\partial p}{\partial x} dx dy.$$

Integrating by parts the first term (see equation (B.12)), and using the periodicity conditions we get

$$\int_{\Omega} p \frac{\partial h}{\partial x} dx dy = - \int_{\Omega} h \frac{\partial p}{\partial x} dx dy,$$

this way we obtain

$$f_L = -f_U,$$

which means that the total friction force on h_L is equal in magnitude to the total friction force on h_U but in the opposite direction.

2.4 Comparison with Navier-Stokes equations

2.4.1 Reynolds and Stokes roughness

Bayada and Chambat [9], Elrod [36] and Phan-Tien [70] found that the validity of Reynolds equation can be claimed when the wavelength of the roughness (λ in Figure 2.4) is large, and the roughness height is small (d in Figure 2.4) when compared to the mean film thickness ($h_m + d/2$ in Figure 2.4). In general, when the roughness of some surface is such that Reynolds equation is a good approximation to the Stokes system, the name *Reynolds roughness* is used; on the other hand, when the roughness is such that Reynolds equation is not a good approximation, and thus the Stokes system must be used, the name *Stokes roughness* is used [9]. A deep discussion of this topic is beyond the scope of this work. Thus, here we only compare the Navier Stokes and Reynolds equations varying the depth d of the roughness. A more complete study also would vary the wavelength λ .

2.4.2 Numerical comparison addressing a sinusoidal texture case

At 100°C, the dynamic viscosity and density of a lubricant oil SAE40 are around $\mu = 1.3 \times 10^{-2} [\text{Pa}\cdot\text{s}]$ and $\rho = 850 [\text{Kg}/\text{m}^3]$ resp. The space between the piston ring and the liner of a combustion engine, for the hydrodynamic regime, is around $H = 10 [\mu\text{m}]$, and the speed of the piston is of order $U = 10 [\text{m}/\text{s}]$. These data give a Reynolds number $\text{Re} = \rho U H / \mu = 6.54$. Thus, in the next set of tests the Reynolds number is around 10. A similar study can be found in [84].

The simulation scheme is showed in Figure 2.4, which consists of two infinite parallel surfaces. The conditions imposed are as follows:

- The lower surface has a sinusoidal shape of period λ and wave amplitude $d/2$, while the upper one is flat. The minimal space between them is h_m .

- A Newtonian incompressible lubricant is placed between the surfaces, its density is ρ and its dynamic viscosity is μ .
- The lower surface is not moving ($U_L = 0$), while the upper one is moving with speed $U_H > 0$.
- No pressure gradient is imposed, instead we set $p(x_0) = p_0$ at some point x_0 of the domain Ω (to be determined).
- Setting $H = h_m + \frac{d}{2}$ (the mean surface height), the Reynolds number $\text{Re} = \rho U_H H / \mu$ is supposed to be low enough for assuring (along with other conditions) the system reaching a steady state.

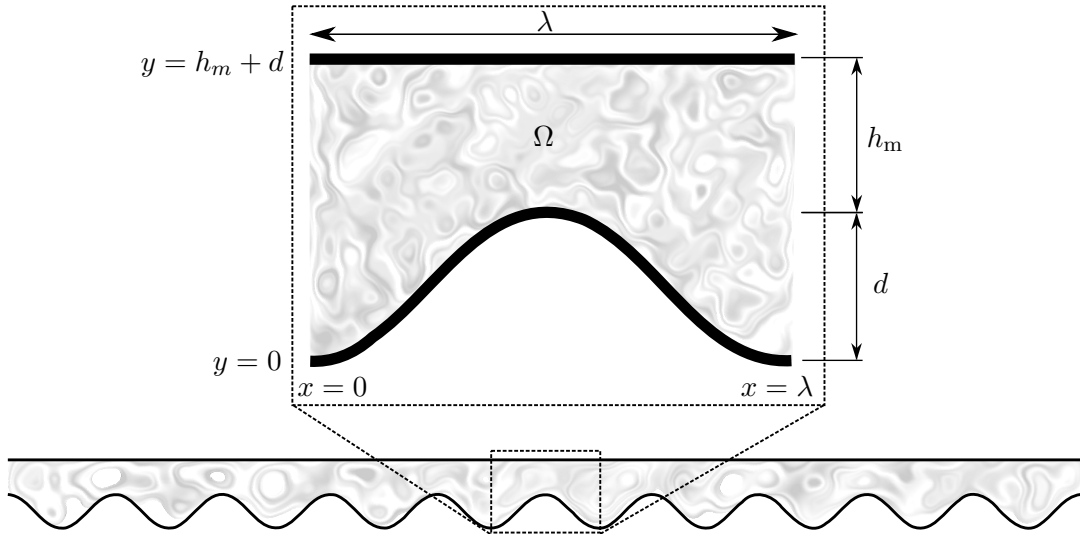


FIGURE 2.4: An infinite 1D bearing with a sinusoidal texture.

With all these assumptions, both Navier-Stokes and Reynolds equations can be solved for this infinite system on just a representative *block*, as Figure 2.4 shown. Now, defining the domain $\Omega = \Omega_d$ as

$$\Omega_d = \{(x, y) \in \mathbb{R}^2 \mid 0 < x < \lambda, h_L(x) < y < h_m + d\},$$

with $h_L(x) = \frac{d}{2}(1 - \cos(2\pi x/\lambda))$, the first mathematical problem reads:

Find the velocity field $\vec{u} = (u(x, z), w(x, z)) : \Omega_d \rightarrow \mathbb{R}^2$ and the pressure field $p : \Omega_d \rightarrow \mathbb{R}$, both periodic in x , satisfying Navier-Stokes equations in Ω_d :

$$\rho \left(\frac{\partial u}{\partial t} + u \frac{\partial u}{\partial x} + w \frac{\partial u}{\partial z} \right) = - \frac{\partial p}{\partial x} + \mu \left(\frac{\partial^2 u}{\partial x^2} + \frac{\partial^2 u}{\partial z^2} \right) \quad (2.28)$$

$$\rho \left(\frac{\partial w}{\partial t} + u \frac{\partial w}{\partial x} + w \frac{\partial w}{\partial z} \right) = - \frac{\partial p}{\partial z} + \mu \left(\frac{\partial^2 w}{\partial x^2} + \frac{\partial^2 w}{\partial z^2} \right), \quad (2.29)$$

along with the continuity equation for incompressible fluids

$$\nabla \cdot \vec{u} = \frac{\partial u}{\partial x} + \frac{\partial w}{\partial z} = 0, \quad \text{in } \Omega_d. \quad (2.30)$$

And the conditions

$$\begin{cases} p(x_0) = p_0, \\ u(x, y = h_m + d) = U_H, \quad u(x, y = h_L(x)) = 0. \\ w(x, y = h_m + d) = 0, \quad w(x, y = h_L(x)) = 0. \end{cases} \quad (2.31)$$

for some $x_0 \in \Omega_d$.

The numerical method used for this problem is described in Appendix A.

Quantity	Scale	Description
x, λ	H	Horizontal coordinate
S	U_H	Sliding velocity
h, h_m, d	H	Fluid thickness
p	$\frac{6\mu U_H}{H^2}$	Hydrodynamic pressure
f	μU_H	Friction force

TABLE 2.1: Non-dimensional variables for the stationary Reynolds equation (2.32).

For the second mathematical problem, we used the non-dimensional variables showed in Table 2.1. Upon these non-dimensionalization, omitting all carets for simplicity, the mathematical problem for the stationary non-dimensional Reynolds equation is written:

Find the pressure field $p : (0, \lambda) \rightarrow \mathbb{R}$ satisfying the stationary Reynolds equation in $(0, \lambda)$:

$$\frac{\partial}{\partial x} \left(h^3 \frac{\partial p}{\partial x} - S h \right) = 0, \quad (2.32)$$

with $h(x) = h_m + d/2 (1 + \cos(2\pi x/\lambda))$ and the conditions

$$p(0) = p(\lambda) = 0. \quad (2.33)$$

Since the problem is one-dimensional there is no need to impose conditions on the pressure gradient. Please notice the great contrast in complexity between both problems. The second one can be solved by a simple integration, yielding

$$p(x) = \int_0^x \frac{\zeta + S h}{h^3} dx, \quad \text{for } x \in [0, \lambda] \text{ with} \quad \zeta = \frac{-S \int_0^\lambda \frac{1}{h^2} dx}{\int_0^\lambda \frac{1}{h^3} dx}.$$

Simulation parameters

We set $U_H = 10[\text{m/s}]$, $H = 10[\mu\text{m}]$, $\lambda = 10$ and $h_m = 1 - d/2$. This setup, along with the non-dimensionalizations, makes the problem dependent only on d and Re . The sets of values chosen for these quantities are

$$d \in \{0, 0.2, 0.4, 0.6, 0.8, 1.0, 1.2, 1.4, 1.6, 1.8\}$$

$$\text{Re} \in \{0.1, 1.0, 5.0, 10.0, 20.0, 50.0, 100.0\}.$$

In both problems (for Reynolds and Navier-Stokes equations) 600 uniform cells were used in the x -axis which correspond to $dx = 0.01667$. For the 2D problem, $dy = dx$ and $dt = 0.45 \min \left\{ \frac{1}{4} dx^2 \text{Re}, \frac{2}{10 \cdot \text{Re}} \right\}$ were set (see [73] Chapter 2 for the stability policy on dt). These numerical parameters were chosen to assure both time and space convergence along with numerical stability.

Results and discussion

As we are interested in the load that a certain system can support and the friction losses involved in the process, the next two basic quantities are compared: 1) the hydrodynamic pressure generated between the surfaces; 2) the friction force opposing the relative motion of the surfaces (see Section §2.3).

For the comparison, we denote as p_r the pressure found by solving (Reynolds equation) equations (2.32) and (2.33) and as p_n the averaged (in y) pressure obtained from equations (2.28), (2.29) and (2.30) along the conditions (2.31).

Figure 2.5 shows the resulting non-dimensional pressure for both sets of equations for the case $\text{Re}=1$, $d = 0.4$. The Reynolds solution is symmetric while the Navier-Stokes solution develops a slightly asymmetrical shape. In fact, for this case

$$|\max p_r(x)| = |\min p_r(x)| = 0.327, \text{ but } |\max p_n(x)| = 0.332 \neq |\min p_n(x)| = 0.344.$$

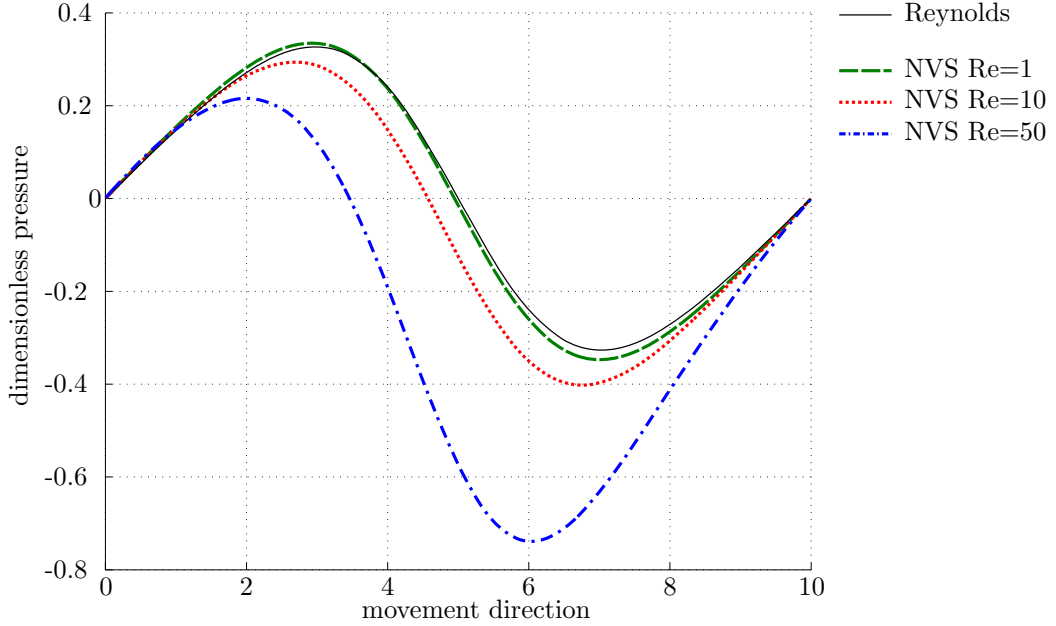


FIGURE 2.5: Dimensionless pressure for Reynolds equation and for Navier-Stokes with $\text{Re}=1, 10, 50$, $d = 0.4$.

This asymmetry can only appear due to the inertial terms of the Navier-Stokes equations which are neglected in the Reynolds approximation. The relative difference of these solutions is 6% (in $\|\cdot\|_\infty$).

Figure 2.6 shows the pressure resulting from Reynolds equation and Navier-Stokes equations for $\text{Re} = 5$ and $d = 0.4, 0.8, 1.2, 1.6$. The bigger the depth d is the smaller the minimal distance between the surfaces h_m is. Because of this, the peak pressure rises when d is augmented. We observe a good agreement for all the depths chosen, in fact, from Figure 2.7 we obtain that the relative differences are around 15 to 20% (in $\|\cdot\|_\infty$).

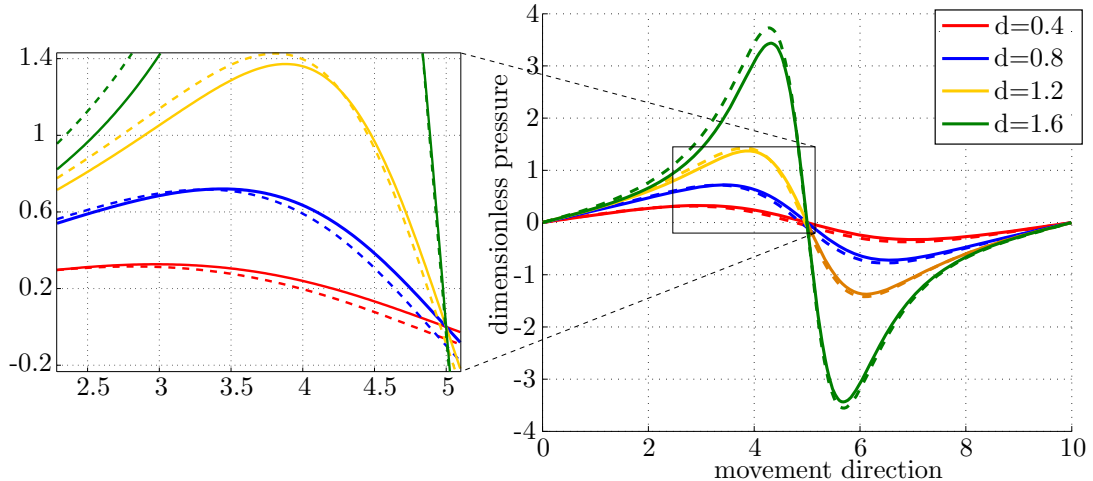


FIGURE 2.6: Dimensionless pressure from Navier-Stokes equations and Reynolds equation for different depth d and $\text{Re} = 5$. The continuous lines show the results from Reynolds equation, while the dashed lines show the results for Navier-Stokes equations.

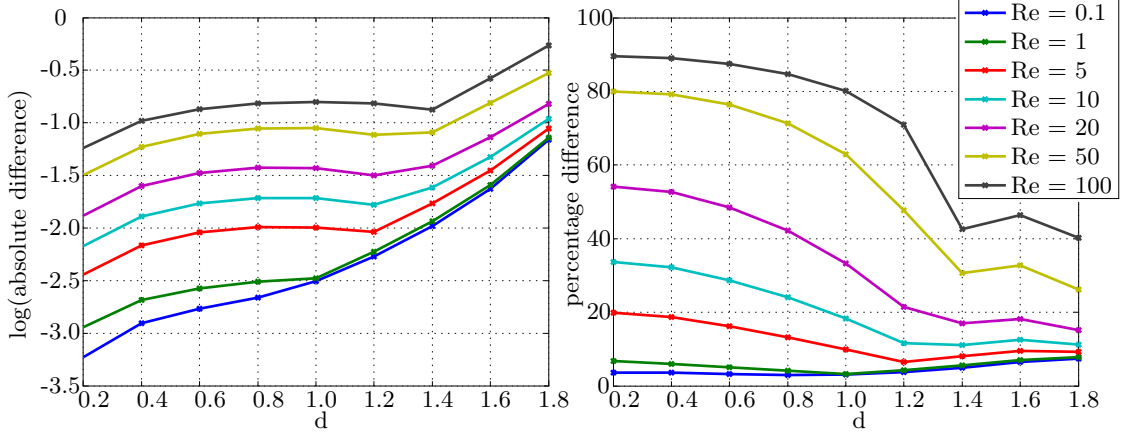


FIGURE 2.7: Dimensionless pressure difference (left) and relative difference (right) for different Reynolds number.

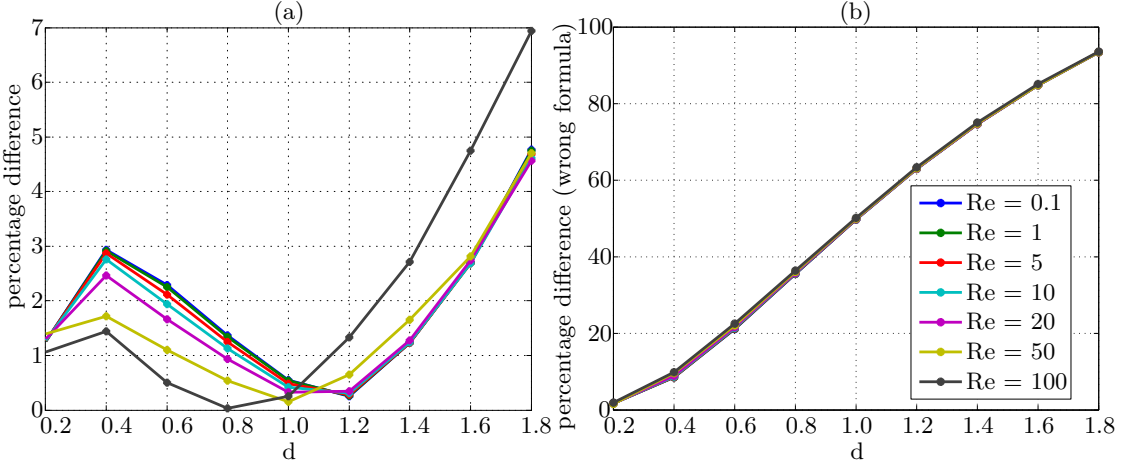


FIGURE 2.8: Left: relative difference in friction difference for Navier Stokes Reynolds equation (using formula (2.26)) and for several Reynolds number. Right: analogous calculation without the projection term $\frac{h_L}{2} \frac{\partial p}{\partial x}$.

As the Reynolds number grows, we expect the difference between the solutions (for pressure and friction) of the Navier Stokes and Reynolds equations to grow. On the other hand, for the validity of Reynolds the value $\lambda/d = 10$ is a well known lower bound for the aspect ratio λ/d [34]. Therefore, as we fix $\lambda = 10$, we also expect the difference between the solutions of the Navier Stokes and Reynolds equations to grow for $d > 1$.

In Figure 2.7 we show the differences for pressure for both sets of equations; at the left side the absolute difference ($\log(\|p_n - p_r\|_\infty)$) is showed; at the right side the relative difference ($100 \times \|p_n - p_r\|_\infty / \|p_n\|_\infty$) is showed.

Since the friction force is derived from the pressure and the velocity of the fluid, we expect a similar behavior between the differences in pressure and the differences in friction. Figure 2.8(a) shows the relative difference in friction ($|f_n - f_r| / |f_n|$), for $d < 1$ friction results are very similar; for $d > 1$ the difference remains low (less than 7%

of difference) but it begins to grow. Figure 2.8(b) shows the relative difference when calculated without including the projection term $p \partial h_L / \partial x$ in formula (2.26). It can be observed that for the cases considered the projection term cannot be neglected as done in some published works [65, 86, 68].

The above results give us some insight about the accuracy of the calculations made in this work. Clearly we are simplifying the problem, as we do not consider cavitation or squeezing effects (temporal terms).

Remark 2.1. A better comparison has been done with a more sophisticated in-house code developed by this research group, already tested in [14, 6]. This has been done since the computation of the friction formula (2.26) requires a better treatment of the derivatives at the boundaries. Therefore, the rectangular mesh used in this section is not suitable. The results indicate clearly the validity of the formula (2.26).

2.5 Some representative analytic solutions

Two types of finite wedges are going to be analyzed in this section, more details of these computations can be found in [18]. Optimal geometric parameters for these wedges will be computed analytically. The selection of these optimal parameters depends on what are we interested in maximize/minimize. In particular, the geometric configuration that minimizes friction is not the configuration that maximizes the load-carrying capacity (defined as the integral of the hydrodynamic pressure).

2.5.1 Step wedge and Rayleigh step

Quantity	Scale	Description
x, l	L	Horizontal coordinate
S	U	Fluid velocity
h, h_0	H	Fluid thickness
p	$6\mu UL/H^2$	Hydrodynamic pressure
f	$\mu UL/H$	Friction forces
W	$6\mu UL^2/H^2$	Load-carrying capacity

TABLE 2.2: Non-dimensional variables for the step wedge problem.

Figure 2.9 shows the scheme of the step wedge problem. In this case, the pad of finite length L is still while a flat surface is moving to the right with constant speed U . To find the hydrodynamic behavior of the lubricant oil between the surfaces, taking the non-dimensionalizations written in Table 2.2, the mathematical problem reads

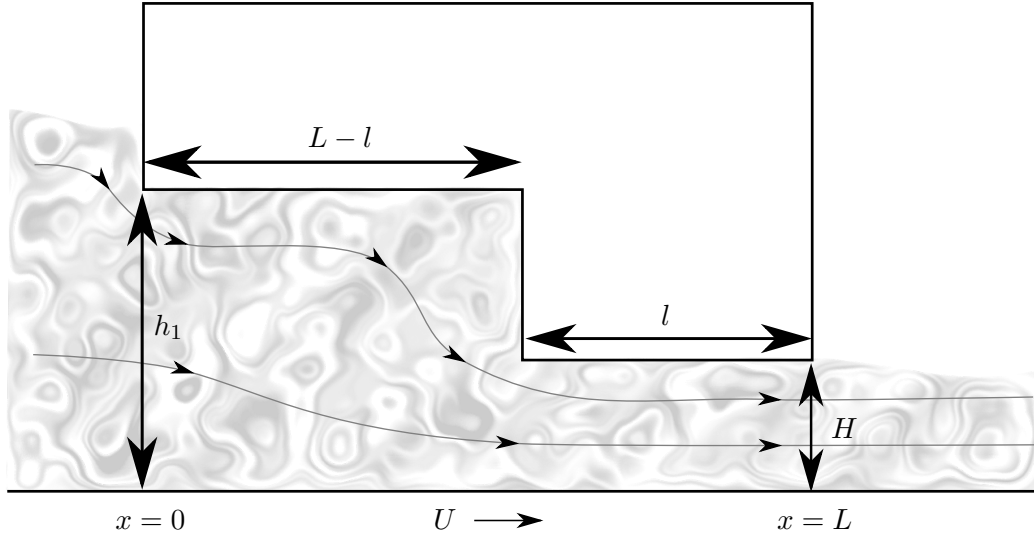


FIGURE 2.9: Step wedge pad scheme.

Find the pressure scalar field $p : [0, 1] \rightarrow \mathbb{R}$, satisfying the stationary Reynolds equation in $[0, 1]$:

$$\frac{\partial}{\partial x} \left(h^3 \frac{\partial p}{\partial x} - S h \right) = 0 \quad (2.34)$$

with $h(x) = h_1$ for $0 \leq x < 1 - l$, and $h(x) = 1$ for $1 - l \leq x \leq 1$. Along with the boundary condition

$$p(0) = p(1) = 0. \quad (2.35)$$

From equation (2.34) we see that the flux function

$$J(x) = -\frac{h^3}{2} \frac{\partial p}{\partial x} + \frac{S}{2} h \quad (2.36)$$

is constant along the domain $]0, 1[$.

From equation (2.34) and the definition of h we see that

$$\frac{\partial^2 p}{\partial x^2} = 0 \text{ in }]0, 1 - l[\cup]1 - l, 1[,$$

and so, using the boundary conditions given by (2.35), and assuming the continuity of p , the pressure can be written as

$$p(x) = \begin{cases} x \left(\frac{\partial p}{\partial x} \right)_{\text{left}} & , 0 \leq x < 1 - l \\ p_{\max} + (x - 1 + l) \left(\frac{\partial p}{\partial x} \right)_{\text{right}} & , 1 - l \leq x \leq 1 \end{cases} \quad (2.37)$$

where $\left(\frac{\partial p}{\partial x}\right)_{\text{left}} = \frac{p_{\max}}{1-l}$ is the left pressure gradient, $\left(\frac{\partial p}{\partial x}\right)_{\text{right}} = -\frac{p_{\max}}{l}$ is the right pressure gradient, and p_{\max} is the peak pressure. To determine the peak pressure p_{\max} we impose mass-conservation on the flux function at $x = 1 - l$:

$$\lim_{x \rightarrow (1-l)^-} J(x) = \lim_{x \rightarrow (1-l)^+} J(x),$$

so

$$-\frac{h_1^3}{2} \left(\frac{\partial p}{\partial x}\right)_{\text{left}} + \frac{S}{2} h_1 = -\frac{1}{2} \left(\frac{\partial p}{\partial x}\right)_{\text{right}} + \frac{S}{2}.$$

Replacing the expressions of the gradients for both left and right sides we obtain

$$p_{\max} = S \frac{l(h_1 - 1)(1 - l)}{1 + l(h_1^3 - 1)}. \quad (2.38)$$

We have solved the problem of looking for the pressure of the step wedge. Now, we can ask for some tribological characteristics of the system. First, we look for the load-carrying capacity and its optimal configuration. Next, we look for the friction force and its optimal configuration too.

Load-carrying capacity of the step wedge

The load-carrying capacity W is just the integral of the pressure distribution. Thus, using (2.37) and (2.38) we have

$$W = \int_0^1 p(x) dx = \frac{1}{2} p_{\max}. \quad (2.39)$$

Now, for finding the optimal configuration, i.e., the 2-tuple (h_1, l) for which the maximum W is reached, we seek for the configurations that nullifies the gradient of W and, between those configurations, the ones having a negative definite Hessian matrix. Doing so, we obtain the optimal configuration:

$$h_1 = \frac{\sqrt{3} + 2}{2} \approx 1.866, \quad l = \frac{4}{\sqrt{27} + 9} \approx 0.282, \quad \frac{1 - l}{l} = \frac{\sqrt{27} + 5}{4} \approx 2.549,$$

which corresponds to a load-carrying capacity

$$W = S \frac{2}{9} \left(\frac{4\sqrt{3} + 7}{26\sqrt{3} + 45} \right) \approx 0.034 S.$$

This configuration is known in the literature as the *Rayleigh Step*. Lord Rayleigh, in 1918 [76], found it by using calculus of variations to find the shape of the step wedge that maximizes the load-carrying capacity.

Friction force of the step wedge

Friction force F can be calculated for the step wedge from equation (2.26) and the pressure profiles found above. The computation reads

$$\begin{aligned} F &= \int_0^1 \left(3h \frac{\partial p}{\partial x} + \frac{S}{h} \right) dx \\ &= \int_0^{1-l} \left(3h \frac{\partial p}{\partial x} + \frac{S}{h} \right) dx + \int_{1-l}^1 \left(3h \frac{\partial p}{\partial x} + \frac{S}{h} \right) dx \\ &= \left[3h_1 \left(\frac{p_{\max}}{1-l} \right) + \frac{S}{h_1} \right] (1-l) + \left[3 \left(\frac{-p_{\max}}{l} \right) + S \right] l \\ &= S \left(3 \frac{l(1-l)(h_1 - 1)^2}{1 + l(h_1^3 - 1)} + \frac{1-l}{h_1} + l \right), \end{aligned} \quad (2.40)$$

taking derivatives it is found that

$$\frac{\partial F}{\partial l} = S \left(\frac{3h_1^3(h_1 - 1)}{(h_1^2 + h_1 + 1)[(h_1^3 - 1)l + 1]^2} + \frac{(h_1 - 1)^3}{h_1^3 + h_1^2 + h_1} \right)$$

and

$$\frac{\partial F}{\partial h_1} = -S \frac{(1-l) [(2h_1^3 - 3h_1 + 1)l - 1]}{h_1^2 [(h_1^3 - 1)l + 1]^2}.$$

So we have

$$\frac{\partial F}{\partial l} > 0 \text{ and } \frac{\partial F}{\partial h_1} < 0, \text{ whenever } h_1 > 1 \text{ and } l \in (0, 1) \text{ resp.}$$

Therefore, the configuration that minimizes friction depends on the design restrictions under the policy: “take l as small as possible, and h_1 as large as possible”. However, from equations (2.38) and (2.39) it can be observed that using this policy the load-carrying capacity W goes to zero. In consequence, another quantity is needed to characterize the friction relatively to the load-carrying capacity. In the literature, the *friction coefficient* is defined as the quotient between the total friction force and the applied load. Thus, considering the non-dimensionalizations presented before (see Table 2.2), the friction coefficient reads

$$C_f = \frac{H}{6L} \frac{F}{W}. \quad (2.41)$$

This quantity was also studied by Lord Rayleigh in its classic work [76]. Making similar calculations we made before for the maximum load-carrying capacity, the configuration that minimizes C_f is found to be

$$h_1 = 2, \quad l = \frac{1}{5}, \quad \frac{1-l}{l} = 4,$$

for which

$$C_f = 4 \frac{H}{L},$$

while for the Rayleigh Step we have $C_f = 4.098 \frac{H}{L}$.

This results can be found also in a recent work by Rahmani et al. [75], where they made an analysis of the Rayleigh Step analytically. They based their work on the Reynolds equation considering non-homogeneous boundary conditions for pressure. Analytic relations for parameters as load capacity and friction force were also developed and studied seeking for optimal configurations.

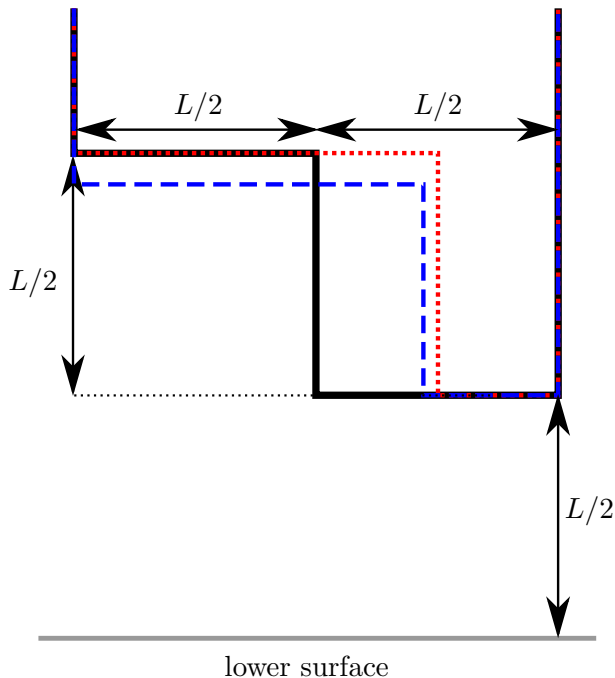


FIGURE 2.10: Scheme of the “naive step wedge” (solid black line) versus the Rayleigh Step wedge (dashed blue line), and the wedged that minimizes C_f (dotted red line).

Comparison of Rayleigh Step with a naive step wedge

By *naive step wedge* we meant a 2-tuple (h_1, l) chosen, arguably, as simple as possible. The idea is to have a non trivial reference design to compare with the optimal designs found above.

The design we choose for this comparison is shown in Figure 2.10. In that figure, the blue dashed lines represent the real proportions of the Rayleigh Step wedge, while the black line represents our simple step of length L with proportions $(L - 1)/l = 1$ and $h_1/H = 2$ (see Figure 2.9).

We use equations (2.39) and (2.40) to calculate the load carrying-capacity of both the Rayleigh Step wedge and our naive step wedge, denoted by W_R and W_0 resp.. We also calculate the friction force for both the Rayleigh Step and the naive step wedge, denoted as F_R and F_0 , respectively. Doing the computations, we found

$$\frac{W_0}{W_R} = 0.81 \quad \text{and} \quad \frac{F_0}{F_R} = 1.08.$$

We observe that the Rayleigh Step augments 19% the load-carrying capacity and diminishes 8% the friction force when compared to the naive step wedge.

2.5.2 Disc wedge

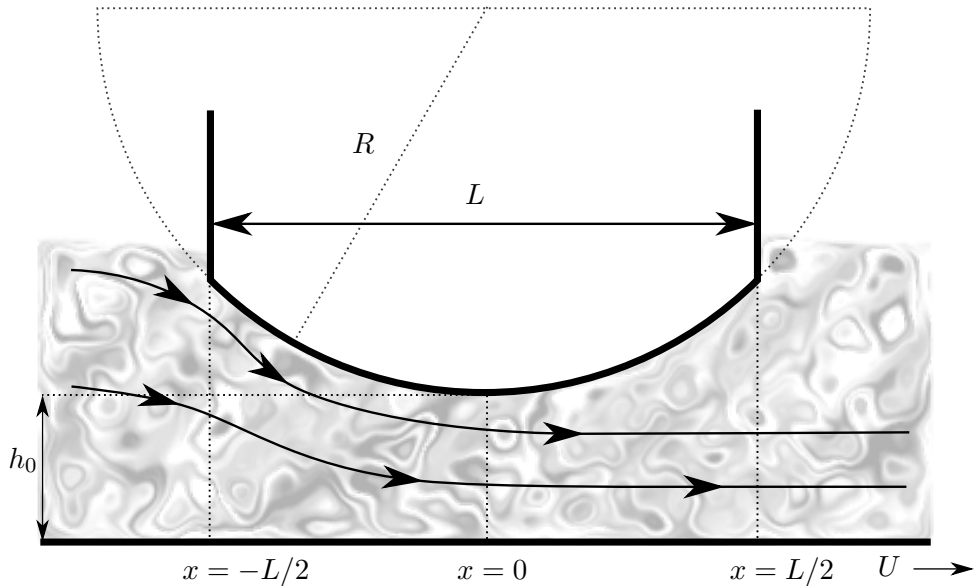


FIGURE 2.11: Disc pad scheme.

In this case, the pad has a circular shape, symmetric along x -axis, centered at $x = 0$ (see Figure 2.11) with radius of curvature R . Non-dimensionalizations are the same as in previous section, including this time the variable R with scale L (see Table 2.3).

Quantity	Scale	Description
x, R	L	Horizontal coordinate
S	U	Fluid velocity
h, h_0	H	Fluid thickness
p	$\frac{6\mu UL}{H^2}$	Hydrodynamic pressure

TABLE 2.3: Non-dimensional variables for the disc wedge problem.

This problem has a major difference with the step wedge problem (previous section), as in this geometry a divergent zone is present for $0 < x < L/2$. Thus, negative pressures are expected to appear at that divergent zone. The mathematical problem is written (non-dimensionalization are shown in Table 2.3):

Find the pressure scalar field $p : [-0.5, 0.5] \rightarrow \mathbb{R}$, satisfying the stationary Reynolds equation:

$$\frac{\partial}{\partial x} \left(h^3 \frac{\partial p}{\partial x} - S h \right) = 0, \quad \text{in } (-0.5, 0.5) \quad (2.42)$$

where the film thickness function is given by

$$h(x) = h_0 + \frac{L}{H} \left(R - \sqrt{R^2 - x^2} \right), \quad x \in [-0.5, 0.5],$$

along with the boundary conditions for pressure

$$p(-0.5) = p(0.5) = 0. \quad (2.43)$$

To simplify calculations we approximate the thickness function (up to an error of order $10^{-7} \times L/H$) by

$$h(x) = h_0 + \frac{L}{H} \frac{x^2}{2R}, \quad x \in [-0.5, 0.5].$$

From Reynolds equation (2.42) we have that the flux function

$$J = -\frac{h^3}{2} \frac{\partial p}{\partial x} + S \frac{h}{2}$$

is constant along the domain. This way, Reynolds equation can be rewritten as

$$\frac{\partial p}{\partial x} = S \frac{(h - \bar{h})}{h^3}, \quad (2.44)$$

where \bar{h} is some constant to determine. Now, we make the change of variables

$$\tan \gamma = \frac{x}{\sqrt{2 h_0 R H / L}}.$$

And so, the double integration of equation (2.44) gives ($\bar{h} = h_0 \sec^2(\bar{\gamma})$)

$$p(\gamma) = S \sqrt{2 R L / H} \left(\frac{\gamma}{2} + \frac{\sin 2\gamma}{4} - \frac{1}{\cos^2 \bar{\gamma}} \left[\frac{3}{8} \gamma + \frac{\sin 2\gamma}{4} + \frac{\sin 4\gamma}{32} \right] \right) + C, \quad (2.45)$$

where $\bar{\gamma}$ and C are determined from boundary conditions (2.43).

Figure 2.12 shows the pressure profile for the case $R = 80$, $S = 1$, $h_0 = 1$, $L = 1 \times 10^{-3}$ [m] and $H = 1 \times 10^{-6}$ [m]. The anti-symmetric pressure profile is such that it is positive at the convergent zone (where $\partial_x h < 0$) and negative at the divergent zone (where $\partial_x h > 0$). These negative pressures will be subject of study in Chapter 4.

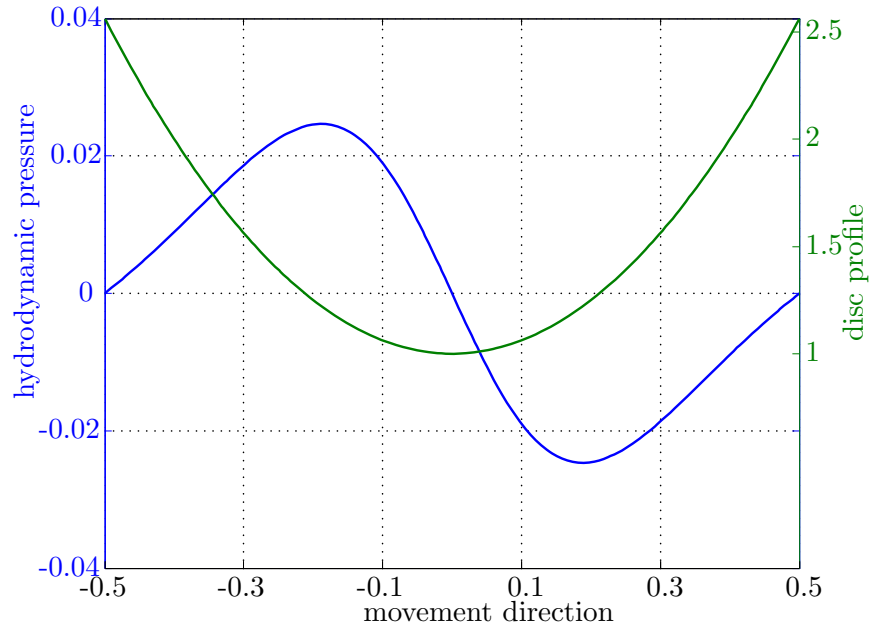


FIGURE 2.12: Disc pad scheme and pressure profile.

Chapter 3

Mathematics of Reynolds equation

We have shown in Chapter 2 that Reynolds equation models the tribological variables of two surfaces being lubricated. In this chapter a mathematical analysis is developed in order to study the *well-posedness* of Reynolds equation. Using powerful tools of Functional Analysis, like the Hilbert Spaces structure, *existence*, *uniqueness* and *stability* of solutions of Reynolds equation will be addressed. Furthermore, we will seek for *regularity* of the solutions, i.e., how much smooth the solutions are. As the reader may guess, the last question will be related to the quality of the input: how *regular* is the gap between the surfaces?; how *regular* is the boundary of the domain?.

For this we will consider a measurable domain $\Omega \subset \mathbb{R}^2$, with Lebesgue measure $\mu(\Omega) < +\infty$, and a measurable subdomain $\omega \subset \Omega$ where Reynolds equation holds. In this chapter, ω is a data of the problem and it is supposed to be locally Lipschitz (see definition B.29). The general problem, where ω is also an unknown, will be studied in Chapter 4 where $\Omega \setminus \omega$ will be determined by the cavitation phenomenon.

3.1 From Stokes equations to Reynolds equation

Along Sections §2.1 and §2.2 we have made asymptotic expansions for obtaining Reynolds equation from Navier-Stokes equations. Bayada and Chambat (1986) [8] proved mathematically that Reynolds equation is an approximation of Stokes equations. In the following, we summarize their results in order to give a mathematical comprehension of the relation between both sets of equations.

Consider two surfaces in proximity and in relative motion (see Figure 3.1). The first surface (lower one), denoted by ω , is a planar bounded domain of \mathbb{R}^2 placed in the plane $z = 0$ and its boundary $\partial\omega$ is locally Lipschitz. The second surface (upper one) is characterized by $z = H(x, y)$, $(x, y) \in \omega$. The thin distance between both surfaces is taken into account by introducing a small parameter ϵ , which will tend to 0, and a fixed function $h : \omega \rightarrow \mathbb{R}^+$ such that

$$H(x, y) = \epsilon h(x, y),$$

with $h \in C^1(\bar{\omega})$ and $h \geq \alpha > 0$.

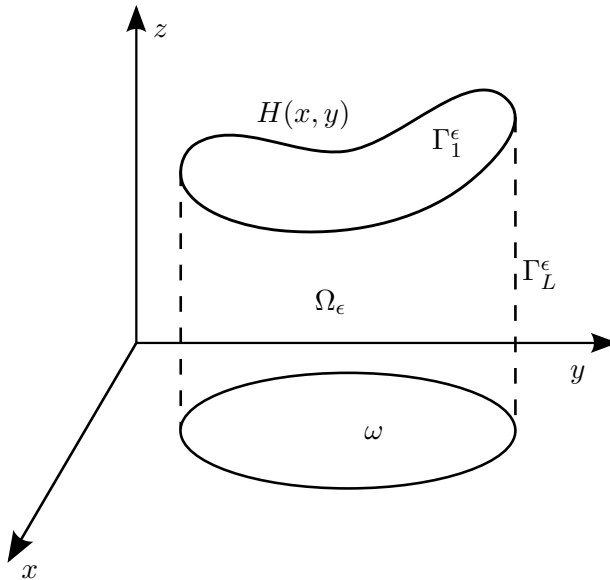


FIGURE 3.1: Ω_ϵ scheme. Based on Fig. 1 in [8].

Let us write the domain

$$\Omega_\epsilon = \{(x, y, z) \in \mathbb{R}^3, (x, y) \in \omega, 0 < z < H(x, y)\},$$

and $\Gamma_\epsilon = \partial\Omega_\epsilon = \bar{\omega} \cup \bar{\Gamma}_1^\epsilon \cup \bar{\Gamma}_L^\epsilon$ its boundary (see Figure 3.1). On Ω_ϵ , the Stokes system¹ and the continuity equation for a Newtonian fluid can be written resp. as

$$-\mu \nabla^2 \mathbf{U}^\epsilon + \nabla p^\epsilon = 0 \quad (3.1)$$

$$\nabla \cdot \mathbf{U}^\epsilon = 0, \quad (3.2)$$

¹ Assuming no source term on the right hand side of Equation (3.1) as generally occurs in Lubrication Theory.

where μ is the dynamic viscosity, \mathbf{U}^ϵ is the velocity field of the fluid and p^ϵ is its hydrodynamic pressure. Dirichlet boundary conditions for the velocities $\mathbf{U}^\epsilon = (g^\epsilon, 0, 0)$ on Γ^ϵ are imposed, where

$$g^\epsilon = 0, \quad \text{on } \Gamma_1^\epsilon \quad (3.3)$$

$$g^\epsilon = S > 0, \quad \text{on } \omega. \quad (3.4)$$

Also, in order to make sure that the Stokes equations have a solution, the authors [8] impose the condition

$$g^\epsilon \in H^{1/2}(\Gamma^\epsilon) \quad \text{and} \quad \int_{\Gamma_L^\epsilon} g^\epsilon \cos(\hat{\mathbf{n}}, \hat{\mathbf{e}}_1) d\sigma = 0, \quad (3.5)$$

where $\hat{\mathbf{n}}$ is the normal unit vector pointing outward Ω_ϵ and $\hat{\mathbf{e}}_1$ is the unit vector pointing positively along the x -axis. The first condition is a regularity requirement and the second condition is for mass-conservation.

Existence and uniqueness for Stokes system

First, let us define the space $L_0^2(\Omega_\epsilon) = \{f \in L^2(\Omega_\epsilon) : \int_{\Omega_\epsilon} f dV = 0\}$, $dV = dx dy dz$, which is the class of functions with zero average. This set is considered since the pressure is uniquely determined up to an additive constant.

The next theorem establishes the existence and uniqueness of the Stokes problem defined by equations (3.1)-(3.4). It is a well known result and it can be found, for instance, in [47]:

Theorem 3.1. *Under assumptions (3.3), (3.4) and (3.5), there exists a unique pair of functions $(\mathbf{U}^\epsilon, p^\epsilon)$ in $(H^1(\Omega_\epsilon))^3 \times L_0^2(\Omega_\epsilon)$ such that*

$$\begin{aligned} -\mu \nabla^2 \mathbf{U}^\epsilon + \nabla p^\epsilon &= 0 \\ \nabla \cdot \mathbf{U}^\epsilon &= 0 \\ \mathbf{U}^\epsilon &= (g^\epsilon, 0, 0), \quad \text{on } \Gamma^\epsilon. \end{aligned}$$

Moreover, let us define the bilinear form a by $a(\mathbf{U}, \mathbf{V}) = \sum_{i=1}^3 \int_{\Omega_\epsilon} \nabla u_i \cdot \nabla v_i dV$. Then, $(\mathbf{U}^\epsilon, p^\epsilon)$ satisfies the weak formulation:

$$\begin{aligned} \mu a(\mathbf{U}^\epsilon, \Phi) &= \int_{\Omega_\epsilon} p^\epsilon \nabla \cdot \Phi dV & \forall \Phi \in (H_0^1(\Omega_\epsilon))^3 \\ 0 &= \int_{\Omega_\epsilon} q \nabla \cdot \mathbf{U}^\epsilon dV, & \forall q \in L_0^2(\Omega_\epsilon), \end{aligned}$$

and there exists a function $\mathbf{G}^\epsilon \in H^1(\Omega_\epsilon)^3$ such that

$$\nabla \cdot \mathbf{G}^\epsilon = 0, \quad \mathbf{G}^\epsilon - \mathbf{U}^\epsilon \in (H_0^1(\Omega_\epsilon))^3. \quad (3.6)$$

Now, set the domain $\Omega = \{(x, y, Z) \in \mathbb{R}^3, (x, y) \in \omega, 0 < Z < h(x, y)\}$, and for any function $v(x, y, z)$ defined on Ω_ϵ associate the function $\hat{v}(x, y, Z) = v(x, y, \epsilon Z)$ defined on Ω .

Along this definitions and using Functional Analysis (e.g.², Chapter “Banach and Hilbert Spaces” in [87], Chapters III and V in [1]) the authors [8] obtained the next results regarding convergence of the functions $\hat{\mathbf{U}}^\epsilon$ and \hat{p}^ϵ .

Convergence of the solutions

Theorem 3.2. *Suppose there exists a constant K , not depending on ϵ , such that G^ϵ in Theorem 3.1 satisfies*

$$\|\nabla \hat{G}_i^\epsilon\|_{(L^2(\Omega))^3} \leq K, \quad i = 1, 2, 3, \quad (3.7)$$

then, there exists \mathbf{U}^ in $(L^2(\Omega))^3$ such that*

$$\hat{\mathbf{U}}^\epsilon \rightarrow \mathbf{U}^*, \quad \frac{\partial \hat{\mathbf{U}}^\epsilon}{\partial Z} \rightarrow \frac{\partial \mathbf{U}^*}{\partial Z}, \quad \epsilon \frac{\partial \hat{\mathbf{U}}^\epsilon}{\partial x} \rightarrow 0, \quad \epsilon \frac{\partial \hat{\mathbf{U}}^\epsilon}{\partial y} \rightarrow 0$$

weakly in $(L^2(\Omega))^3$.

The proof of Theorem 3.2 is based on the following estimates that are proved by the authors [8] (under the hypothesis of Theorem 3.2)

$$\|\hat{\mathbf{U}}^\epsilon\|_{(L^2(\Omega))^3} \leq K, \quad \left\| \frac{\partial \hat{u}_i^\epsilon}{\partial \xi} \right\|_{L^2(\Omega)} \leq \frac{K}{\epsilon}, \quad \left\| \frac{\partial \hat{u}_i^\epsilon}{\partial Z} \right\|_{L^2(\Omega)} \leq K, \quad i = 1, 2, 3, \xi \in \{x, y\}.$$

Also a result on the convergence of p_ϵ is given, which is based on the next estimates

$$\left\| \frac{\partial \hat{p}_\epsilon}{\partial x} \right\|_{H^{-1}(\Omega)} \leq \frac{K}{\epsilon^2}, \quad \left\| \frac{\partial \hat{p}_\epsilon}{\partial y} \right\|_{H^{-1}(\Omega)} \leq \frac{K}{\epsilon^2}, \quad \left\| \frac{\partial \hat{p}_\epsilon}{\partial Z} \right\|_{H^{-1}(\Omega)} \leq \frac{K}{\epsilon}.$$

Theorem 3.3. *There exists p^* in $L_0^2(\Omega)$ such that $\epsilon^2 \hat{p}_\epsilon$ converges weakly to p^* ; moreover $\frac{\partial p^*}{\partial Z} = 0$.*

²The reader can find a summary of the main results in Appendix B.

Functional relations of the limit solutions

Once the existence of limit solutions was established, the authors found that these limits accomplishes analogous equations as those found in Sections §2.1 and §2.2.

Theorem 3.4. *Under the same hypothesis of Theorem 3.2, the components of the limit field \mathbf{U}^* satisfies the equations:*

$$\begin{aligned}\frac{\partial p^*}{\partial x} &= \mu \frac{\partial^2 u_1^*}{\partial Z^2}, && \text{in } H^{-1}(\Omega) \\ \frac{\partial p^*}{\partial y} &= \mu \frac{\partial^2 u_2^*}{\partial Z^2}, && \text{in } H^{-1}(\Omega) \\ u_3^* &= 0, && \text{in } \Omega.\end{aligned}$$

Now, for any function $v(x, y, z)$ in $H^1(\Omega_\epsilon)$, or the corresponding $\hat{v}(x, y, Z)$ in $H^1(\Omega)$, define the average

$$\bar{v}(x, y) = \frac{1}{h} \int_0^h \hat{v}(x, y, Z) dZ = \frac{1}{\epsilon h} \int_0^{\epsilon h} v(x, y, z) dz$$

so \bar{v} lies in $H^1(\omega)$.

Theorem 3.5. *Under the same hypothesis of Theorem 3.2, the average velocity field \bar{u}^* satisfies*

$$\begin{aligned}\bar{u}_1^* &= \frac{S}{2} - \frac{h^2}{12\mu} \frac{\partial p^*}{\partial x}, \quad \bar{u}_2^* = -\frac{h^2}{12\mu} \frac{\partial p^*}{\partial y} && \text{both in } H^{-1}(\omega), \\ \bar{u}_3^* &= 0 && \text{in } \omega.\end{aligned}$$

Moreover, the average velocity field $\bar{\mathbf{U}}^\epsilon$ satisfies the “mass flow conservation” equation:

$$\frac{\partial}{\partial x} (h \bar{u}_1^\epsilon) + \frac{\partial}{\partial y} (h \bar{u}_2^\epsilon) = 0 \quad \text{in } \mathcal{D}'(\omega),$$

and the limit average velocity field satisfies the “mass-conservation” equation

$$\frac{\partial}{\partial x} (h \bar{u}_1^*) + \frac{\partial}{\partial y} (h \bar{u}_2^*) = 0 \quad \text{in } \mathcal{D}'(\omega).$$

Furthermore, regarding strong convergence the authors [8] found the next result:

Theorem 3.6. *Under the hypothesis of Theorem 3.2, suppose there exists a function $\hat{g} \in H^{1/2}(\Gamma)$ that does not depends on ϵ , such that*

$$g^\epsilon(x, y, z) = \hat{g}(x, y, z/\epsilon) \tag{3.8}$$

then, it holds

- $\epsilon^2 p^\epsilon, \epsilon^2 \frac{\partial p^\epsilon}{\partial x}, \epsilon^2 \frac{\partial p^\epsilon}{\partial y}$ and $\epsilon \frac{\partial p^\epsilon}{\partial Z}$ converge strongly in $L^2(\omega)$ to $p^*, \frac{\partial p^*}{\partial x}, \frac{\partial p^*}{\partial y}$ and 0 resp.
- p^* is unique and lies in $H^1(\omega)$, also it satisfies

$$\nabla \cdot \left(\frac{h^3}{12\mu} \nabla p^* \right) = \frac{S}{2} \frac{\partial h}{\partial x},$$

which corresponds to Reynolds equation (2.19) in the steady case with $U_L = S$, $U_H = V_H = V_L = 0$.

Conclusions

- Reynolds Equation is an approximation of the Stokes system when ϵ is small.
- The authors have shown that the solution of Stokes equations converges to the solution of Reynolds equation when ϵ goes to 0.
- $h \in C^1(\bar{\omega})$ is a strong hypothesis. It would be interesting to extend this work under more *realistic* hypothesis like $h \in L^\infty(\omega)$. This kind of functions can be found when considering discontinuous textures [5, 86, 46].

3.2 Weak formulation for Reynolds equation

Here we consider the non-dimensional velocity S as $S = 1$. From a classical point of view, solving Reynolds equation consists in seek for a pressure field $p \in C^2(\bar{\omega})$ satisfying the non-dimensional Reynolds equation

$$\frac{\partial}{\partial x} \left(h^3 \frac{\partial p}{\partial x} \right) + \frac{\partial}{\partial y} \left(h^3 \frac{\partial p}{\partial y} \right) = \frac{\partial h}{\partial x} + 2 \frac{\partial h}{\partial t} \quad \text{in } \omega \quad (3.9)$$

$$p = 0 \quad \text{in } \partial\omega, \quad (3.10)$$

where ω is a domain in \mathbb{R}^2 of class C^1 and h is continuously differentiable both in space and time.

Please notice that in equation (3.9) time is only a parameter. In the analysis we will show it will remain being a parameter.

Frequently, these hypotheses about the smoothness of p , h and $\partial\omega$ are too strong. For instance, there are several works (both numerical and experimental) where textured surfaces are described by h being discontinuous [91, 90, 82, 21]. For handling this,

we need to look beyond the classical definition of derivative: here is where the tools of Functional Analysis appear. First, we rewrite the problem below for accomplishing weaker hypothesis. For this, first we multiply Reynolds equation (3.9) by some *test function* $\phi \in H_0^1(\omega)$ and make use of Green's formula (see equation (B.12)) to obtain

$$\begin{aligned} \int_{\omega} h^3 \nabla p \nabla \phi \, dA &= - \int_{\omega} \phi \frac{\partial h}{\partial x} - 2 \int_{\omega} \phi \frac{\partial h}{\partial t} \, dA \\ &= \int_{\omega} h \frac{\partial \phi}{\partial x} \, dA - 2 \int_{\omega} \phi \frac{\partial h}{\partial t} \, dA \quad \forall \phi \in H_0^1(\omega), \end{aligned} \quad (3.11)$$

with $dA = dx \, dy$. Observe the boundary term is null since $\phi = 0$ a.e. in $\partial\omega$.

Now, take a gap function $h : \omega \times [0, +\infty) \rightarrow \mathbb{R}^+$ such that

$$h(\cdot, t) \in L^\infty(\omega) \quad \forall t \in [0, +\infty) \text{ and } \frac{\partial h(\cdot, t)}{\partial t} \in H^{-1}(\omega) \quad \forall t \in [0, +\infty), \quad (3.12)$$

so, as ω has finite measure, we have $h(\cdot, t) \in L^p(\omega)$ for any $p \in [1, \infty]$ (see Lemma B.14).

With this, given ω locally Lipschitz with measure $\mu(\omega) < \infty$ and h accomplishing (3.12), we can rewrite our original problem as: find a function $p(\cdot, t) \in H_0^1(\omega)$ such that

$$\int_{\omega} h^3 \nabla p \nabla \phi \, dA = \int_{\omega} h \frac{\partial \phi}{\partial x} \, dA - 2 \int_{\omega} \phi \frac{\partial h}{\partial t} \, dA \quad \forall t \in [0, \infty) \quad \forall \phi \in H_0^1(\omega). \quad (3.13)$$

Now on, we use the norm on $H_0^1(\omega)$ given by

$$\|\phi\|_{H_0^1(\omega)} = \|\nabla \phi\|_{L^2(\omega)},$$

and let us assume h is such that:

$$\text{there exist } a, b \in \mathbb{R}^+ \text{ such that } 0 < a \leq h(x, y, t) \leq b \text{ a.e. on } \omega \quad \forall t \in [0, +\infty). \quad (3.14)$$

Also, define the bilinear form $B(h) : H_0^1(\omega) \times H_0^1(\omega) \rightarrow \mathbb{R}$ as

$$B(h; u, v) = \int_{\omega} h^3 \nabla u \nabla v \, dA. \quad (3.15)$$

Since $h(\cdot, t) \in L^2(\omega)$ and $\frac{\partial h(\cdot, t)}{\partial t} \in H^{-1}(\omega)$, the functional $\ell(h) : H_0^1(\omega) \rightarrow \mathbb{R}$ defined by

$$\ell(h; \phi) = \int_{\omega} h \frac{\partial \phi}{\partial x} \, dA - 2 \int_{\omega} \frac{\partial h}{\partial t} \phi \, dA \quad (3.16)$$

is a linear functional on $H_0^1(\omega)$.

Proposition 3.7. *Suppose h satisfying (3.12) and (3.14), then B , defined in (3.15), is a continuous coercive bilinear form on $H_0^1(\omega)$ and ℓ , defined in (3.16), is a continuous*

linear functional on $H_0^1(\omega)$.

Proof. Bilinearity of B and linearity of ℓ are trivial from the linearity of the operators involved. To prove continuity of $B(h)$, using Cauchy-Schwarz inequality we have

$$B(h; u, v) = \int_{\omega} h^3 \nabla u \nabla v \, dx \leq b^3 \|\nabla u\|_{L^2(\omega)} \|\nabla v\|_{L^2(\omega)} = b^3 \|u\|_{H_0^1(\omega)} \|v\|_{H_0^1(\omega)}.$$

For proving coercivity, we write

$$B(h; v, v) = \int_{\omega} h^3 |\nabla v|^2 \, dx \geq a^3 \|\nabla v\|_{L^2(\omega)}^2 = a^3 \|v\|_{H_0^1(\omega)}^2. \quad (3.17)$$

Now, for ℓ , from Cauchy-Schwarz inequality we have

$$|\ell(h; \phi)| = \left| \int_{\omega} h \partial_x \phi \, dA - 2 \int_{\omega} \partial_t h \phi \, dA \right| \quad (3.18)$$

$$\leq \|h(\cdot, t)\|_{L^2(\omega)} \|\partial_x \phi\|_{L^2(\omega)} + 2 \|\partial_t h(\cdot, t)\|_{H^{-1}(\omega)} \|\phi\|_{H^1(\omega)} \quad (3.19)$$

$$\leq C(h(\cdot, t), \omega) \|\phi\|_{H_0^1(\omega)}, \quad (3.20)$$

being $C(h(\cdot, t), \omega) = \|h(\cdot, t)\|_{L^2(\omega)} + C_1(\omega) \|\partial_t h(\cdot, t)\|_{H^{-1}(\omega)}$, and C_1 is a Poincaré constant. Therefore, $\ell(h; \cdot)$ is continuous on $H_0^1(\omega)$. \square

With all this, equation (3.13) can be written as, for each time t

$$B(h; p, \phi) = \ell(h; \phi), \quad \forall \phi \in H_0^1(\omega), \quad (3.21)$$

and by definition, we say a function $p \in C^1(0, +\infty, C^2(\overline{\omega}))$ accomplishing equations (3.9) and (3.10) is a *classical solution* of (3.9)-(3.10). While a function $p(\cdot, t) \in H_0^1(\omega)$ is a *weak solution* of (3.9)-(3.10) if it satisfies equation (3.21).

Thus, as both $B(h)$ and $\ell(h)$ satisfy the hypothesis of Lax-Milgram Theorem (see Appendix B) we have the next result:

Theorem 3.8. *The problem “to find $p(\cdot, t) \in H_0^1(\omega)$ accomplishing equation (3.21) for an arbitrary time $t \in [0, +\infty)$ ” has a unique solution.*

3.2.1 Stability Analysis

Does the unique solution of equation (3.21) depends continuously on h ? A first idea is to take $\phi = p(\cdot, t)$ in equation (3.21) and so, using equations (3.20) and (3.17), we have

$$\|p(\cdot, t)\|_{H_0^1(\omega)} \leq \frac{1}{a^3} \{ \|h(\cdot, t)\|_{L^2(\omega)} + C_1(\omega) \|\partial_t h(\cdot, t)\|_{H^{-1}(\omega)} \}. \quad (3.22)$$

Suppose h appears only in R.H.S. of equation (3.9) and so the functional ℓ depends on h , while B does not. This would be a typical case where, due to the linearity of the equation, (3.22) is enough to assure stability of p with respect to *small changes* on h . However, as h appears on the L.H.S. of equation (3.9), and so the bilinear form B also depends on h (thus, we had written $B(h)$), stability of the solution with respect to h requires some major development.

The next result is based in a similar analysis that can be found in [10].

To relax notation, for $f : \omega \times [0, +\infty)$ such that $f(\cdot, t)$ is in some normed space X , we denote

$$|f|_X = \|f(\cdot, t)\|_X.$$

Theorem 3.9. Suppose $p_1(\cdot, t), p_2(\cdot, t) \in H_0^1(\omega)$ accomplish the weak formulations of Reynolds equation for an arbitrary time $t \geq 0$:

$$\int_{\omega} h_1^3 \nabla p_1 \nabla \phi \, dA = \int_{\omega} h_1 \frac{\partial \phi}{\partial x} \, dA - 2 \int_{\omega} \frac{\partial h_1}{\partial t} \phi \, dA \quad \forall \phi \in H_0^1(\omega), \quad (3.23)$$

$$\int_{\omega} h_2^3 \nabla p_2 \nabla \phi \, dA = \int_{\omega} h_2 \frac{\partial \phi}{\partial x} \, dA - 2 \int_{\omega} \frac{\partial h_2}{\partial t} \phi \, dA \quad \forall \phi \in H_0^1(\omega). \quad (3.24)$$

Suppose also that both h_1 and h_2 , satisfying (3.12), are such that $0 < a_1 \leq h_1(\cdot, t) \leq b_1$, $0 < a_2 \leq h_2(\cdot, t) \leq b_2$ a.e. on ω with

$$|h_1 - h_2|_{L^\infty(\omega)} < \epsilon,$$

and $\partial_t h_1, \partial_t h_2 \in H^{-1}(\omega)$ are such that

$$|\partial_t h_1 - \partial_t h_2|_{H^{-1}(\omega)} < \epsilon'.$$

Then, the next estimate holds

$$\|p_1(\cdot, t) - p_2(\cdot, t)\|_{H_0^1(\omega)} \leq \frac{1}{a_2^3} \left\{ \epsilon \left[\frac{C(b_1 + b_2, \omega)}{a_1^3} (b_1 + |\partial_t h_1|_{L^2(\omega)}) + C(\omega) \right] + \epsilon' C(\omega) \right\}, \quad (3.25)$$

where $C(\cdot)$ are constants not depending on $h_1(\cdot, t) - h_2(\cdot, t)$ nor $\partial_t h_1(\cdot, t) - \partial_t h_2(\cdot, t)$.

Proof. Subtracting equation (3.24) from equation (3.23), rearranging terms and recalling the definition of $\ell(h)$ (with $h = h_1 - h_2$), for any $\phi \in H_0^1(\omega)$ we have

$$\int_{\omega} h_2^3 \nabla(p_1 - p_2) \nabla \phi \, dA = - \int_{\omega} (h_1^3 - h_2^3) \nabla p_1 \nabla \phi \, dA + \ell(h_1 - h_2; \phi),$$

taking $\phi = p_1 - p_2$ this can be written as

$$\int_{\omega} h_2^3 \nabla(p_1 - p_2)^2 dA = - \int_{\omega} (h_1^3 - h_2^3) \nabla p_1 \nabla(p_1 - p_2) dA + \ell(h; p_1 - p_2),$$

taking absolute value

$$\begin{aligned} a_2^3 |p_1 - p_2|_{H_0^1(\omega)}^2 &\leq |h_1^3 - h_2^3|_{L^\infty(\omega)} \left| \int_{\omega} \nabla p_1 \nabla(p_1 - p_2) dA \right| + |\ell(h; p_1 - p_2)| \\ &\leq |h_1^3 - h_2^3|_{L^\infty(\omega)} |p_1|_{H_0^1(\omega)} |p_1 - p_2|_{H_0^1(\omega)} + |\ell(h; p_1 - p_2)|. \end{aligned} \quad (3.26)$$

By equation (3.19) we have that

$$|\ell(h; p_1 - p_2)| \leq (|h_1 - h_2|_{L^2(\omega)} + C_1(\omega) |\partial_t(h_1 - h_2)|_{H^{-1}(\omega)}) |p_1 - p_2|_{H_0^1(\omega)},$$

replacing this in equation (3.26) we obtain

$$a_2^3 |p_1 - p_2|_{H_0^1(\omega)} \leq |h_1^3 - h_2^3|_{L^\infty(\omega)} |p_1|_{H_0^1(\omega)} + |h_1 - h_2|_{L^2(\omega)} + C_1(\omega) |\partial_t(h_1 - h_2)|_{H^{-1}(\omega)}. \quad (3.27)$$

The estimate

$$|h_1 - h_2|_{L^2(\omega)} \leq \mu(\omega)^{\frac{1}{2}} |h_1 - h_2|_{L^\infty(\omega)},$$

and

$$\begin{aligned} |h_1^3 - h_2^3|_{L^\infty(\omega)} &\leq |h_1^2 + h_1 h_2 + h_2^2|_{L^\infty(\omega)} |h_1 - h_2|_{L^\infty(\omega)} \\ &\leq C(b_1 + b_2, \omega) |h_1 - h_2|_{L^\infty(\omega)}, \end{aligned}$$

allow us to rewrite (3.27) as

$$a_2^3 |p_1 - p_2|_{H_0^1(\omega)} \leq \epsilon \left(C(b_1 + b_2, \omega) |p_1|_{H_0^1(\omega)} + C(\omega) \right) + \epsilon' C_1(\omega). \quad (3.28)$$

Now, we use the estimate (3.22) for p_1 , so we get

$$|p_1|_{H_0^1(\omega)} \leq \frac{C(\omega)}{a_1^3} (b_1 + |\partial_t h_1|_{L^2(\omega)}).$$

Finally, putting the last inequality in equation (3.28) we obtain the result. \square

3.2.2 Spatial regularity

From Sobolev Imbeddings (see Section §B.4, and Lemma B.14) we have that, for the two dimensional case ($n = 2$), the solution p is such that $p(\cdot, t) \in L^q(\omega) \forall q \in [2, \infty)$. For the case $n = 1$, we have an analogous weak formulation with analogous results, but

this time $p(\cdot, t) \in C_B^0(\omega)$. Moreover, by Theorem B.35 we have that if $h(\cdot, t) \in L^\infty(\Omega)$, $\partial_t h(\cdot, t) \in L^p(\Omega)$ and considering the hypothesis of Ω having finite measure and with Lipschitz boundary, if $u \in H_0^1(\Omega)$ is a weak solution of equations (3.9) and (3.10) then $p \in C^{0,\alpha}(\bar{\Omega})$, and

$$\|p\|_{C^{0,\alpha}(\bar{\Omega})} \leq C (|\partial_t h|_{L^p(\Omega)} + |h|_{L^{2p}(\Omega)}) .$$

where the constant C depends only on n, p, α, Ω and h .

Remark 3.10. The hypothesis made for h in (3.14) give us a huge freedom for treating much more complex surfaces than those considered on the classical formulation.

Remark 3.11. Galerkin's Methods is a robust family of methods for solving variational problems as the one presented in this section. Those methods use the rich structure of $H_0^1(\omega)$ as a Hilbert space whose elements can be approximated by smooth functions. We recommend [12] for an approach to that theory.

3.3 Maximum Principle for Reynolds equation

The Maximum Principle is an important feature of elliptic PDEs that distinguishes them from equations of higher order and systems of equations. In order to establish it, we define first a notion of inequality at the boundary for functions in the Sobolev Space $H^1(\omega)$. Let us say that $u \in H^1(\omega)$ satisfies $u \leq 0$ on the boundary $\partial\omega$ if its positive part $u^+ = \max\{u, 0\} \in H_0^1(\omega)$, which is equivalent to $u^+|_{\partial\omega} = 0$ (see the properties of the trace operator in Appendix B). If u is continuous in a neighborhood of $\partial\omega$, then u satisfies $u \leq 0$ on $\partial\omega$ if the inequality holds in the classical pointwise sense. We say that $u \geq 0$ on $\partial\omega$ if $-u \leq 0$ on $\partial\omega$, and $u \leq v$ (both in $H^1(\omega)$) on $\partial\omega$ if $u - v \leq 0$ on $\partial\omega$.

Theorem 3.12. Let $p \in H^1(\omega)$ satisfy

$$\nabla \cdot (h^3 \nabla p) \leq 0 (\geq 0), \quad \text{in } \omega,$$

in the weak sense, where h satisfies (3.14). Then

$$\inf_{\omega} p \geq \inf_{\partial\omega} p^-, \quad \left(\sup_{\omega} p \leq \sup_{\partial\omega} p^+ \right).$$

The proof of this theorem can be found in Chapter 8 of [87] and it is based on the boundedness of h and the ellipticity of the equation.

As an example, stationary Reynolds equation can be written as

$$\nabla \cdot (h^3 \nabla p) = \partial_x h,$$

including the condition $p = 0$ in $\partial\omega$ and supposing the geometry is convergent (divergent) everywhere, i.e., $\partial_x h \leq 0$ (≥ 0) on ω , the maximum Principle establishes that p must be non-negative (non-positive) over all ω .

Figure 3.2 shows two instances of 1D lubrication on the domain $\omega = [0, 1]$ with boundary conditions $p(0) = p(1) = 0$. The first geometry have bounds between $y = 0$ and the linear represented by the continuous red line. Thus, as the velocity is assumed to be positive ($S = 1$), the first geometry corresponds to a convergent geometry. Its corresponding pressure profile is represented by the dashed red line. The pressure profile is non-negative as the Maximum Principle establishes. On the other hand, a divergent geometry and its non-positive pressure profile are represented by the blue line and the dashed blue line resp.

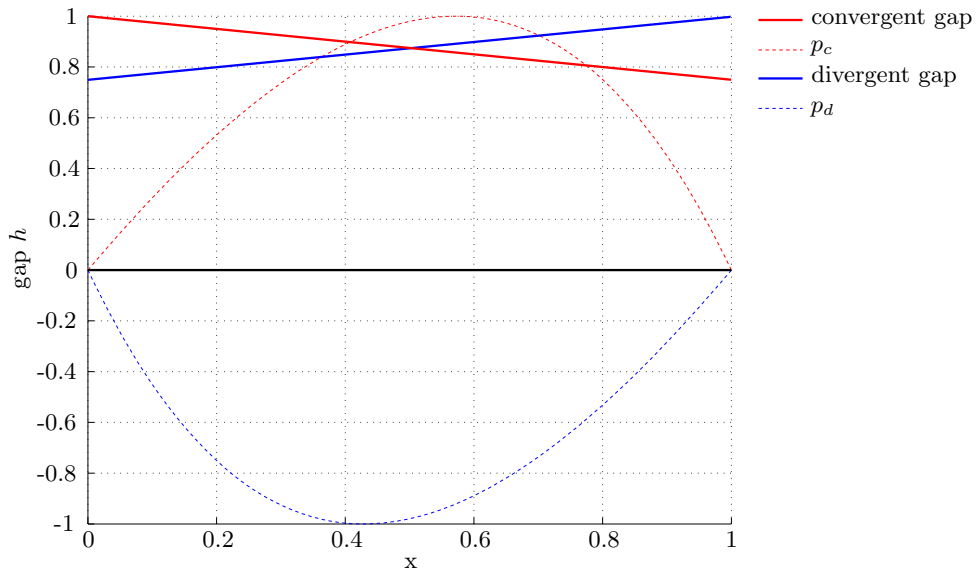


FIGURE 3.2: Disc pad scheme and pressure profile. p_c (p_d) is the pressure corresponding to the convergent (divergent) gap.

Moreover, there is a stronger result

Theorem 3.13. *Let $p \in C^2(\omega) \cap C^0(\bar{\omega})$, $h \in C^1(\bar{\omega})$ and*

$$\nabla \cdot (h^3 \nabla p) \leq 0 (\geq 0), \quad \text{in } \omega,$$

in the classical sense on ω , which is of class C^1 . Then if u achieves its minimum (maximum) at the interior of ω , u is constant.

The proof of this theorem can be found in Section 3.2 of [87].

Chapter 4

Cavitation and cavitation models

In Chapter 3 we have studied well-posedness of Reynolds equation in a subdomain $\omega \subset \Omega$, where $\Omega \subset \mathbb{R}^2$ is a measurable bounded domain. In this Chapter, we extend our study to the rest of the domain. As a consequence, $\Omega \setminus \omega$ will be a special area where Reynolds equation does not apply. That area will be called *cavitated region* and its existence is related to the incapability of fluids to sustain negative pressures below some threshold called *cavitation pressure*. The boundary $\partial\omega$ will be a new unknown of the problem determined by the cavitation model we choose.

4.1 Basic cavitation physics

Cavitation is a non-linear dynamic phenomenon that consists in the appearance, growth and collapse of *cavities* or *bubbles* in fluids due to an adiabatic process. Contrary to what happens in *boiling*, where the appearance of vapor bubbles takes place due to a rise in temperature, cavitation appears when low pressures are reached at constant temperature.

Vaporous cavitation takes place when pressure reaches the vapor pressure of the fluid. Similarly, *Gaseous cavitation* happens when pressure reaches the saturation pressure of gases dissolved in the fluid, Figure 4.1 shows an illustration of it.

Among others [59], the consequences of cavitation can be: damage on the surface boundaries; extraneous effects, like noise and vibrations of the mechanisms involved with the flow; hydrodynamic effects due to the interruption of the continuity of the fluid phase.

Cavitation modeling is a keystone when studying lubrication of tribological systems with textured surfaces, such as Journal Bearings or Piston-Ring/Liner [71, 5]. As an instance

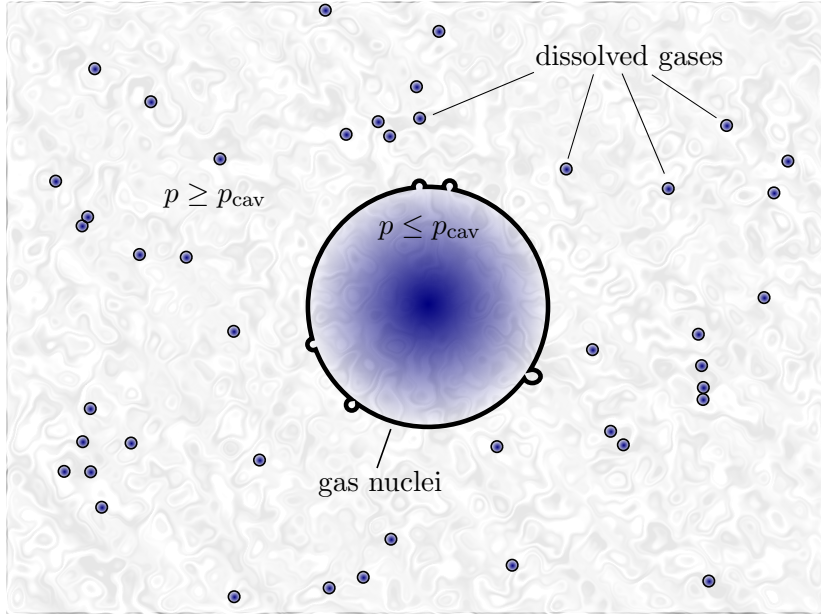


FIGURE 4.1: Illustration of gaseous cavitation. In the cavitated zone the pressure is lower than some threshold $p < p_{\text{cav}}$.

of this, in Section §4.5.1 we present the *Pure Squeeze Motion problem*, which is a well known benchmark problem for cavitation modeling [67, 5].

Half-Sommerfeld cavitation model is the simplest cavitation model that can be found in literature. It was proposed by Gümbel in 1921 [53] based on a previous work made by Sommerfeld in 1904 [83]. Half-Sommerfeld cavitation model consists in solving Reynolds equation in the whole domain Ω with Dirichlet boundary conditions $p = 0$, and once the pressure is obtained, at any point where $p < 0$ the condition $p = 0$ is imposed. In the next sections we describe the more sophisticated Reynolds and Elrod-Adams cavitation models.

4.2 Reynolds model

Half-Sommerfeld model is a very simple model that suffers of an important defect: even when considering stationary states, half-Sommerfeld model does not accomplish mass-conservation. For showing this, first note that the non-dimensional mass flux function for one dimensional Reynolds equation is given by

$$J = -\frac{h^3}{2} \frac{\partial p}{\partial x} + S \frac{h}{2}, \quad (4.1)$$

and, for any function, define the limits

$$f_{\pm}(x) = \lim_{\epsilon \rightarrow 0^{\pm}} f(x \pm \epsilon).$$

This way, mass-conservation in any point $x \in \Omega$ can be written as

$$J_+(x) - J_-(x) = 0.$$

Suppose $\zeta \in \partial\omega$ and the cavitated zone (given by half-Sommerfeld) is placed at right of ζ (see Figure 4.2). Suppose also that h is continuous at ζ . Then, we have

$$\left(\frac{\partial p}{\partial x} \right)_+ = 0, \quad \left(\frac{\partial p}{\partial x} \right)_- < 0,$$

so

$$J_+(\zeta) - J_-(\zeta) = \frac{h^3}{2} \left(\frac{\partial p}{\partial x} \right)_- < 0,$$

where lack of mass conservation can be observed.

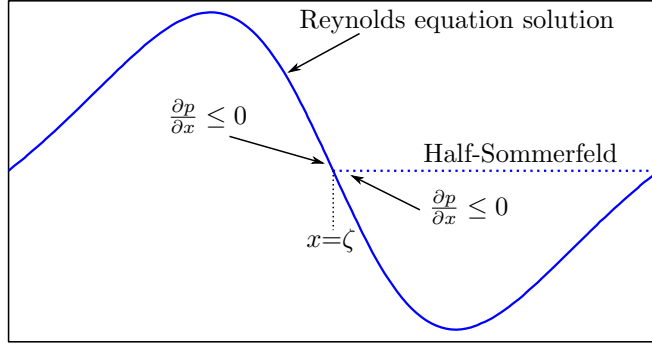


FIGURE 4.2: Scheme of a solution using Half-Sommerfeld cavitation model.

Swift H.W. in 1931 and Stieber W. in 1933 formulated mathematically a film rupture condition first suggested by Reynolds in 1886 (*apud* Dowson et al. [35]). Nowadays, these conditions are known as the Reynolds cavitation model. This model imposes the condition

$$\left(\frac{\partial p}{\partial x} \right)_+ = \left(\frac{\partial p}{\partial x} \right)_- = 0, \quad \text{in } \partial\omega. \quad (4.2)$$

These conditions are commonly used in the literature for defining Reynolds model [18, 35, 11]. In Section §4.2.1 we study this model from another point of view, beyond these boundary conditions.

4.2.1 Variational Formulation for Reynolds cavitation model

We present here the Reynolds cavitation model by using a variational formulation. This can be found, for instance, in founding works of Kindel Lehrer and Stampacchia, which are summarized in [58]. In the same context, in [8] it can be found an interesting comparison with Elrod-Adams model.

The half-Sommerfeld model was the first attempt to consider cavitation along with Reynolds equation. The heuristics of this model is simple: solve Reynolds equation and then cut off every pressure below some threshold p_{cav} (for simplicity, hereafter we take $p_{\text{cav}} = 0$). Reynolds model attempts to introduce this threshold in a smooth way, i.e., we may ask: given Reynolds equation and a domain Ω , can we find a solution of this equation such that p is non-negative? If the answer is positive, how does the nature of the mathematical problem change?

The obstacle problem

Trying to answer this last question we arrive to a general way of considering restrictions to PDE's: *Variational Inequalities*. A typical example of this kind of formulations arises when modeling the deformation of an elastic membrane and some obstacle restricts the deformation, as Figure 4.3 shows.

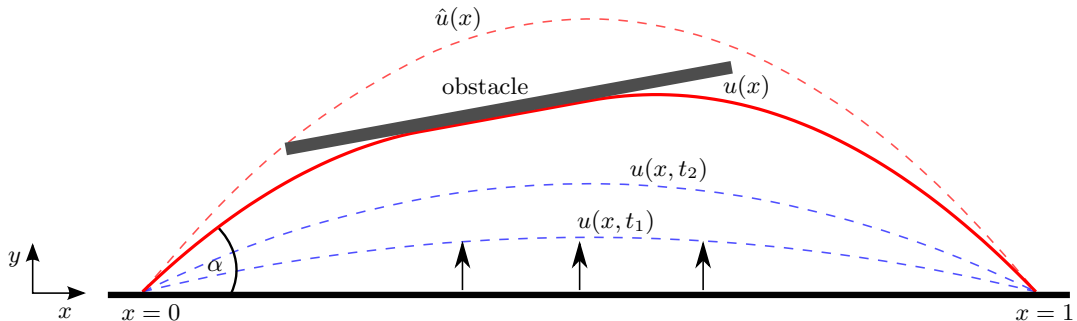


FIGURE 4.3: Obstacle problem for an elastic membrane. The black arrows represent the force applied on the membrane surface. $t_1 < t_2$ are two time steps of its evolution. $u(x)$ (red continuous line), $\hat{u}(x)$ (red dashed line) are the final states with the obstacle presence and without it resp.

Let us describe the 1D modeling of the obstacle problem. Denote by $u(x, t)$ the position of the membrane at time t . The ends of the membrane are fixed in such a way that

$$u(x = 0, t) = u(x = 1, t) = 0 \quad \forall t \geq 0.$$

Also, denote by $u(x) = \lim_{t \rightarrow \infty} u(x, t)$ the limit deformation of the membrane on time. Without the presence of an obstacle, the deformation of the membrane is modeled by the problem of finding $u : [0, 1] \rightarrow [0, +\infty)$ such that

$$\begin{aligned} -T \left(\frac{u'(x)}{\sqrt{1+u'(x)^2}} \right)' &= f(x), \quad \text{in } (0, 1) \\ u(0) = u(1) &= 0, \end{aligned}$$

where $f(x)$ is the force per unit of length applied on the membrane surface, and T is a parameter related to the tension on the membrane surface. If the deformations are small, i.e., $\alpha \approx 0$ in figure 4.3, the last equation can be approximated by the Poisson equation with boundary conditions

$$\begin{aligned} -T u''(x) &= f(x) \quad \text{in } (0, 1) \\ u(0) = u(1) &= 0. \end{aligned}$$

When an obstacle is present, we model the displacement of the membrane by finding $u : [0, 1] \rightarrow [0, +\infty)$ such that

$$\begin{aligned} -T u''(x) &= f(x) \quad \text{whenever } u(x) < \psi(x) \\ u(x) &\leq \psi(x) \quad \text{in } (0, 1) \\ u(0) = u(1) &= 0, \end{aligned}$$

where $\psi > 0$ is the function that describes the obstacle.

The variational formulation of this obstacle problem is similar to the one given by equation (3.21). In fact, using the same notation as before, it reads

$$B(u, \phi - u) \geq \langle f, \phi - u \rangle, \quad \forall \phi \in K, \tag{4.3}$$

where this time $K = K(\psi)$ is defined by

$$K = \{v \in H_0^1(0, 1) : v \leq \psi\},$$

and B is the coercive bilinear form on $H_0^1(0, 1)$ given by

$$B(u, v) = \int_0^1 u'(x)v'(x) dx.$$

Reynolds cavitation model as a variational inequality

In Section §3.2 we established the next variational formulation: find $p(\cdot, t)$ such that equation (3.13) is satisfied for any $\phi \in H_0^1(\omega)$, where t is a parameter. However, this time we are not looking for a solution in $H_0^1(\omega)$ since, as discussed before, $p = 0$ is a “physical obstacle” for the hydrodynamic pressure. Instead, let us define

$$K = \{v \in H_0^1(\Omega) : v \geq 0\}, \quad (4.4)$$

and seek for a function $p(\cdot, t) \in K$ such that

$$\int_{\Omega} h^3 \nabla p \nabla (\phi - p) dA \geq \int_{\Omega} h \frac{\partial}{\partial x} (\phi - p) dA - 2 \int_{\Omega} \frac{\partial h}{\partial t} (\phi - p) dA, \quad \forall \phi \in K. \quad (4.5)$$

This variational inequality is well known [26, 58] and we will name it *variational formulation* of the Reynolds cavitation model.

As in the case of Section §3.2, for assuring existence and uniqueness of $p(\cdot, t) \in K$ such that equation (4.5) is fulfilled, all we need is $\frac{\partial h}{\partial t}(\cdot, t) \in H^{-1}(\Omega)$ and $h(\cdot, t) \in L^\infty(\Omega)$ as the Stampacchia Theorem B.8 establishes. Thus, we can relax the hypothesis on h for the variational formulation of Reynolds equation. The regularity of the solution is studied, for instance, in [58] and a particular result due to Rodrigues [78] is given in Theorem B.36.

Distributional equations of Reynolds model

Here we suppose $p \in H_0^1(\Omega) \cap H^2(\Omega)$ is solution of equation (4.5), $h \in H^1(\Omega) \cap L^\infty(\Omega)$ and $\partial_t h \in L^2(\Omega)$.

What would we obtain starting from the variational formulation of Reynolds cavitation model and some suitable regularity hypothesis?

Integrating by parts equation (4.5) we get

$$\int_{\Omega} \left\{ \nabla \cdot (-h^3 \nabla p) + \frac{\partial h}{\partial x} + 2 \frac{\partial h}{\partial t} \right\} (\phi - p) dA \geq 0, \quad \forall \phi \in K, \quad (4.6)$$

where we have used Theorem B.26 and the fact that $\phi - p \in H_0^1(\Omega)$. Remember the definition *pressurized zone* and *cavitated zone* reads

$$\omega = \{(x, y) \in \Omega : p(x, y) > 0\} \quad \text{and} \quad \Omega \setminus \omega$$

resp.. It can be proved that $\Omega \setminus \omega$ is closed and ω is open [58]. We also assume $\partial\omega$ is locally Lipschitz.

Let us fix an arbitrary $f \in C_0^\infty(\omega)$. As $p > 0$ in ω , there exist some $\epsilon > 0$ such that $p \pm \epsilon f \in K$, and so $p \pm \epsilon f = 0$ in $\Omega \setminus \omega$. Putting $\phi = p \pm \epsilon f$ in equation (4.6) we get

$$\epsilon \int_\omega \left\{ \nabla \cdot (-h^3 \nabla p) + \frac{\partial h}{\partial x} + 2 \frac{\partial h}{\partial t} \right\} (\pm f) dA \geq 0,$$

so we obtain

$$\int_\omega \left\{ \nabla \cdot (-h^3 \nabla p) + \frac{\partial h}{\partial x} + 2 \frac{\partial h}{\partial t} \right\} f dA = 0, \quad \forall f \in C_0^\infty(\omega)$$

thus, from Lemma B.17 we obtain

$$\nabla \cdot (h^3 \nabla p) = \frac{\partial h}{\partial x} + 2 \frac{\partial h}{\partial t}, \quad \text{a.e. in } \omega. \quad (4.7)$$

We have recovered Reynolds equation (in distributional sense) in the pressurized zone ω .

To obtain an equation on $\Omega \setminus \omega$, take any function $\psi \in C_0^\infty(\Omega \setminus \omega) : \psi \geq 0$, so $\psi + p \in K$. Putting $\phi = \psi + p$ in equation (4.6) we obtain

$$\int_{\Omega \setminus \omega} \left(\frac{\partial h}{\partial x} + 2 \frac{\partial h}{\partial t} \right) \psi dA \geq 0 \quad \forall \psi \in C_0^\infty(\Omega \setminus \omega) : \psi \geq 0$$

this way, by using Lemma B.18 we get

$$\frac{\partial h}{\partial x} + 2 \frac{\partial h}{\partial t} \geq 0 \quad \text{a.e. in } \Omega \setminus \omega. \quad (4.8)$$

Remark 4.1. In fact, for some cases it is possible to show that $\partial_x h + 2 \partial_t h = \mu$ in ω_0 , where μ is a non-negative Radon measure with support in ω_0 . The interested reader may review Section “The Obstacle Problem: First Properties” in [58].

Remark 4.2. For the stationary case, equation (4.8) implies $\frac{\partial h}{\partial x} \geq 0$ in ω_0 . Therefore, Reynolds cavitation model only accepts cavitated regions placed at zones of divergent geometry. Analogously, for the pure squeeze motion, since the transport velocity is null the term $\partial_x h$ does not appear, then we have $\partial_t h \geq 0$, which also means that cavitation only take place at zones of divergent geometry.

Implied boundary conditions for Reynolds model in stationary state

We seek for the boundary conditions Reynolds model implies for the stationary 1D case. The main hypothesis will be continuity of the gap function h . In 1D Reynolds model

reads

$$\int_{\Omega} \left(h^3 \frac{\partial p}{\partial x} - h \right) \frac{\partial}{\partial x} (\phi - p) dx \geq 0, \quad \forall \phi \in K$$

where $\Omega = [a, b]$. Suppose $z \in \Sigma$ is a point placed at the boundary of the cavitated region such that $p(y) > 0$ if $z - \epsilon < y < z$ and $p(y) = 0$ if $z \leq y < z + \epsilon$ for some $\epsilon > 0$ small enough. The variational formulation implies that for any $\phi \in H_0^1(V)$, $\phi \geq 0$, with $V = [z - \epsilon, z + \epsilon]$, we have

$$\int_{z-\epsilon}^{z+\epsilon} \left(h^3 \frac{\partial p}{\partial x} - h \right) \frac{\partial}{\partial x} (\phi - p) dx \geq 0,$$

we split the domain as

$$\int_{z-\epsilon}^z \left(h^3 \frac{\partial p}{\partial x} - h \right) \frac{\partial}{\partial x} (\phi - p) - \int_z^{z+\epsilon} h \frac{\partial}{\partial x} (\phi - p) dx \geq 0.$$

Assuming $h \in H^1(V)$ and $p \in H^2(V)$, we integrate by parts (using Theorem B.26) to obtain

$$\int_{z-\epsilon}^z \frac{\partial}{\partial x} \left(h^3 \frac{\partial p}{\partial x} - h \right) (\phi - p) + \left(h^3 \frac{\partial p}{\partial x} - h \right)_- \phi(z) + \int_z^{z+\epsilon} \phi \frac{\partial}{\partial x} h dx + (h)_+ \phi(z) \geq 0,$$

where the sub-indices “-” and “+” denote the limits by the left and right of z resp.. By equation (4.7), the first integral is null. And assuming h is continuous ($h_- = h_+$) in z we obtain

$$\left(h^3 \frac{\partial p}{\partial x} \right)_- \phi(z) + \int_z^{z+\epsilon} \phi \frac{\partial}{\partial x} h dx \geq 0,$$

taking $\phi(z) > 0$ and making ϵ tends to zero we obtain $\left(h^3 \frac{\partial p}{\partial x} \right)_- \geq 0$, which implies

$$\left(\frac{\partial p}{\partial x} \right)_- \geq 0$$

however, since p is positive at the left of z , we must have $\left(\frac{\partial p}{\partial x} \right)_- \leq 0$ so we obtain the well known boundary condition of Reynolds model

$$\left(\frac{\partial p}{\partial x} \right)_- = 0.$$

Therefore, if we have enough regularity on the solution, we recover condition equation (4.2), which is typically found in literature defining Reynolds cavitation model. A scheme of this condition for the 2D case is shown in figure 4.4.

Remark 4.3. A more detailed proof (by using Theorem B.37) of the continuity of $\partial_x p$,

allowing the obstacle to have discontinuities of the type $\partial_x \psi(x^-) \leq \partial_x \psi(x^+)$, can be found in Section 7, Chapter II of [58].

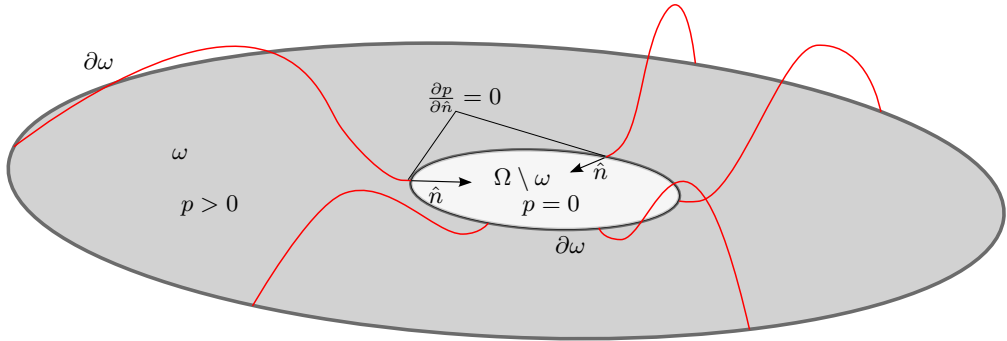


FIGURE 4.4: Scheme of a 2D cavitated domain. The red lines represent the pressure going to zero smoothly near ω_0 (cavitated zone) when h is sufficiently smooth.

4.3 Mass conservation in cavitation models

In the last years, mass-conservation has been proved to be a key issue in the study of tribological systems involving textured surfaces. When considering textured surfaces, Ausas et al. [5] showed that Reynolds model makes a large underestimate of the cavitating area leading to inaccuracies in the calculated friction. This was done comparing the results of Reynolds model to the ones returned by Elrod-Adams model, which enforces mass-conservation. Y. Qiu and M. Khonsari [74] also compared cavitation models, they showed that due to the underestimate of the cavitated zone, Reynolds model overestimates the load-carrying capacity when compared to Elrod-Adams model. Also, they showed a good correspondence between the cavitated zone found experimentally, in dimples made over a rotating disk, and the cavitated zone predicted by Elrod-Adams model. Consequently, it is interesting to study mass-flux behavior when considering Reynolds model, as this can give us baseline knowledge for understanding the mass-conservative model of Elrod-Adams.

For simplicity, in this section we will consider the one dimensional lubrication problem. Thus, taking the non-dimensional transportation velocity S equal to the unity, Reynolds equation reads

$$\frac{\partial}{\partial x} \left(h^3 \frac{\partial p}{\partial x} - h \right) = 0.$$

Now, consider the flux function of Reynolds model

$$J = -\frac{h^3}{2} \frac{\partial p}{\partial x} + \frac{h}{2}.$$

By equation (4.7) we know that in the pressurized zone ω , mass conservation is assured at any point since

$$\frac{\partial J}{\partial x} = 0, \quad \text{in } \omega.$$

However, by equation (4.8) and the condition $p = 0$, we know that in the cavitated zone

$$\frac{\partial J}{\partial x} = \frac{1}{2} \frac{\partial h}{\partial x} \geq 0, \quad \text{in } \Omega \setminus \omega.$$

We observe that when the mass-flux is passing through a diverging region of the geometry ($\partial_x h > 0$) there is an artificial mass-influx. Let us define as *rupture point* a point of $x \in \partial\omega$ where the flux is “exiting” ω , i.e.,

$$\hat{e}_1 \cdot \hat{n} > 0,$$

where \hat{n} is the normal vector pointing outward ω . Analogously, define as *reformation point* a point of $\partial\omega$ where the flux is entering ω , i.e.,

$$\hat{e}_1 \cdot \hat{n} < 0.$$

Figure 4.5 shows an example of a lubrication problem where cavitation is present.

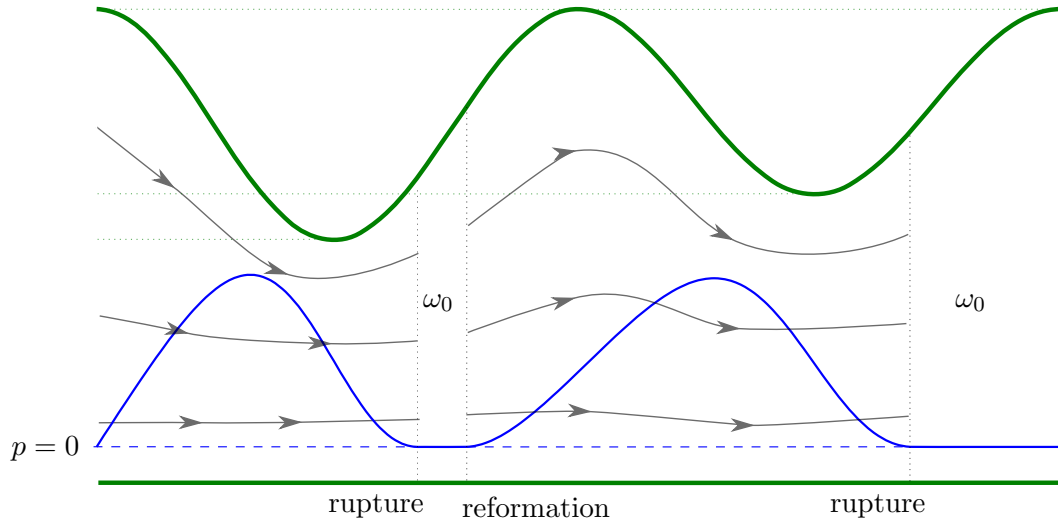


FIGURE 4.5: Rupture and deformation in a 1D tube section with Reynolds model. Black opaque lines represent the fluid flux. Notice the fluid flux “exiting” the pressurized region at the left rupture point and “re-entering” the pressurized region at the reformation point.

The blue continuous line represents the non-dimensional pressure. Please notice the condition of the normal derivative $\frac{\partial p}{\partial x} = 0$ on both rupture and reformation points.

We already know that in the full-film region we have $\frac{\partial J}{\partial x} = 0$ and thus mass-conversation holds. This is because the Poiseuille flux ($-\frac{h^3}{2} \frac{\partial p}{\partial x}$) compensates the Couette flux ($\frac{h}{2}$) on

that region. On the other hand, at the cavitated region there is no Poiseuille flux that could compensate Couette flux variations. This is why, as the cavitated region is placed at the divergent region, we have $\frac{\partial J}{\partial x} = \frac{\partial h}{\partial x} > 0$ on the cavitated region.

Observing Figure 4.5 one can hope that, if the surfaces being lubricated consist only of one pair of convergent and divergent zones, there will be only one cavitated region. Thus, the effect of the non-conservation of mass along the cavitated zone would be negligible. On the contrary, if there are several full-film regions sharing its boundaries with cavitated regions, the accumulated effect of the lack of mass-conservation might be important. Some good examples of this appear when considering textured surfaces, as can be found in [5]. Similar examples will be presented in the next section considering smooth textures.

4.4 Elrod-Adams model

In an effort for assuring mass-conservation, Jakobson [57], Olsson [66] and Floberg [40, 41] provided the base of a theory that nowadays is known as the Jakobson, Floberg and Olsson (JFO) cavitation theory (*apud* [11]). In these works the authors take into account the amount of liquid being transported through the cavitated zones, which can be important as suggested in the previous section.

Making use of JFO theory, Elrod and Adams [37] exposed a generalized Reynolds equation and an algorithm for solving it by introducing a new variable θ that represents the fraction of liquid content at each point of the domain [11]. The transported quantity for this model is $h\theta$. In the full-film region, or pressurized region, we have $p > 0$ and $\theta = 1$. In the cavitated region, we have $p = 0$ and $0 \leq \theta \leq 1$. Considering this new variable, the non-dimensional Reynolds equation for Elrod-Adams cavitation model is written (using scales analogous to those from Table 2.2 with time scale L/S)

$$\nabla \cdot \left(\frac{h^3}{2} \nabla p \right) - \frac{S}{2} \frac{\partial h\theta}{\partial x} = \frac{\partial h\theta}{\partial t}, \quad \text{in } \Omega, \quad (4.9)$$

where S is the non-dimensional relative velocity of the surfaces, which is supposed to develop along the x -axis.

This time the non-dimensional mass-flux function is given by (taking the transport velocity S equal to unity)

$$\vec{J} = -\frac{h^3}{2} \nabla p + \frac{h\theta}{2} \hat{e}_1, \quad \text{in } \Omega. \quad (4.10)$$

For stationary states, where the cavitation boundaries are not moving, the mass-flux entering $\Omega \setminus \omega$ at $\mathbf{x} \in \partial\omega$, and the mass-flux exiting ω at the same point can be written resp. as

$$\lim_{\epsilon \rightarrow 0^+} \vec{\mathbf{J}}(\mathbf{x} + \epsilon \hat{\mathbf{n}}) \cdot \hat{\mathbf{n}} \quad \text{and} \quad \lim_{\epsilon \rightarrow 0^+} \vec{\mathbf{J}}(\mathbf{x} - \epsilon \hat{\mathbf{n}}) \cdot \hat{\mathbf{n}},$$

where $\hat{\mathbf{n}}$ is the unitary vector pointing outward $\partial\omega$. Defining the limits in $\mathbf{x} \in \partial\omega$ for some function f

$$f_{\pm} = \lim_{\epsilon \rightarrow 0^+} f(\mathbf{x} \pm \epsilon \hat{\mathbf{n}}),$$

mass conservation implies the boundary conditions

$$\left(\lim_{\epsilon \rightarrow 0^+} \vec{\mathbf{J}}(\mathbf{x} + \epsilon \hat{\mathbf{n}}) - \lim_{\epsilon \rightarrow 0^+} \vec{\mathbf{J}}(\mathbf{x} - \epsilon \hat{\mathbf{n}}) \right) \cdot \hat{\mathbf{n}} = (h_+ \theta_+ - h_- \theta_-) \Sigma', \quad \forall \mathbf{x} \in \partial\omega.$$

where Σ' is the velocity at which $\partial\omega$ is moving. This condition is known as the *Rankine-Hugoniot Condition* for mass-conservation (see, e.g., [61]). So the boundary condition can also be written

$$(\vec{\mathbf{J}}_+ - \vec{\mathbf{J}}_-) \cdot \hat{\mathbf{n}} = (h_+ \theta_+ - h_- \theta_-) \Sigma'. \quad (4.11)$$

If the system reaches an steady state (so $\Sigma' = 0$) and \mathbf{x} is a rupture point, this boundary condition implies

$$(-h_+^3 \nabla p_+ + (h\theta)_+ \hat{\mathbf{e}}_1 + h_-^3 \nabla p_- - (h\theta)_- \hat{\mathbf{e}}_1) \cdot \hat{\mathbf{n}} = 0 \quad \text{in } \mathbf{x},$$

as $h_- = h_+ = h$, $\theta_- = 1$, $\nabla p_+ = 0$ and $\hat{\mathbf{e}}_1 \cdot \hat{\mathbf{n}} > 0$ we have

$$h^3 \nabla p_- \cdot \hat{\mathbf{n}} = h(1 - \theta_+) \hat{\mathbf{e}}_1 \cdot \hat{\mathbf{n}} \geq 0$$

moreover, as p is positive in ω we have $\nabla p_- \cdot \hat{\mathbf{n}} \leq 0$ and so

$$\nabla p_- \cdot \hat{\mathbf{n}} = \left(\frac{\partial p}{\partial n} \right)_- = 0,$$

which is the same boundary condition of Reynolds model for rupture points. On the other hand, for reformation points ($\hat{\mathbf{e}}_1 \cdot \hat{\mathbf{n}} < 0$), applying condition (4.11) we obtain

$$h^3 \left(\frac{\partial p}{\partial n} \right)_+ = -h(1 - \theta_-) \hat{\mathbf{e}}_1 \cdot \hat{\mathbf{n}} \geq 0.$$

Observe that this condition is different from the one from Reynolds model. If on the left side of the reformation point the fluid is not complete ($\theta < 1$), a jump (or discontinuity) in the pressure gradient is developed in order to assure mass-conservation.

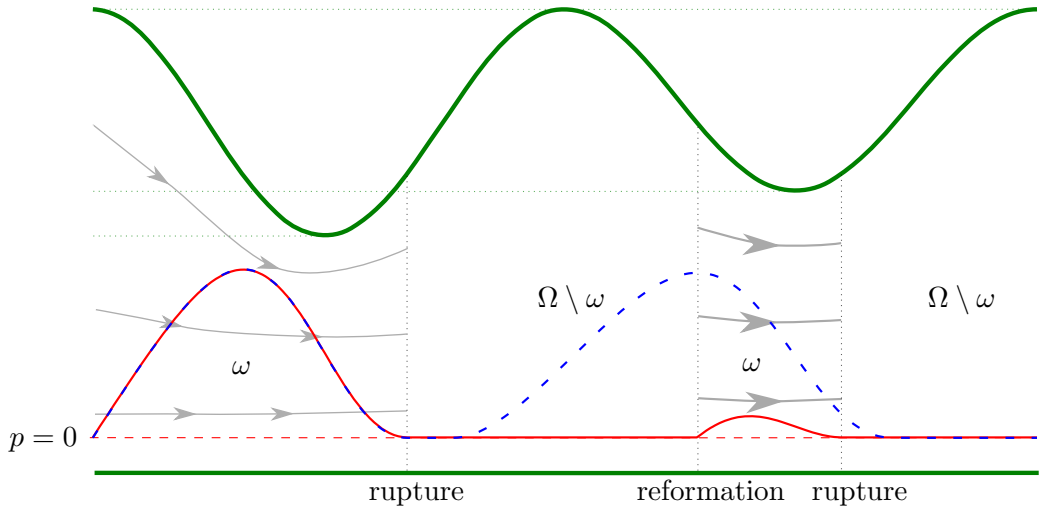


FIGURE 4.6: Rupture and reformation in a 1D tube section with Elrod-Adams model. Black opaque lines represent the fluid flux, the red line represents pressure from Elrod-Adams model and the blue-dashed line represents pressure from Reynolds model.

A simple comparison with Reynolds model

Figure 4.6 shows the same example we used for Reynolds model (see Figure 4.5), this time including Elrod-Adams solution. The red line and the blue-dashed line represent the pressure given by Elrod-Adams and Reynolds models resp.. We observe that both solutions coincide in the first convergent region (left side). However, the first cavitated region of Elrod-Adams model (left side) is much larger than the one from Reynolds model. The second cavitated region is also larger for Elrod-Adams model. All this leads to a smaller pressure integral for Elrod-Adams model on Ω .

Remembering that for Reynolds model $\frac{\partial J}{\partial x} = \frac{\partial h}{\partial x}$ in the cavitated region, we can make the next remark while observing Figure 4.5: the amount of fluid (Q_1) leaving the left pressurized region is bigger than the amount of fluid (Q_2) entering the right pressurized region. On the contrary, for Elrod-Adams model, the amount of fluid entering passing through all Ω is always Q_1 . This is why Reynolds model exhibits a larger pressure profile. This overestimation of pressure due to non mass-conservation of Reynolds model is also presented in [5, 74].

Finally, we remark that the Elrod-Adams model can also be written as a variational problem for the steady state. Its formulation is similar to the one exhibited for Reynolds model in Section §4.2.1 and the interested reader can find it in [7].

4.5 Analytical solution examples

4.5.1 Cavitation in Pure Squeeze Motion

In this section we illustrate the differences between cavitation models when solving a simple benchmark problem. Pure Squeeze Motion between two parallel surfaces is going to be used for this purpose. The scheme of the problem is showed in Figure 4.7.

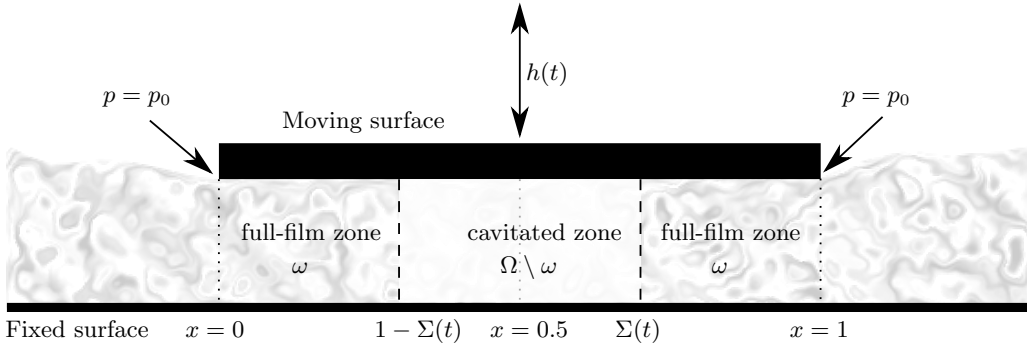


FIGURE 4.7: Pure Squeeze problem scheme.

The lower surface is at rest, while the upper surface has a known motion in such a way the space between the surfaces is equal to

$$h(t) = 0.125 \cos(4\pi t) + 0.375,$$

and the sliding velocity for both surfaces is null. Also, the boundary conditions for pressure are $p(x = 0, t) = p(x = 1, t) = p_0 = 0.025$.

Initially, we assume the space between the surfaces is fulfilled with fluid. Therefore, as immediately after $t = 0$ the gap h is shrinking, the pressure p is going to be positive (Strong Maximum Principle, Theorem 3.13) and we will have $\omega =]0, 1[$ and $\Omega \setminus \omega = \emptyset$. After that shrinking, the gap h will expand and so there will be some time t_{rup} at which the film ruptures and a cavitated zone appears.

In ω , Reynolds equation is valid and it can be written as

$$\frac{1}{2} \frac{\partial^2 p}{\partial x^2} = \frac{1}{h^3} \frac{\partial h}{\partial t}, \quad \text{in } \omega. \quad (4.12)$$

Thus, when the space between the surfaces diminish ($h'(t) < 0$) and cavitation is not taken into account, the minimal pressure fall below the boundary conditions (Strong Maximum Principle). When cavitation is taken into account, the models we already exposed consider that pressure reaches some threshold level p_{cav} , here we take $p_{\text{cav}} = 0$.

As the problem is symmetric around $x = 0.5$ in the x -axis, and the boundary conditions in $x = 0, 1$ are equal, the cavitated zone will also be symmetric around $x = 0.5$, i.e., $\Omega \setminus \omega = [1 - \Sigma(t), \Sigma(t)]$ where $\Sigma(t) \in [0.5, 1[$ is the right boundary of the cavitated zone.

Half-Sommerfeld model solution

In this case we only need to solve equation (4.12) in the whole domain $\Omega =]0, 1[$ and, for each time t , find the point $\Sigma \in [0.5, 1[$ such that $p(\Sigma) = 0$ (if there is any).

Reynolds model solution

For Reynolds model, we can integrate equation (4.12) on $]\Sigma(t), x[$ with $\Sigma(t) < x < 1$, so

$$\begin{aligned} \int_{\Sigma}^x \frac{\partial^2 p}{\partial x^2} dx &= \int_{\Sigma}^x 2 \frac{1}{h^3} \frac{\partial h}{\partial t} dx \\ h^3 (p'(x) - p'(\Sigma)) &= 2 \partial_t h (x - \Sigma), \end{aligned}$$

where $p' = \frac{\partial p}{\partial x}$ and we have used that h does not depend on x . Reynolds model implies $p'(\Sigma) = 0$, so integrating again on $]\Sigma, x[$ we obtain

$$p(x) = 2 \frac{\partial_t h}{h^3} \left(\frac{x^2 - \Sigma^2}{2} - \Sigma (x - \Sigma) \right), \quad x \in]\Sigma(t), 1[.$$

To find Σ , we use the boundary condition $p(1) = p_0$, so we have

$$h^3 p_0 = \partial_t h (1 - \Sigma)^2,$$

thus, for Reynolds model the cavitation boundary $\Sigma_r = \Sigma$ is given by

$$\Sigma_r(t) = 1 - \sqrt{\frac{p_0 h(t)^3}{\partial_t h(t)}}. \quad (4.13)$$

Elrod-Adams model solution

As we said above, initially the whole domain Ω will be pressurized. Let us denote by t_{rup} the time at which the cavitation begins. Denote also by t_{ref} the time for which the cavitated zone is growing at any time $t \in]t_{\text{rup}}, t_{\text{ref}}[$, which means that $\Sigma(t)$ is a rupture point on that time interval. Also, denote by t_{end} the time for which the cavitated zone disappears (if there is any), i.e., $]t_{\text{ref}}, t_{\text{end}}[$ is the time interval for which the cavitated zone is shrinking and $\Sigma(t)$ is a reformation point.

For $t \in [t_{\text{rup}}, t_{\text{ref}}[$, $\Sigma(t)$ is a rupture point. Thus, the boundary conditions $\partial_x p = 0$ at $\partial\omega$ are the same for Reynolds and Elrod-Adams model. Therefore, for Elrod-Adams model $\Sigma(t)$ is given by equation (4.13). But for $t \in]t_{\text{ref}}, t_{\text{end}}[$ that equality is not valid anymore.

To find Σ for $t \in]t_{\text{ref}}, t_{\text{end}}[$, we integrate equation (4.12) obtaining

$$h^3 (p'(x) - p'(\Sigma)) = 2 \partial_t h (x - \Sigma). \quad (4.14)$$

And using equation (4.11) we obtain the next mass-conservation condition on Σ :

$$h^3 p'(\Sigma) = 2 \Sigma' h (\theta_- - 1), \quad (4.15)$$

where Σ' is the velocity of Σ and θ_- is the value of the saturation θ just at the left of Σ . Putting this in equation (4.14) and integrating on $[\Sigma, x]$ we get

$$p(x) = \frac{2}{h^3} \left\{ \partial_t h \left(\frac{x^2 - \Sigma^2}{2} - \Sigma (x - \Sigma) \right) + \Sigma' h (\theta_- - 1)(x - \Sigma) \right\}. \quad (4.16)$$

In consequence, for finding p we need to calculate Σ . As before, we use the boundary condition $p(1) = p_0$ so we get the differential equation

$$\Sigma'(t) = \frac{(1 - \Sigma)^2 \partial_t h - p_0 h^3}{2 h (1 - \Sigma) (1 - \theta_-(\Sigma))}. \quad (4.17)$$

Where $\theta_-(\Sigma)$, the saturation just at the left of Σ , can be calculated by using the characteristic lines method as it is illustrated in Figure 4.8.

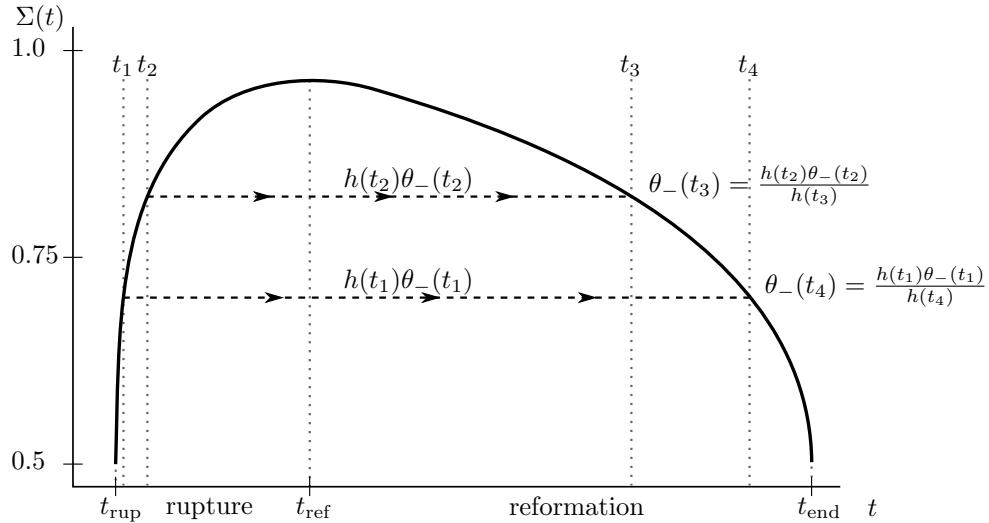


FIGURE 4.8: Characteristic lines of $h\theta$.

Using as initial condition $\Sigma(t_{\text{ref}}) = \Sigma_r(t_{\text{ref}})$, equation (4.17) allows to find the boundary

cavitation till the final time t_{end} . Finally, putting Σ and Σ' into equation (4.16) we can find the pressure field for the Elrod-Adams model.

Comparison of the solutions

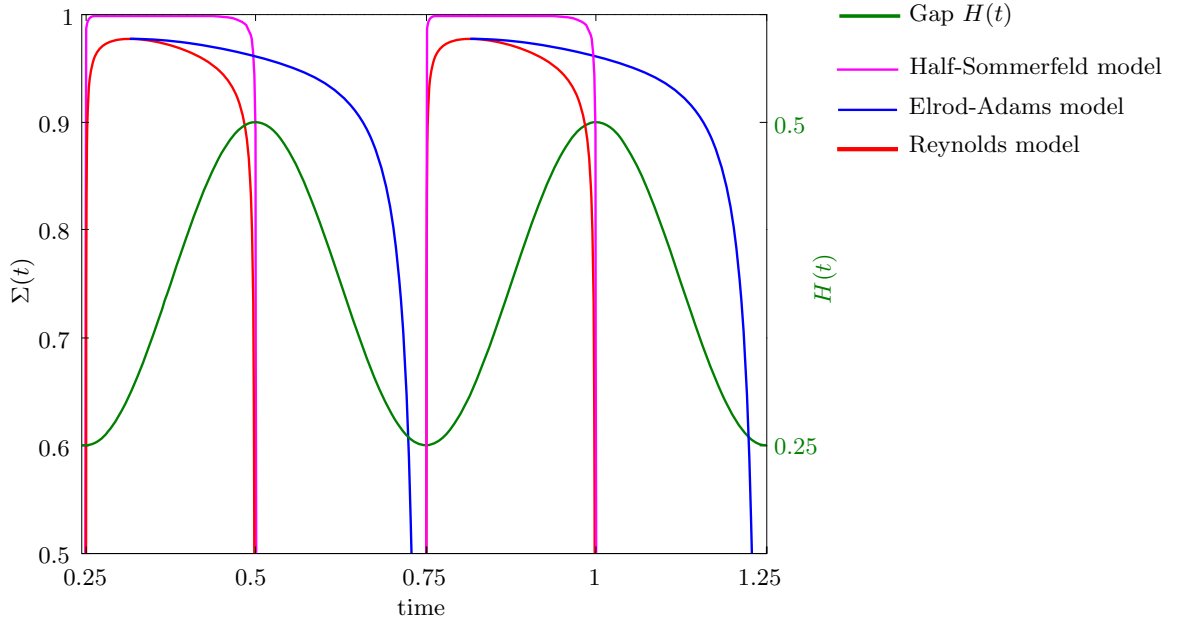


FIGURE 4.9: $\Sigma(t)$ for half Sommerfeld, Reynolds and Elrod-Adams cavitation models.
The thickness function $H(t)$ is shown the continuous sinusoidal line.

All models considered here show a rupture in the full-film region at time $t = 0.25$, just when the space between the surfaces begins to expand (see Figure 4.9). By the other hand, the collapse of the cavitated region is totally different when considering Elrod-Adams model. At time $t = 0.5$, the upper surface is stopped, and immediately after that time the distance $h(t)$ will begin to shrink. When this occurs, both Half-Sommerfeld and Reynolds models show a collapse of the cavitated zone, for both models there is no cavitated zone until a rupture reappears at time $t = 0.75$, when the distance $h(t)$ begins to expand again. On the contrary, the cavitated zone resulting from Elrod-Adams model does not collapse at $t = 0.5$ but it remains until approximately $t = 0.73$. Elrod-Adams model predicts the presence of cavitation at great part of the time at which the space $h(t)$ is shrinking!.

4.5.2 Cavitation in a flat pad with a traveling pocket

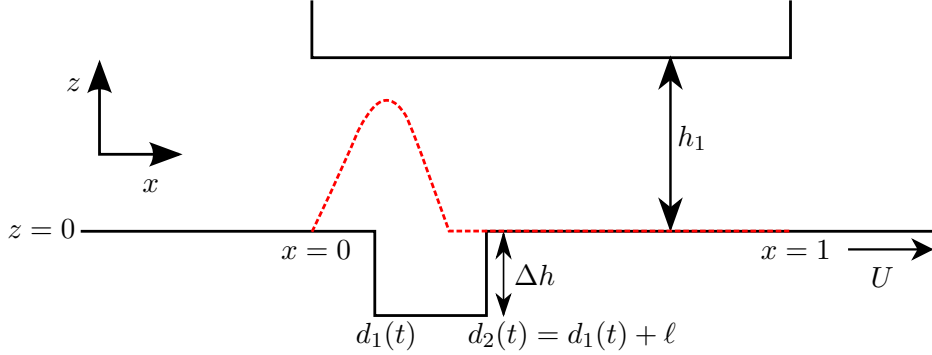


FIGURE 4.10: Scheme of the problem. The dashed red line illustrates the pressure profile.

In this section we study a 1D problem consisting of two parallel surfaces in relative motion. As Figure 4.10 shows, the upper surface is flat and it is placed between $x = 0$ and $x = 1$. The lower surface is flat and placed at distance h_1 from the upper one, except for a pocket of depth $\Delta h = h_2 - h_1$ and length ℓ . This pocket is traveling at the same sliding speed U of the lower surface. The pocket's left side position is denoted by $d_1(t)$ and its right side is denoted by $d_2(t) = d_1(t) + \ell$.

At time $t = 0$, we assume the pocket is just entering the region $\Omega =]0, 1[$, which is written $d_1(t = 0) = -\ell$. Also, we assume fully flooded conditions on $x = 0$ and null pressure on $x = 1$, i.e.,

$$p(0, t) = p(1, t) = 0, \quad \theta(0, t) = 1, \quad \forall t > 0. \quad (4.18)$$

Reynolds model solution

As the pocket travels along $\Omega = [0, 1]$ with constant velocity S , the gap function is described by $h(x, t) = h(x - St)$ and we have $\partial_t h = -S \partial_x h$. This way, Reynolds equation for this problem reads

$$\frac{\partial}{\partial x} \left(h^3 \frac{\partial p}{\partial x} \right) = -S \frac{\partial h}{\partial x}, \quad \forall t \geq 0, \text{ on } \Omega.$$

Also, the gap function can be written as

$$h(x, t) = h_1 + \Delta h (H(x + l - St) - H(x - St)),$$

where $H(x)$ is the Heaviside function ($H(x) = 0$ if $x < 0$, $H(x) = 1$ otherwise), which weak derivative is the Dirac's delta distribution $\frac{\partial H(x)}{\partial x} = \delta(x)$. With all this, we can

write Reynolds equation as

$$\frac{\partial}{\partial x} \left(h^3 \frac{\partial p}{\partial x} \right) = -S\Delta h (\delta(x + \ell - St) - \delta(x - St)), \quad \forall t \geq 0, \text{ on } \Omega. \quad (4.19)$$

For $t < \ell/S$, before the pocket enters completely into Ω , equation (4.19) can be written as:

$$\frac{\partial}{\partial x} \left(h^3 \frac{\partial p}{\partial x} \right) = S\Delta h \delta(x - d_2), \quad \text{for } 0 < t < \ell/S, \text{ on } \Omega,$$

where we have used that $d_2(t) = St$. So, as the right hand side of this last equation is positive, we must have $p \leq 0$ because of the boundary conditions and the Maximum Principle, and so, as we are looking for non-negative pressures we have $p = 0$ in Ω . This result is clear from the observation that for $t < \ell/S$ the geometry is strictly divergent.

For $\ell/S < t < 1/S$, the time interval for which the pocket is completely inside Ω , we integrate equation (4.19) obtaining

$$\frac{\partial p}{\partial x} = \frac{C}{h^3} - \frac{S\Delta h}{h^3} (H(x - d_1) - H(x - d_2)). \quad (4.20)$$

As $H_0^1(0, 1) \subset C^0(0, 1)$ (see Section §B.4), this equation means that p is a piecewise linear and continuous function that changes its slope only at $x = d_1(t)$ and $x = d_1(t) + \ell$. Now, outside the pocket equation (4.20), can be written

$$\frac{\partial p}{\partial x} = \frac{C}{h_1^3}, \quad \text{for } x < St - \ell \text{ or } St < x. \quad (4.21)$$

Since $p(0) = 0$ and p must be non-negative, we only can have $C \geq 0$. Analogously, as $p(1) = 0$ we must have $C \leq 0$, and so we have $C = 0$. Thus, as p is continuous, p must be null on Ω .

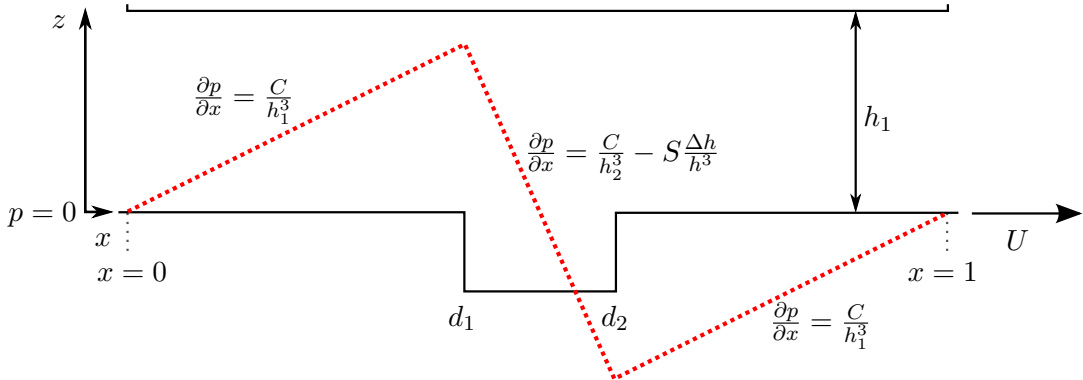


FIGURE 4.11: Scheme of the solution for a single honed pocket without cavitation.

As the reader may guess, something has gone wrong with our “solution procedure”

above. For illustrating our error let us reconsider the problem, this time without cavitation. From Figure 4.11 we infer that, for accomplishing equation (4.21), we need to allow negative pressures.

The error we made before was due to consider Reynolds equation as being valid through all Ω . But Reynolds equations is not valid on the cavitated zone $\Omega \setminus \omega$. Here, we will guess (based on the illustration of Figure 4.11) that the cavitated zone corresponds to $[d_2(t), 1]$ for any time t such that $\ell/S < t < 1/S$, and soon we will prove that such guess is correct. This way, the region where Reynolds equation is valid is written $\omega =]0, d_2[$, and the corresponding scheme of the solution is showed in Figure 4.12.

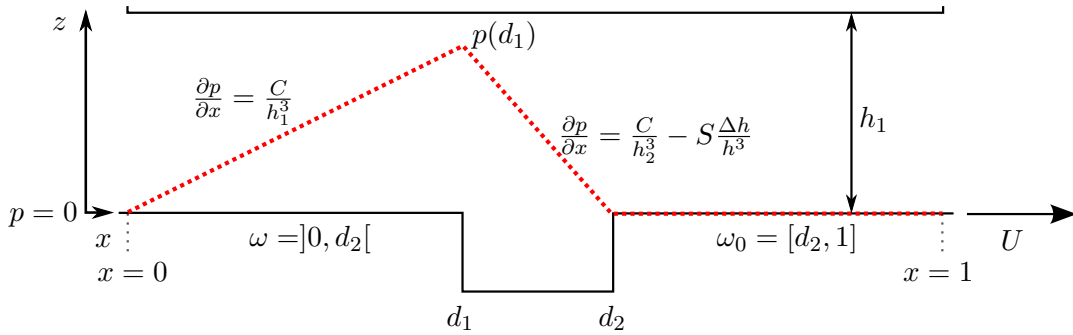


FIGURE 4.12: Scheme of an ansatz solution for a single honed pocket with Reynolds cavitation model.

Now, Reynolds equation is valid in ω and we write it as

$$\frac{\partial p}{\partial x} = \frac{C}{h^3} - \frac{S\Delta h}{h^3} H(x - d_1), \quad \text{on } \omega, \quad (4.22)$$

$$p(0) = p(d_2) = 0. \quad (4.23)$$

For finding C we integrate equation (4.22) along with the boundary conditions so we obtain

$$C = \frac{S\ell h_1^3 \Delta h}{d_1 h_2^3 + \ell h_1^3}, \quad (4.24)$$

and so

$$p(d_1) = \frac{S\ell d_1 \Delta h}{d_1 h_2^3 + \ell h_1^3}. \quad (4.25)$$

In the next proposition we prove that this is, in fact, the solution for Reynolds cavitation model.

Proposition 4.4. *Let $\ell/S < t < 1/S$, then, the piecewise linear function p defined by equation (4.22) on $\omega =]0, d_2[$ and the boundary conditions (4.23) along with $p = 0$ on $\omega_0 = [d_2, 1]$ is the solution of the Reynolds cavitation model for $\Omega = [0, 1]$.*

Proof. We need to prove that p accomplishes the variational formulation

$$\int_0^1 h^3 \partial_x p \partial_x (\phi - p) dx \geq S \int_0^1 h \partial_x (\phi - p) dx - 2 \int_0^1 (\phi - p) \partial_t h dx \quad \forall \phi \in K,$$

with $K = \{\phi \in H_0^1(0, 1) : \phi \geq 0\}$.

We integrate the identity $\partial_t h = -S \partial_x h$ and integrate by parts, obtaining

$$\int_0^1 h^3 \partial_x p \partial_x (\phi - p) dx \geq -S \int_0^1 h \partial_x (\phi - p) dx dx \quad \forall \phi \in K. \quad (4.26)$$

Denote by I_1 the integral of the left-hand side. We can decompose I_1 as

$$I_1 = \int_0^{d_1} h_1^3 \partial_x p \partial_x (\phi - p) dx + \int_{d_1}^{d_2} h_2^3 \partial_x p \partial_x (\phi - p) dx + \int_{d_2}^1 h_1^3 \partial_x p \partial_x (\phi - p) dx.$$

Using (4.22) in this last equation, and the fact that $p = 0$ on $[d_2, 1]$, we have

$$\begin{aligned} I_1 &= \int_0^{d_1} h_1^3 \partial_x p \partial_x (\phi - p) dx + \int_{d_1}^{d_2} h_2^3 \partial_x p \partial_x (\phi - p) dx \\ &= -\frac{C^2}{h_1^3} d_1 + (C - S \Delta h) (\phi(d_2) - \phi(d_1)) - \frac{l}{h_2^3} (C - S \Delta h)^2. \end{aligned} \quad (4.27)$$

Denoting by I_2 the integral of the right-hand side of equation (4.26) we have

$$I_2 = -S \left(\int_0^{d_1} h_1 \partial_x (\phi - p) dx + \int_{d_1}^{d_2} h_2 \partial_x (\phi - p) \partial_x (\phi - p) dx + \int_{d_2}^1 h_1 \partial_x (\phi - p) dx \right),$$

and using again (4.22) and $p = 0$ on $[d_2, 1]$ we obtain

$$I_2 = -S \Delta h (\phi(d_2) - \phi(d_1)) + S C \left(\frac{d_1}{h_1^2} + \frac{l}{h_2^2} \right) - S^2 \ell \frac{\Delta h}{h_2^2}. \quad (4.28)$$

Replacing equations (4.27) and (4.28) in equation (4.26), multiplying by $h_1^3 h_2^3$ and rearranging the terms we obtain

$$Ch_1^3 h_2^3 \phi(d_2) \geq h_1^3 \ell (C - S \Delta h)^2 + d_1 C^2 h_2^3 + S C (d_1 h_2^3 h_1 + \ell h_1^2 h_2) - S^2 \ell h_1^3 h_2 \Delta h,$$

as $C > 0$ and this inequality must hold for any $\phi(d_2) \geq 0$, this is equivalent to

$$h_1^3 \ell (C - S \Delta h)^2 + d_1 C^2 h_2^3 + S C (d_1 h_2^3 h_1 + \ell h_1^2 h_2) - S^2 \ell h_1^3 h_2 \Delta h \leq 0.$$

In fact, replacing $\Delta h = h_2 - h_1$ and C by its definition (4.24), we obtain that the left-hand side of the last inequality is equal to zero, and so the variational formulation holds for p . \square

Please observe that for $1 \leq t < 1 + \ell$ (while the pocket is exiting the domain), the pressure can be found just replacing the right side of the pocket, d_2 , by 1.

Elrod-Adams model solution

In this section we solve once more the problem of a flat pad with a traveling pocket, this time modeling cavitation through the Elrod-Adams model. We will find a significant qualitative difference between the solutions of both models.

For Elrod-Adams cavitation model, the modified non-dimensional Reynolds equation can be written as

$$\frac{\partial}{\partial x} \left(h^3 \frac{\partial p}{\partial x} \right) = S \frac{\partial h \theta}{\partial x} + 2 \frac{\partial h \theta}{\partial t}, \quad \text{on } \Omega = [0, 1], \quad (4.29)$$

where p the hydrodynamic pressure, θ the saturation field, h the gap function and S the velocity of the lower surface. This equation is not valid exclusively on the active region $\omega \subset \Omega$ but through all the domain Ω .

The variables that describe the pocket are the same as in the last section, i.e., the depth Δh and its right and left side, d_1 and d_2 resp.. Also, the initial position of the pocket is the same as before, $d_1(t = 0) = -\ell$.

The mass-conservation (Rankine-Hugoniot condition) condition at an arbitrary point $x \in \Omega$ moving at velocity V_x is written

$$\frac{S}{2} (h\theta)_+ - \frac{h^3}{2} \partial_x p_+ - \frac{S}{2} (h\theta)_- + \frac{h^3}{2} \partial_x p_- = ((h\theta)_+ - (h\theta)_-) V_x. \quad (4.30)$$

Let us remember that cavitation prevents pressure to take values below p_{cav} (here $p_{cav} = 0$), and the geometry is divergent for $0 < t < \ell/S$. This way, it is clear that the solution for pressure, while the pocket is entering, is just $p(x, t) = 0 \forall x \in \Omega$ and $0 < t < \ell/S$.

Now, imposing mass-conservation at d_2 we have:

$$Sh_1\theta_+ - h_1^3 \partial_x p_+ - Sh_2\theta_- + h_2^3 \partial_x p_- = 2S(h_1\theta_+ - h_2\theta_-),$$

so

$$\theta_- = \frac{h_1}{h_2} + \frac{h_1^3 \partial_x p_+ - h_2^3 \partial_x p_-}{Sh_2}, \quad \text{on } x = d_2. \quad (4.31)$$

For $0 \leq t < \ell/S$ we have $\partial_x p = 0$ everywhere, so the saturation θ on the very left of d_2 is given by

$$\theta_- = h_1/h_2. \quad (4.32)$$

As there is no pressure while the pocket is entering, by using (4.32) and the fully flooded condition we can solve the saturation θ by the *characteristics* method for the transport equation. This method is shown in Figure 4.13.

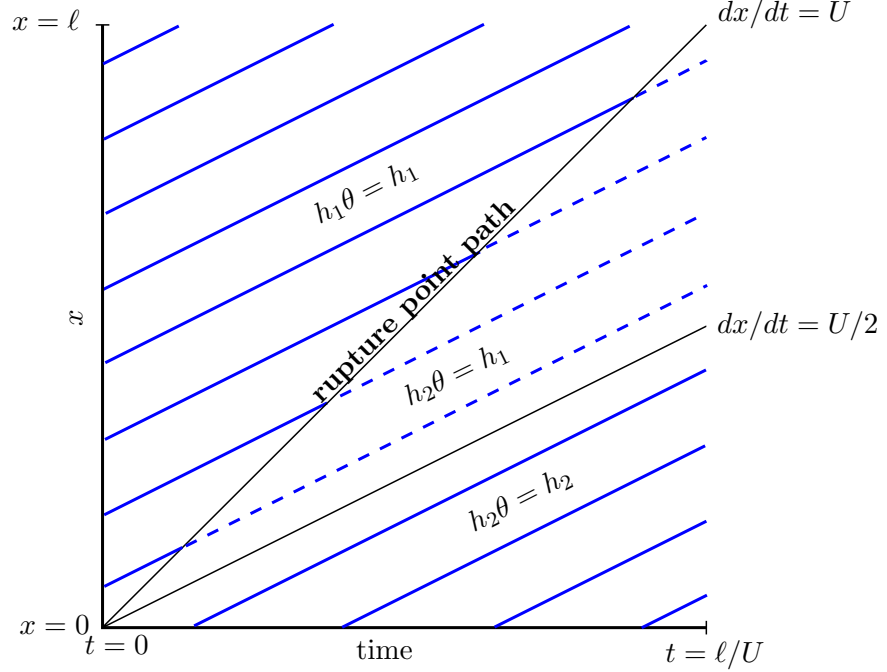


FIGURE 4.13: Characteristics lines of the transport equation of $h\theta$ for $0 < t < t_1$.

This way, we obtain the profiles of both fields p and θ at $t = \ell/S$, i.e., $p = 0$ on all Ω and

$$\theta(x, \ell/S) = \begin{cases} h_1/h_2 & \ell/2 \leq x \leq \ell, \\ 1 & \text{elsewhere.} \end{cases}$$

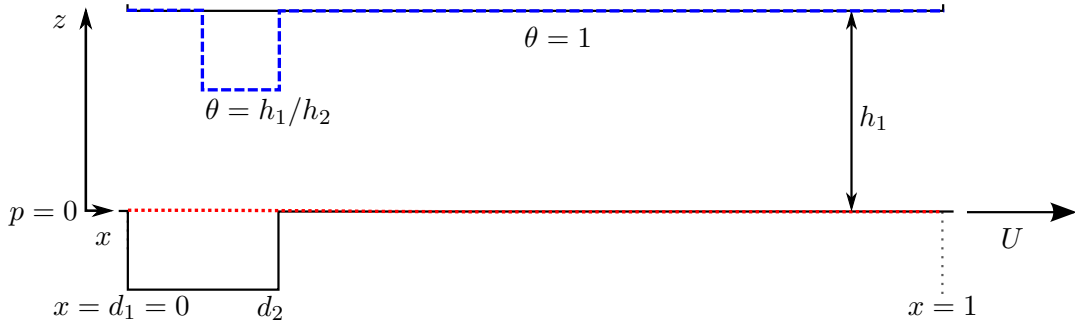


FIGURE 4.14: Values of p (lower pointed red line) and θ (upper dashed blue line) at $t = \ell/S$.

The state of p and θ at $t = \ell/S$ is shown in Figure 4.14. Initially we have no pressurized zone. Now, consider $\ell/S < t < 1$ and denote by $\beta(t)$ the right side of ω , we have

$\beta(t = \ell/S^+) = \ell/2$. We will show that, to find the behavior of p and θ after $t = \ell/S$, we need to know the behavior of $\beta(t)$.

Now, as $\beta(t)$ depends continuously on time, we already know the dependency of pressure with β . In fact, equations (4.22) and (4.23) are valid changing d_2 by β , so we have

$$\frac{\partial p}{\partial x} = \frac{C}{h^3} - \frac{S\Delta h}{h^3} H(x - d_1), \quad \text{on } \omega =]0, \beta[, \quad (4.33)$$

$$p(0) = p(\beta) = 0. \quad (4.34)$$

Similarly, changing ℓ by $\beta - d_1$, we have the equations

$$C = \frac{S(\beta - d_1) h_1^3 \Delta h}{d_1 h_2^3 + (\beta - d_1) h_1^3}, \quad (4.35)$$

and so

$$p(d_1) = \frac{S(\beta - d_1) d_1 \Delta h}{d_1 h_2^3 + (\beta - d_1) h_1^3}. \quad (4.36)$$

Now, we need to find the time evolution of β . For this, let us write equation (4.30) for β . Knowing that $\partial_x p_+(\beta) = 0$ and $\theta_-(\beta) = 1$ we get:

$$\frac{h_2^3}{2} \partial_x p_-(\beta) = h_2 (\theta_+(\beta) - 1) \left(\beta' - \frac{S}{2} \right), \quad (4.37)$$

being β' the velocity of β . As $\partial_x p_-(\beta) < 0$ and $\theta_+(\beta) < 1$, we get $\beta' > S/2$. By the characteristics method we get $\theta_+(\beta) = h_1/h_2$ (see Figure 4.15).

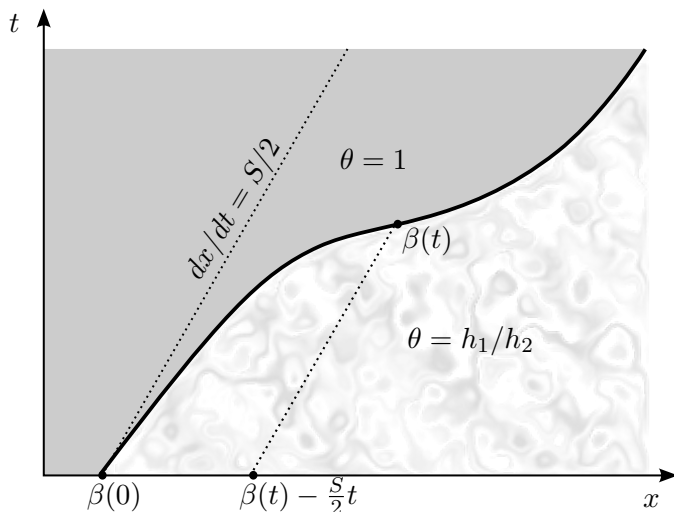


FIGURE 4.15: Characteristic lines to find $\theta_+(\beta)$.

Putting this on equation (4.37), we can write the relation

$$h_2^3 \partial_x p_-(\beta) = (S - 2\beta')\Delta h. \quad (4.38)$$

And from equations (4.33) and (4.35) we have that

$$h_2^3 \partial_x p_-(\beta) = \frac{S(\beta - d_1)h_1^3 \Delta h}{d_1 h_2^3 + (\beta - d_1)h_1^3} - S\Delta h.$$

Replacing this in equation (4.38) and rearranging terms we obtain that

$$\frac{d\beta}{dt} = \frac{S}{2} \left(1 + \frac{h_2^3}{h_2^3 + h_1^3(\beta/d_1 - 1)} \right). \quad (4.39)$$

Integrating this equation and using the initial condition $\beta(\ell/S) = \ell/2$ we can find the behavior of the cavitated zone (field θ) and thus the pressure field.

For $1 \leq t < 1 + \ell$ (while the pocket is exiting the domain), the solution we showed continues to be valid whenever $\beta < 1$. After β reaches the right side of the domain it must be replaced by 1 in equation (4.36).

Comparison of the solutions

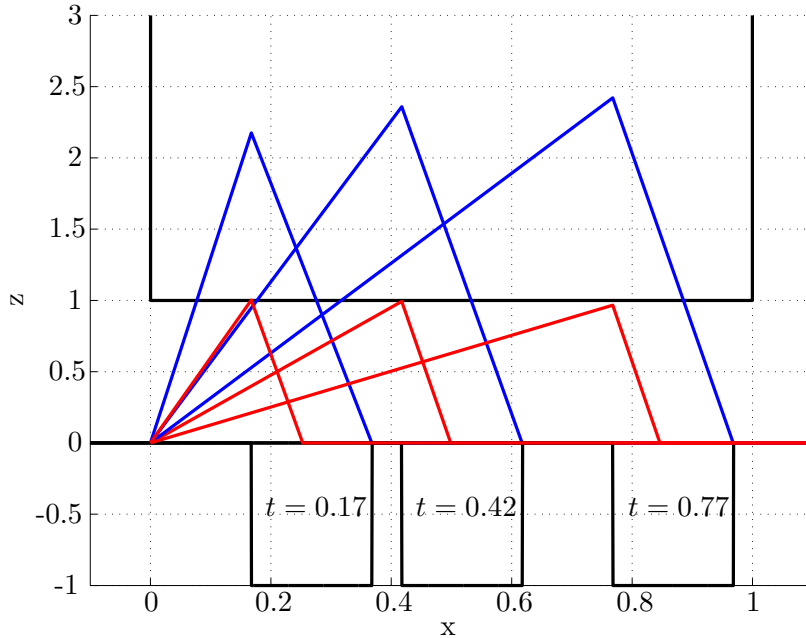


FIGURE 4.16: Analytic solutions of Elrod-Adams (in red) and Reynolds (in blue) cavitation models for three different times. The non-dimensional pressure profiles were amplified by a factor of 100.

Figure 4.16 shows the analytic solutions found for both models, in blue the solution for Reynolds model and in red the solution for Elrod-Adams model. The parameters chosen for this example were $\Delta h = 1$, $\ell = 0.2$ and $h_1 = 1$. Different moments are shown, $t = 0.17, 0.42, 0.77$. Notice that Reynolds model solution overestimate the peak on pressure approx. by a factor of 2. Also, the length of the cavitated zone for Elrod-Adams model is more than half of the pocket, while for the Reynolds model there is no cavitation at all.

Chapter 5

Numerical methods and illustrative examples

In Chapter 4 we have presented the models involved in lubrication theory. In this chapter we present how these models' calculations can be done in a computer. For this, we will use Finite Volume Methods that are known to give good numerical behavior for conservative laws. Due to the non-linear nature of the cavitation models, Gauss-Seidel like algorithms will be used. The details of the resulting resolution algorithms for each model are presented. Finally, we give a simple example of what can be done with these algorithms. This example consists in the resolution of the problem of the pocket presented in Section §4.5.2 but this time allowing for a dynamic behavior of the slider in the z -axis.

5.1 Finite volume discretization

Mass conservation is an important issue when considering cavitation modeling for Reynolds equation [5, 74]. Because of this, when seeking for a discrete version of the models we are dealing with, *Finite Volume Methods* are very helpful as they construct the discretization from the flux functions associated to the transported quantity. Also, these methods are useful when considering linear equations where the coefficients have discontinuous jumps, like in lubrication with discontinuous gap functions [61].

Finite Difference Methods are also classical methods to discretize an equation, however, these methods overview the nature of the model being discretized. Finite difference methods viewpoint is the approximation of the differential operators at each point of the discrete domain. On the other hand, Finite Volume Methods seek for a discrete

version of the flux function related to the transported quantity. Next, we present Finite Volume Methods by developing an example.

Take a domain $\Omega \subset \mathbb{R}^2$, a quantity $q : \Omega \times [0, +\infty[\rightarrow \mathbb{R}^2$ and $\vec{\mathbf{J}} : \Omega \rightarrow \mathbb{R}^2$, with all this, the next equation is called *conservation law* for q

$$\frac{\partial q}{\partial t} = -\nabla \cdot \vec{\mathbf{J}}, \quad \text{on } \Omega, \quad (5.1)$$

with *flux function* $\vec{\mathbf{J}} = \begin{pmatrix} J_x \\ J_y \end{pmatrix}$. Consider the simple domain $\Omega = [0, 1] \times [0, 1]$ and divide it into square volumes of uniform size with edges of length $\Delta\ell$. Also, let us discretize the time variable uniformly as $t_k = k\Delta t$. This way, integrating equation (5.1) over a *control volume* V (see Figure 5.1) and over the time interval $[t_{n-1}, t_n]$, and using the divergence theorem we obtain

$$\int_V q(\mathbf{x}, t_n) dv - \int_V q(\mathbf{x}, t_{n-1}) dv = - \int_{t_{n-1}}^{t_n} \int_{\partial V} \vec{\mathbf{J}} \cdot \hat{\boldsymbol{\eta}} dl dt, \quad (5.2)$$

where $\hat{\boldsymbol{\eta}}$ is the unitary normal vector pointing outwards V on its boundary ∂V . We divide ∂V in the northern $\partial V_{\hat{n}}$, southern $\partial V_{\hat{s}}$, eastern $\partial V_{\hat{e}}$ and western $\partial V_{\hat{w}}$ borders as is shown in Figure 5.1. Let us define the next average quantities

$$q_{ij}^n = \frac{1}{|V|} \int_V q(\mathbf{x}, t_n) dv, \quad J_\xi = \frac{1}{\Delta t} \int_{t_{n-1}}^{t_n} \left(\int_{\partial V_\xi} \vec{\mathbf{J}} \cdot \hat{\boldsymbol{\eta}} dl \right) dt,$$

where $\xi \in \{\hat{n}, \hat{s}, \hat{e}, \hat{w}\}$ and $|V|$ is the volume of V and it is equal to $(\Delta\ell)^2$. Then, equation (5.2) can be written as

$$q_{ij}^n = q_{ij}^{n-1} - \frac{\Delta t}{(\Delta\ell)^2} (J_{\hat{n}} - J_{\hat{s}} + J_{\hat{e}} - J_{\hat{w}}). \quad (5.3)$$

This equation is satisfied exactly by the solution of equation (5.1). If one could calculate the fluxes J_ξ in function of the unknowns q_{ij}^n , then the system would be closed along with suitable boundary conditions. However, in general, this is not the case and what we have are approximations of the real fluxes in function of the unknowns q_{ij}^n .

Let us denote some approximation of J_ξ by \tilde{J}_ξ . We can write a discrete version of equation (5.3) as

$$Q_{ij}^n = Q_{ij}^{n-1} - \frac{\Delta t}{(\Delta\ell)^2} (\tilde{J}_{\hat{n}} - \tilde{J}_{\hat{s}} + \tilde{J}_{\hat{e}} - \tilde{J}_{\hat{w}}). \quad (5.4)$$

Equation (5.4) is a general form for Finite Volume Methods in the case presented above. Different methods arise when different formulas \tilde{J}_ξ are chosen, which in general, will depend of the quantities Q_{ij}^n (see Section 4.1 in [61]).

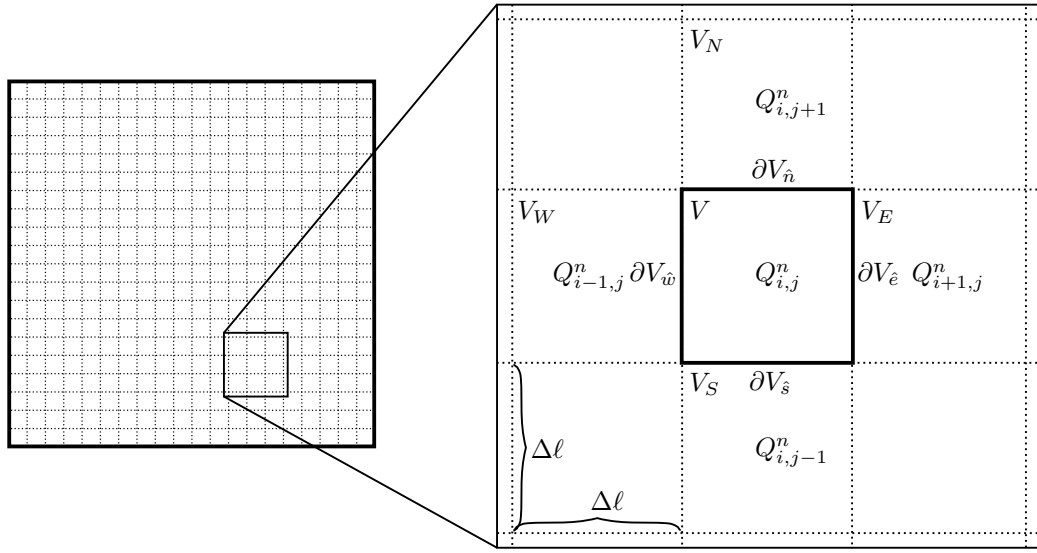


FIGURE 5.1: Staggered grid for Finite Volume Methods.

5.2 Numerical implementation of Reynolds equation and cavitation models

In this section we solve numerically Reynolds equation by using the classical Gauss-Seidel method. After this, we adequate this procedure for taking into account Reynolds cavitation model by a projection of the partial solution into the cone of positive functions on $H_0^1(\Omega)$. Finally, we present a version of the algorithm for the Elrod-Adams model. Through all this section we suppose the behavior of the gap function h to be known in space and time. In Section §5.3 we include a dynamic coupling between the upper surface motion and the generated hydrodynamic pressure by means of the Newton equation.

5.2.1 Reynolds equation without cavitation

A Finite Volume Method is going to be used for a one dimensional problem (the generalization to two dimensions does not represent major difficulties) on the domain $\Omega = [0, 1]$. The discretization obtained this way is going to be base for the discretization when taking into account some cavitation model.

First, let us set the problem of finding some function p that satisfies Reynolds equation

$$\frac{\partial h}{\partial t} = -\frac{\partial}{\partial x} \left(\frac{S}{2} h - \frac{h^3}{2} \frac{\partial p}{\partial x} \right), \quad (5.5)$$

which is written in the conservative form of equation (5.1). In this case, our conserved quantity is h and the flux function corresponds to

$$J_x = \frac{S}{2}h - \frac{h^3}{2} \frac{\partial p}{\partial x}.$$

Let us select the $N+1$ equally spaced points from $[0, 1]$ $\{x_i\}_{i=0}^N$ given by $x_i = \Delta x (i + \frac{1}{2})$, with $\Delta x = 1/N$. Each x_i is the center of the volume $V_i = [x_i - \Delta x/2, x_i + \Delta x/2]$. Time is discretized with a constant time step Δt , starting from $t_0 = 0$ and $t_n = n\Delta t$. This way, the Finite Volume equation (5.3) fulfilled by p at each volume V_i can be written (see Figure 5.2)

$$h_i^n = h_i^{n-1} - \frac{\Delta t}{\Delta x} \left(J_x \left(x_{i+\frac{1}{2}}, t_n \right) - J_x \left(x_{i-\frac{1}{2}}, t_n \right) \right), \quad (5.6)$$

where $x_{i+1/2} = x_i + \Delta x/2$, and the volume of each V_i is $|V_i| = \Delta x$.

Now, for each x_i and time t_n , we associate an unknown average pressure P_i^n and a known gap value $h_i^n = h(x_i, t_n)$.

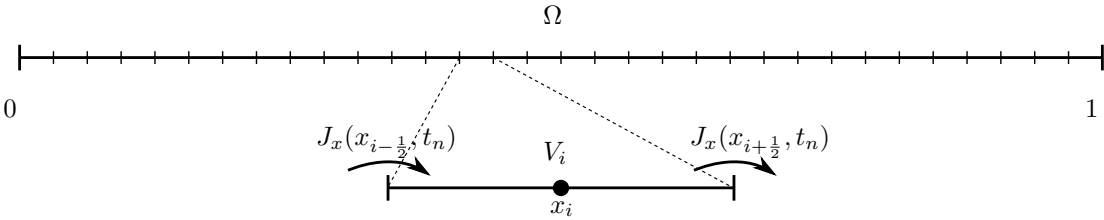


FIGURE 5.2: Scheme of flux functions 1D.

The flux function evaluated at the interface between the volumes V_{i-1} at time t_n is written

$$J_x \left(x_{i-\frac{1}{2}}, t_n \right) = \frac{1}{2} \left\{ S h \left(x_{i-\frac{1}{2}}, t_n \right) - h \left(x_{i-\frac{1}{2}}, t_n \right)^3 \partial_x p \left(x_{i-\frac{1}{2}}, t_n \right) \right\}.$$

Now, let us approximate $h(x_{i-1/2}, t_n)^3$ by $a_{i-1/2} = \frac{(h_{i-1}^n)^3 + (h_i^n)^3}{2}$ and denote as P_i^n our approximation of pressure for each unknown exact value p_i^n . Then, using an *upwind Finite Difference scheme* for the first term (convective term) and a *centralized Finite Difference scheme* for the second term (diffusive term) we obtain the next approximation for the fluxes $J_x(x_{i-1/2}, t_n)$

$$\tilde{J}_x \left(x_{i-\frac{1}{2}}, t_n \right) = \frac{1}{2} \left\{ S h_{i-1}^n - a_{i-\frac{1}{2}} \frac{P_i^n - P_{i-1}^n}{\Delta x} \right\}. \quad (5.7)$$

The kind of Finite Difference schemes we have chosen are known to give time stability when considering these type of equations (see Chapter 4 in [61]).

Putting the approximations (5.7) in equation (5.6) and rearranging terms we get the system of equations:

$$-a_{i-\frac{1}{2}} P_{i-1}^n + \left(a_{i-\frac{1}{2}} + a_{i+\frac{1}{2}} \right) P_i^n - a_{i+\frac{1}{2}} P_{i+1}^n = -\frac{2\Delta x^2}{\Delta t} (h_i^n - h_i^{n-1}) - S\Delta x (h_i^n - h_{i-1}^n), \quad (5.8)$$

for $i = 1 \dots N-1$. This system of equations is closed when including suitable boundary conditions. Here we take

$$P_0^n = 0 \text{ and } P_N^n = 0 \quad \forall n \geq 0. \quad (5.9)$$

Convergence of the numerical scheme

Let us write the system of equations (5.8) as

$$\frac{-a_{i-\frac{1}{2}} P_{i-1}^n + \left(a_{i-\frac{1}{2}} + a_{i+\frac{1}{2}} \right) P_i^n - a_{i+\frac{1}{2}} P_{i+1}^n}{\Delta x^2} = -2 \frac{h_i^n - h_i^{n-1}}{\Delta t} - S \frac{h_i^n - h_{i-1}^n}{\Delta x}. \quad (5.10)$$

This system corresponds to a Finite Differences scheme for equation (5.5), its left-hand side is an approximation of the operator $\partial_x(h^3 \partial_x)$ applied to p and its right-hand side approximates $2\partial_t + S\partial_x$ applied to h . Here, we suppose the discrete values h_i^n as being known. With all this, the questions are: once we have solved the system (5.10), how much good are the approximation P_i^n ? What is its behavior when we augment the number of volumes?

Given some fixed time t_n , we denote as $\hat{\mathbf{p}}_N$ the vector of components $(\hat{\mathbf{p}}_N)_i = P_i^n$ (omitting the dependency on time), where N is the number of volumes we are taking into account. Also, denote as \mathbf{p}_N the vector of components $(\mathbf{p}_N)_i = p(x_i, t_n)$, i.e., the values of the exact solution. With this, we write the system of equations (5.10) as

$$\mathbf{A}_N \hat{\mathbf{p}}_N = \hat{\mathbf{f}}_N. \quad (5.11)$$

Where \mathbf{A}_N is the next tridiagonal symmetric matrix

$$\mathbf{A}_N = N^2 \begin{pmatrix} d_1 & -a_{3/2} & & & \\ -a_{3/2} & d_2 & -a_{5/2} & & \\ & -a_{5/2} & \ddots & \ddots & \\ & & \ddots & \ddots & -a_{N-3/2} \\ & & & -a_{N-3/2} & d_{N-1} \end{pmatrix}, \quad \text{with } d_i = a_{i-\frac{1}{2}} + a_{i+\frac{1}{2}}. \quad (5.12)$$

and $\hat{\mathbf{f}}_N = -\frac{2}{\Delta t} \mathbf{I}_N (\mathbf{h}_N^n - \mathbf{h}_N^{n-1}) - \frac{S}{\Delta x} \mathbf{C}_N \mathbf{h}_N^n$ corresponds to¹ the right-hand side of the system (5.10), \mathbf{I}_N is the identity matrix of order $N - 1$, and \mathbf{C}_N is the matrix such that

$$\begin{cases} (\mathbf{C}_N)_{i,j} = 1 & \text{if } j = i, \\ (\mathbf{C}_N)_{i,j} = -1 & \text{if } j = i - 1, \\ 0 & \text{otherwise.} \end{cases}$$

Denoting as \mathbf{f}_N the vector of components

$$(\mathbf{f}_N)_i = -2 \partial_t h(x_i, t_n) - S \partial_x h(x_i, t_n), \quad i \in \{1 \dots N - 1\}, \quad (5.13)$$

we have that $\hat{\mathbf{f}}_N$ is an approximation of \mathbf{f}_N .

We define the quantities

$$\boldsymbol{\tau}_N^A = \mathbf{A}_N \mathbf{p}_N - \mathbf{f}_N, \quad \text{and} \quad \boldsymbol{\tau}_N^f = \hat{\mathbf{f}}_N - \mathbf{f}_N. \quad (5.14)$$

$\boldsymbol{\tau}_N^A$ is the *local truncation error* due to the fact that \mathbf{A}_N is an approximation of the functional relation between \mathbf{p}_N and \mathbf{f}_N . $\boldsymbol{\tau}_N^f$ is the local truncation error due to the fact that $\hat{\mathbf{f}}_N$ is an approximation of \mathbf{f}_N . We define also the *global error* $\mathbf{E}_N = \hat{\mathbf{p}}_N - \mathbf{p}_N$, which represents the punctual differences between our approximation and the real values of p . Putting all these definitions in equation (5.11) we get

$$\mathbf{A}_N \mathbf{E}_N = \boldsymbol{\tau}_N^f - \boldsymbol{\tau}_N^A.$$

And so, if \mathbf{A}_N is non-singular we have

$$\|\mathbf{E}_N\| \leq \|\mathbf{A}_N^{-1}\| \left(\|\boldsymbol{\tau}_N^f\| + \|\boldsymbol{\tau}_N^A\| \right).$$

Using terms found in literature [62], we say that the numerical approximation of the differential formulation (5.5) given by the system (5.11) is *consistent* if both

$$\|\boldsymbol{\tau}_N^A\|, \|\boldsymbol{\tau}_N^f\| \rightarrow 0 \quad \text{as } N \rightarrow \infty.$$

We say the same numerical scheme is *stable* if $\|\mathbf{A}_N^{-1}\|$ remains bounded as $N \rightarrow \infty$, i.e., $\exists C \in \mathbb{R}, M \in \mathbb{N}$ such that $\|\mathbf{A}_N^{-1}\| \leq C \ \forall N > M$. Therefore, if our numerical approximation is consistent and stable, then $\hat{\mathbf{p}}_N \rightarrow \mathbf{p}_N$ as $N \rightarrow \infty$.

¹If the boundary conditions are not null, they could be added in the first and last components of this vector.

From now on, if \mathbf{v} is a vector of values over a uniform grid of m points with distance Δx between those points, we use the *grid norm* (see [62]) given by²

$$\|\mathbf{v}\|_2 = \left(\Delta x \sum_{i=1}^m |v_i|^2 \right)^{\frac{1}{2}}.$$

Proposition 5.1. *System (5.11) is consistent.*

Proof. Using Taylor's Series, it is easy to find that $(\boldsymbol{\tau}_N^f)_i = \mathcal{O}(\Delta x)(h''(x_i))$. Thus, supposing the sum of the $h''(x_i)^2$ is bounded, we obtain that

$$\|\boldsymbol{\tau}_N^f\|_2 = \mathcal{O}(\Delta x). \quad (5.15)$$

For proving $\|\boldsymbol{\tau}_N^A\| \rightarrow 0$ as $N \rightarrow \infty$, again by Taylor's series we have

$$\begin{aligned} \frac{-a_{i-\frac{1}{2}} p_{i-1}^n + (a_{i-\frac{1}{2}} + a_{i+\frac{1}{2}}) p_i^n - a_{i+\frac{1}{2}} p_{i+1}^n}{\Delta x^2} &= -\frac{a_{i+\frac{1}{2}} p'_{i+\frac{1}{2}} - a_{i-\frac{1}{2}} p'_{i-\frac{1}{2}}}{\Delta x} + \mathcal{O}(\Delta x^2) (a_i p_i''')' \\ &= -(a_i p_i')' + \mathcal{O}(\Delta x^2) ((a_i p_i''')' + (a_i p_i'''))'. \end{aligned} \quad (5.16)$$

However, a_i is not the exact value of h^3 at the point x_i but an approximation. In fact, by Taylor's series

$$a_i = \frac{(h_{i-\frac{1}{2}}^n)^3 + (h_{i+\frac{1}{2}}^n)^3}{2} = h(x_i, t_n)^3 + \mathcal{O}(\Delta x^2) \partial_{xx} (h(x_i, t_n)^3).$$

Putting this in the right side of equation (5.16) we get

$$\frac{-a_{i-\frac{1}{2}} p_{i-1}^n + (a_{i-\frac{1}{2}} + a_{i+\frac{1}{2}}) p_i^n - a_{i+\frac{1}{2}} p_{i+1}^n}{\Delta x^2} = -\partial_x (h(x_i, t_n)^3 \partial_x p(x_i, t_n)) + \mathcal{O}(\Delta x^2) C_i,$$

where $C_i = ((h_i^3)''' p_i')' + (a_i p_i''')' + (a_i p_i'')''$. This way, we have proved that

$$(\boldsymbol{\tau}_N^A)_i = \mathcal{O}(\Delta x^2) ((h_i^3)''' p_i')' + (a_i p_i''')' + (a_i p_i'')''. \quad (5.17)$$

Therefore, supposing the sum of the C_i^2 is bounded, we have $\|\boldsymbol{\tau}_N^A\| \rightarrow 0$ as $N \rightarrow \infty$. \square

Stability is a property not easy to prove for the general definition of \mathbf{A}_N . The case corresponding to h constant is studied in Chapter 2 of [62]. In that case we can write $\mathbf{A}_N = -N^2 h^3 \tilde{\mathbf{A}}$, where $\tilde{\mathbf{A}}$ is the tridiagonal matrix with diagonal elements equal to

²As this norm is just a constant times the euclidean norm, the corresponding induced norm on matrices also accomplishes the basic properties of Euclidean induced norms, e.g., $\|\mathbf{A} \mathbf{v}\| \leq \|\mathbf{A}\| \|\mathbf{v}\|$.

-2 and the rest of non-null elements equal to 1 . In the referenced work, and for that particular case, it is proved that the Euclidean induced matrix norm (2-norm) can be used for proving stability. This because the eigenvalues of $\tilde{\mathbf{A}}$ are known. In fact, it is proved that $\|\mathbf{A}_N^{-1}\|_2 = h^3\pi^2 + \mathcal{O}(\Delta x^2)$. Thus, the system is stable and the numerical scheme converges. Addressing the eigenvalues of the general matrix \mathbf{A}_N we have the next result.

Proposition 5.2. *The matrix \mathbf{A}_N defined in equation (5.12) is positive definite.*

Proof. Let $\mathbf{v} \in \mathbb{R}^N \setminus \{\vec{0}\}$ be a vector of components $\{v_i\}_{i=1}^N$ and, to simplify notation, let us take $v_0 = v_{N+1} = 0$, then we have

$$\begin{aligned}\mathbf{v}^\top \mathbf{A} \mathbf{v} &= \sum_{i=1}^N \left(v_i a_{i-\frac{1}{2}} (v_i - v_{i-1}) + v_i a_{i+\frac{1}{2}} (v_i - v_{i+1}) \right) \\ &= \sum_{i=1}^N \left(a_{i-\frac{1}{2}} v_i^2 - a_{i-\frac{1}{2}} v_i v_{i-1} + a_{i+\frac{1}{2}} v_i^2 - a_{i+\frac{1}{2}} v_i v_{i+1} \right) \\ &= \sum_{i=1}^N \left(a_{i-\frac{1}{2}} v_i^2 - 2 a_{i-\frac{1}{2}} v_i v_{i-1} + a_{i+\frac{1}{2}} v_i^2 \right) \\ &= \sum_{i=1}^N \left(a_{i-\frac{1}{2}} (v_i - v_{i-1})^2 - a_{i-\frac{1}{2}} v_{i-1}^2 + a_{i+\frac{1}{2}} v_i^2 \right) \\ &= a_{-\frac{1}{2}} v_1^2 + a_{N+\frac{1}{2}} v_N^2 + \sum_{i=1}^N a_{i-\frac{1}{2}} (v_i - v_{i-1})^2 > 0\end{aligned}$$

□

As far as we know, there is no general expression for the eigenvalues of \mathbf{A}_N , and there is not analytic estimate of $\|\mathbf{A}_N^{-1}\|$ for any other induced matrix norm.

Numerical example

Here we solve numerically the problem of the Disc wedge presented in Section §2.5.2. The numerical solution is compared with the analytic one and a convergence test is performed.

Figure 5.3 shows the numerical and the analytic solution. This was made along the non-dimensionalization given in Table 2.3, with $R = 80$, $S = 1$, $h_0 = 1$, $L = 1 \times 10^{-3}$ [m] and $H = 1 \times 10^{-6}$ [m].

In Table 5.1 we resume the truncation error and global error for different number of volumes, $N = 2^6, 2^7, 2^8, 2^9$. Please notice that both quantities $\|\boldsymbol{\tau}_N^f\|_2$ and $\|E_N\|_2$

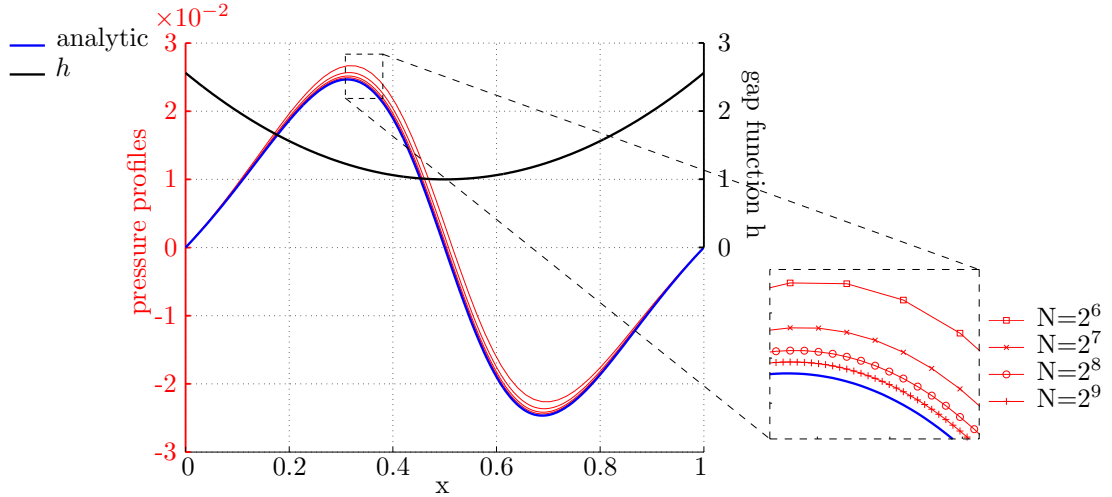


FIGURE 5.3: Convergence of the numerical solution for the Disc wedge presented in Section §2.5.2.

N	Δx	$\ \boldsymbol{\tau}_N^A\ _2$	$\ \boldsymbol{\tau}_N^f\ _2$	$\ \mathbf{A}_N^{-1}\ _2$	$\ E_N\ _2$
2^6	1.56×10^{-2}	5.71×10^{-3}	9.69×10^{-2}	5.15×10^{-6}	1.92×10^{-3}
2^7	7.81×10^{-3}	1.44×10^{-3}	4.86×10^{-2}	1.13×10^{-6}	9.61×10^{-4}
2^8	3.91×10^{-3}	3.62×10^{-4}	2.44×10^{-2}	2.60×10^{-7}	4.81×10^{-4}
2^9	1.95×10^{-3}	9.07×10^{-5}	1.22×10^{-2}	6.18×10^{-8}	2.40×10^{-4}

TABLE 5.1: Convergence of the truncation errors and global error for the numerical example of the Disc wedge.

are in linear relation with Δx ($\propto \Delta x$), while $\|\boldsymbol{\tau}_N^A\|_2$ is in quadratic relation with Δx ($\propto \Delta x^2$). These results agree with equations (5.15) and (5.17).

Gauss-Seidel iterations

We will present the Gauss-Seidel iterative method for the system of equations (5.8) and (5.9). Gauss-Seidel is a classical iterative method for solving linear and non-linear systems of equations [49, 5, 72]. First, we write

$$-a_{i-\frac{1}{2}}^n P_{i-1}^n + \left(a_{i-\frac{1}{2}}^n + a_{i+\frac{1}{2}}^n \right) P_i^n - a_{i+\frac{1}{2}}^n P_{i+1}^n = f_i^n, \quad (5.18)$$

where $f_i^n = -\frac{2\Delta x^2}{\Delta t} (h_i^n - h_i^{n-1}) - S\Delta x (h_i^n - h_{i-1}^n)$. We resume this procedure in Algorithm 1.

Please notice that Gauss-Seidel uses the already calculated value $P_{i-1}^{n,k}$ for calculating the new value $P_i^{n,k}$. If, instead of using $P_{i-1}^{n,k}$, we use the older value $P_{i-1}^{n,k-1}$ the iterative procedure is known as the *Jacobi iterative method*, which is known to have a lower convergence speed when compared to Gauss-Seidel [49].

Algorithm 1: Gauss-Seidel for Reynolds equation

Input: h^n : gap function, P^{n-1} : initial guess, tol : for stop criterion

Output: P^n pressure at time n

```

begin
     $k = 0$ 
     $P^{n,k} = P^{n-1}$ 
    while  $change > tol$  do
         $k = k + 1$ 
        for  $i = 1 \dots N$  do
             $P_i^{n,k} = \frac{1}{a_{i-\frac{1}{2}}^n + a_{i+\frac{1}{2}}^n} (f_i^n + a_{i-\frac{1}{2}}^n P_{i-1}^{n,k} + a_{i+\frac{1}{2}}^n P_{i+1}^{n,k-1})$ 
        end for
         $change = \|P^{n,k} - P^{n,k-1}\|_\infty$ 
    end while
    return  $P^{n,k}$ 
end

```

5.2.2 Reynolds model

Remembering what was exposed in Chapter 4, Reynolds cavitation model consists in finding a weak solution of Reynolds equation not in the whole space $H_0^1(\Omega)$ but in the cone of positive functions $K \subset H_0^1(\Omega)$ given by

$$K = \{\phi \in H_0^1(\Omega) : \phi \geq 0 \text{ a.e. on } \Omega\},$$

which leads to the variational inequality (4.5).

The method we will use for solving Reynolds model was first exposed by Christopherson in 1941 [25]. A detailed study of that method, applied to Journal Bearings, can be found in [32]. This iterative methods can be described as: given an iterative method for solving Reynolds equation (e.g., a Gauss-Seidel like method), at the end of each iteration the partial solution is projected into the cone K . Such projection consists in nullifying each component of $P^{n,k}$ that is negative (see Section 2.8 in [48]). Therefore, the Algorithm 1 for solving Reynolds equation only needs a little modification that is presented in Algorithm 2.

The convergence study of this procedure is based in the contraction property of the operator involved in each iteration composed with the projection operator into K , the interested reader may review [19, 48]. In these last works, it is proved that Algorithm 2 converges to the solution of the next discrete problem (remember \mathbf{A}_N is positive definite according to Proposition 5.2)

$$\min_{v \in \mathbb{R}_+^N} \frac{1}{2} v^\top \mathbf{A}_N v - (\hat{\mathbf{f}}_N)^\top v,$$

where $\mathbb{R}_+^N = \{x \in \mathbb{R}^N : x_i \geq 0, i = 1 \dots N\}$, \mathbf{A}_N and $\hat{\mathbf{f}}_N$ are given by equations (5.12) and (5.13). In fact, Herbin and Marchand [55] showed that a discretization by Finite Volume Methods converges to the solution of the associated variational inequality for the obstacle problem [54]. Thus, we have good evidence of the convergence of Algorithm 2, although we are not going to prove it.

Algorithm 2: Gauss-Seidel for Reynolds equation with Reynolds cavitation model

Input: h^n : gap function, P^{n-1} : initial guess, tol : for stop criterion

Output: P^n pressure at time n

begin

$k = 0$

$P^{n,k} = P^{n-1}$

while $change > tol$ **do**

$k = k + 1$

for $i = 1 \dots N$ **do**

$$\left| \begin{array}{l} P_i^{n,k} = \frac{1}{a_{i-1}^n + a_i^n} \left(f_i^n + a_{i-1}^n P_{i-1}^{n,k} + a_i^n P_{i+1}^{n,k-1} \right) \\ P_i^{n,k} = \max(0, P_i^{n,k}) \end{array} \right.$$

end for

$change = \|P^{n,k} - P^{n,k-1}\|_\infty$

end while

return $P^{n,k}$

end

with $a_i^n = (h_{i+1/2}^n)^3$ and $f_i^n = -\frac{2\Delta x^2}{\Delta t} (h_i^n - h_i^{n-1}) - S\Delta x (h_i^n - h_{i-1}^n)$.

A linear obstacle

As another instance of Gauss-Seidel iterations with projections of the partial solution, we refer to Figure 4.3. There, $u(x)$ was generated solving the Poisson equation $\nabla^2 u = C$ (where $C < 0$ is some constant source term) by Gauss-Seidel iterations and restricting the partial solution u^k by the assignation $u^k = \min(\psi, u^k)$, with ψ being the linear function that describes the obstacle.

5.2.3 Elrod-Adams model

In Chapter 4 we presented the modified Reynolds equation when considering Elrod-Adams cavitation model. In the 1D case we write this equation along the complementary

conditions as

$$\frac{\partial h\theta}{\partial t} = -\frac{\partial}{\partial x} \left(\frac{S}{2} h\theta - \frac{h^3}{2} \frac{\partial p}{\partial x} \right), \quad (5.19)$$

$$p(1-\theta) = 0, \quad (5.20)$$

both in Ω . Notice not only the pressure field p is unknown but also the saturation field θ . Making a similar discretization as before, we discretize θ as $\theta_i^n = \theta(x_i, t_n)$. This way, the transported quantity over each volume V_i is written $Q_i^n = h_i^n \theta_i^n$, which corresponds to the average amount of fluid present at each volume. This way, for Elrod-Adams cavitation model, the equation analogous to equation (5.8) is

$$-\gamma(Q_i^n - Q_i^{n-1} - \nu(Q_i^n - Q_{i-1}^n)) = -a_{i-1}^n P_{i-1}^n + (a_{i-1}^n + a_i^n) P_i^n - a_i^n P_{i+1}^n, \quad (5.21)$$

where $a_i = (h_{i+1/2}^n)^3$, $\gamma = \frac{2\Delta x^2}{\Delta t}$ and $\nu = (S/2)\Delta t/\Delta x$ is the Courant number. Calculating first the pressures P_i^n by equation (5.21), we obtain the following equations for P_i^n and θ_i^n for iteration k

$$P_i^{n,k} = \frac{1}{a_{i-1}^n + a_i^n} \left(-\gamma(Q_i^{n,k-1} - Q_i^{n-1} - \nu(Q_i^{n,k-1} - Q_{i-1}^{n,k-1})) + a_{i-1}^n P_{i-1}^{n,k} + a_i^n P_{i+1}^{n,k-1} \right) \quad (5.22)$$

$$\theta_i^{n,k} = \frac{1}{\gamma(1+\nu)} \left(\gamma(Q_i^{n-1} + \nu Q_{i-1}^{n,k}) + a_{i-1}^n P_{i-1}^{n,k} - (a_{i-1}^n + a_i^n) P_i^{n,k} + a_i^n P_{i+1}^{n,k-1} \right). \quad (5.23)$$

The Gauss-Seidel like algorithm for Reynolds equation when considering cavitation through Elrod-Adams model is shown in Algorithm 3. Notice the complementary equation (5.20) is used to project the partial solutions (p^k, θ^k) into the subset of functions such that, for every volume V_i , if $p > 0$ we must have $\theta = 1$, and if $0 < \theta < 1$ we must have $p = 0$.

5.3 Numerical solution examples

Gauss-Seidel is known to have a good numerical stability behavior for large systems of equations [49]. On the other hand, it is also known for having too low convergence speed, which means that the computational cost may be too high. To deal with this issue, we used methods like *over-relaxation* and *multigrid techniques*, which are well known for accelerating convergence speed [43], also see [20].

Algorithm 3: Gauss-Seidel for Reynolds equation with Elrod-Adams cavitation model

Input: h^n : gap function, (P^{n-1}, θ^{n-1}) : initial guess, tol : for stop criterion

Output: P^n, θ^n pressure and saturation fields at time n resp.

begin

```

    k = 0
    Pn,k = Pn-1, θn,k = θn-1
    while change > tol do
        k = k + 1
        for i = 1 ... N do
            if Pin,k-1 > 0 or θin,k-1 == 1 then
                Compute Pin,k using equation (5.22)
                if Pin,k ≥ 0 then
                    | θkn,k = 1
                else
                    | Pin,k = 0
                end if
            end if
            if Pin,k ≤ 0 or θin,k < 1 then
                Compute θin,k using equation (5.23)
                if θin,k < 1 then
                    | Pin,k = 0
                else
                    | θin,k = 1
                end if
            end if
        end for
        change = ||Pn,k - Pn,k-1||∞ + ||θn,k - θn,k-1||∞
    end while
    return (Pn,k, θn,k)
end

```

5.3.1 Numerical solution to the analytic examples

In this section we show the numerical solutions of the problems exposed in Section §4.5.

Cavitation in Pure Squeeze Motion

Here we search numerically for the analytic solution found for the Pure Squeeze Problem in Section §4.5.1. For this, we used a coarse mesh of only 100 volumes and a finer mesh of 450 volumes (same mesh used in [5]). The parameter tol of Algorithm 3 was chosen to be $tol = 5 \times 10^{-6}$ and the time step was set as $\Delta t = 0.3 \times \Delta x$ (as the numeric scheme is implicit in time, there is unconditional time-stability [62], so this parameter is chosen just for having a good resolution in time), where $\Delta x = 1/100, 1/450$.

Remembering $\Sigma(t)$ denotes the right side of the cavitated zone, from Figure 5.4 we observe a convergent behavior of the numerical solutions to the analytic solution of

Elrod-Adams model. Similar behavior is found for the numerical solutions of $\Sigma(t)$ when considering the Reynolds model in Figure 5.5.

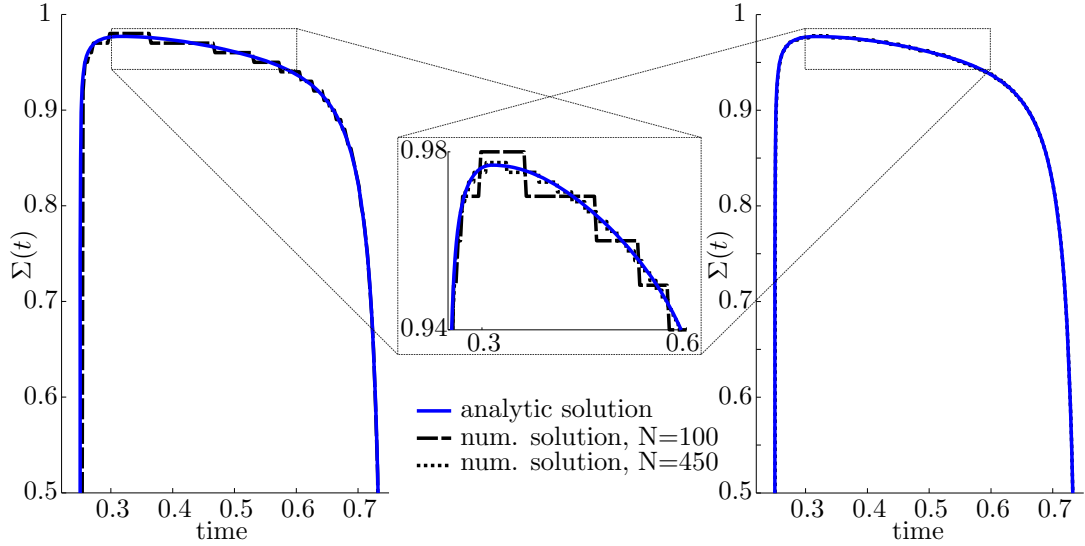


FIGURE 5.4: Numerical solution of $\Sigma(t)$ for Elrod-Adams model with $N = 100, 450$.

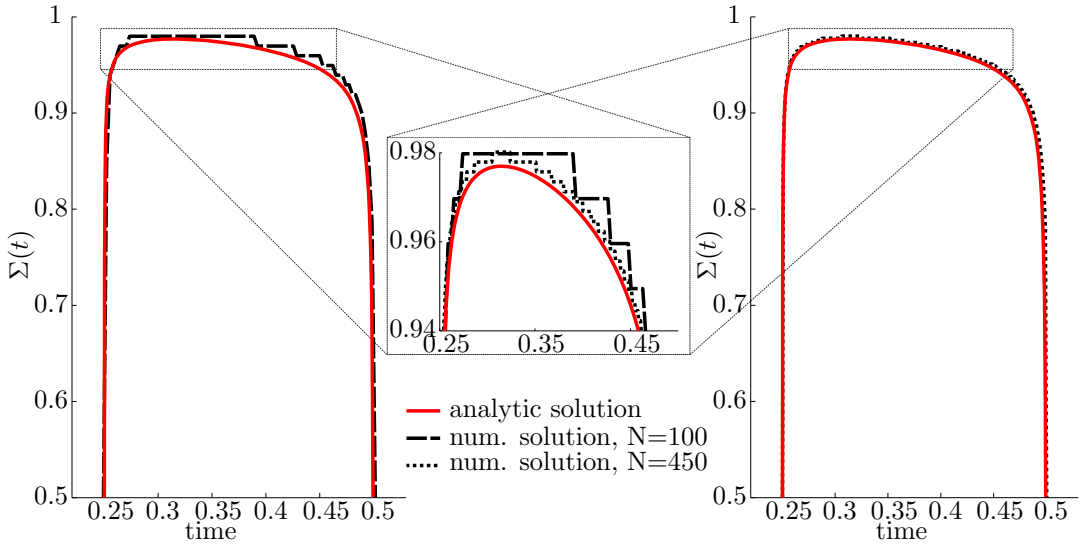


FIGURE 5.5: Numerical solution of $\Sigma(t)$ for Reynolds model with $N = 100, 450$.

Also, remember we denote as t_{ref} the time for which $\Sigma(t)$ change from being a rupture point to be a reformation point $t_{ref} \approx 0.3146$. In Figure 5.6 a good agreement between the numerical solution of θ for $t = 0.3146$ and the analytic solution can be observed. This agreement is important since, as we said in Section §4.5.1, it influences the behavior of the cavitated zone during the time interval for which $\Sigma(t)$ is a reformation point (see equation (4.15)).

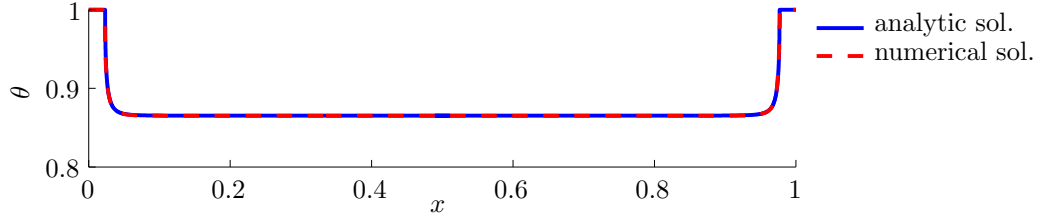


FIGURE 5.6: Numerical ($N=450$) and analytic solution of the saturation θ for $t = 0.3146$, just before the reformation time t_{ref} .

Cavitation in a flat pad with a traveling pocket

In Section §4.5.2 we showed the analytic solutions of the pressure p and saturation field θ for the stepped shape pocket traveling through the domain.

Let us take a number of volumes equal to $N = 1024$ over $]0, 1[$, a time step $\Delta t = 2 \Delta x / S$ (Courant number equal to 1) and $tol = 1 \times 10^{-7}$. With this, by using Algorithm 3 we reproduce in Figure 5.7 the analytic results found before in Figure 4.16. Moreover,

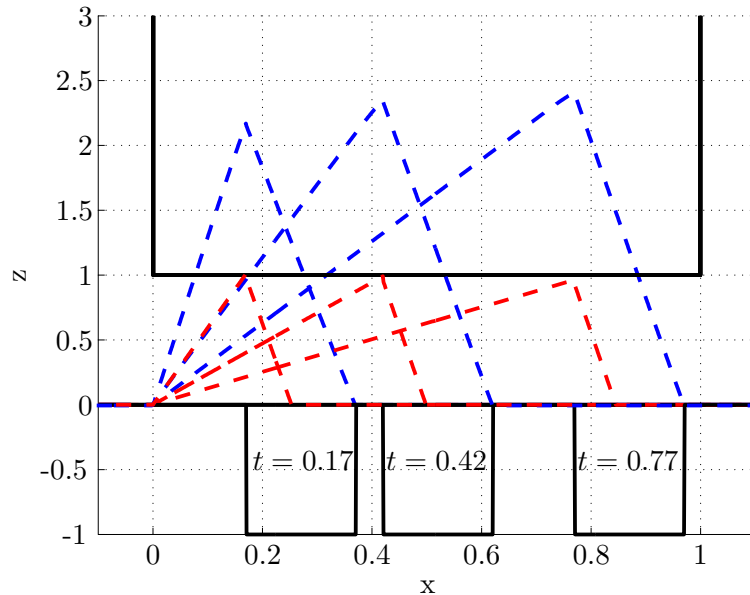


FIGURE 5.7: Analytic solutions of Elrod-Adams (in red) and Reynolds (in blue) cavitation models for three different times as done in Section §4.5.2. The non-dimensional pressure profiles were amplified by a factor of 100.

a convergence analysis is performed comparing the numerical and analytic solutions for $t = 0.77$. The differences between pressures is denoted e_p and between the field saturation is denoted by e_θ . The norms of these errors are shown in Figure 5.8. From those data, it is observed that $\|e_p\|_{H_0^1(0,1)}$ decays as $\|e_p\|_{H_0^1(0,1)} \propto \Delta x^{1.9}$ (quadratic convergence rate), while $\|e_\theta\|_{L^2(0,1)} \propto \Delta x^{\frac{1}{2}}$ (under linear convergence rate). Please note the rate convergence for pressure remains as calculated in Proposition 5.1. The low rate convergence for θ should be associated to its discontinuities in $]0, 1[$.

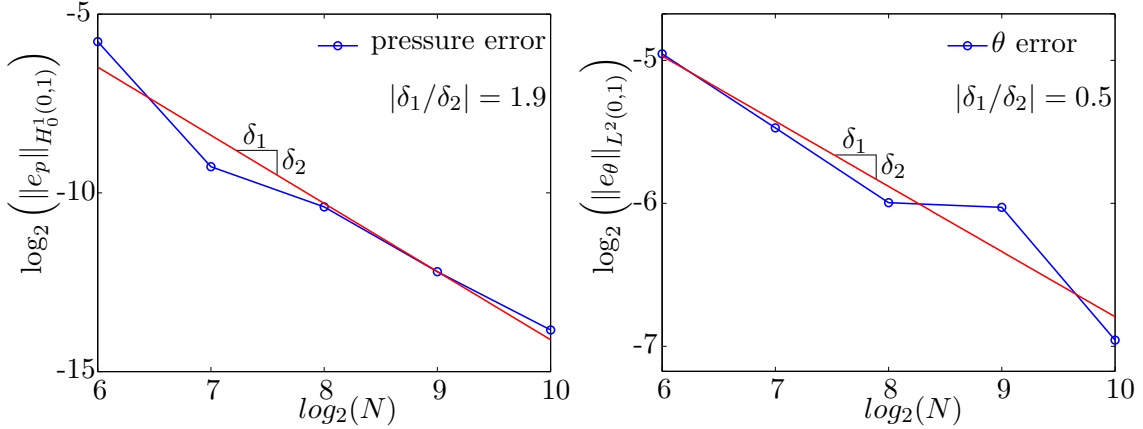


FIGURE 5.8: Convergence analysis for p and θ in the $H_0^1(0, 1)$ and $L^2(0, 1)$ norms resp. for the traveling pocket problem solved in Section §4.5.2.

5.3.2 Incorporating dynamics

Until now we have always considered the gap function h as a known data. From now on, we will consider h as an unknown, and its behavior will be coupled to the hydrodynamic pressure p . For this, we revisit the problem of the traveling pocket, this time allowing the upper surface (slider) to be depending on time $h_U(t) = Z(t)$.

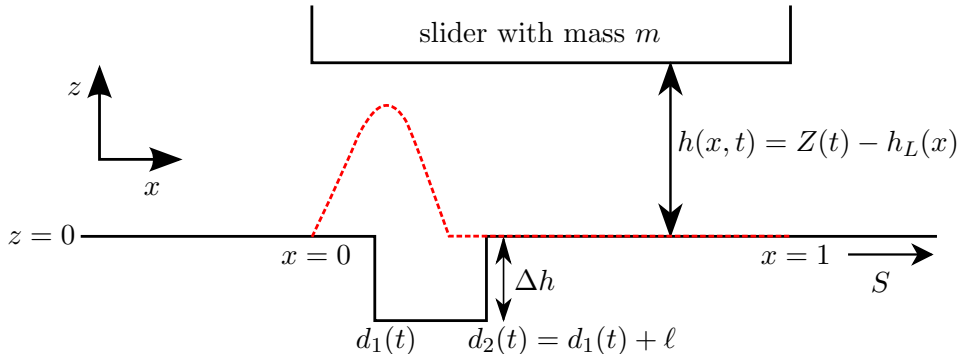


FIGURE 5.9: Scheme of the traveling pocket with a dynamic dependence of the upper surface.

We assume the slider has a non-dimensional inertial mass m . Also, let us denote as $Z(t)$ the distance between the slider and the lower surface (see Figure 5.9). Then, $Z(t)$ is a result of the interaction between the applied load W^a (negative in the z -axis), which is supposed to be constant, and the hydrodynamic force $W^h(t)$ given by

$$W^h(t) = \int_0^1 p(x, t) dx. \quad (5.24)$$

This way, the evolution of $Z(t)$ can be modeled by solving the problem

$$m Z''(t) = W^h(t) - W^a, \quad (5.25)$$

$$Z'(t = 0) = V_0, \quad (5.26)$$

$$Z(t = 0) = Z_0. \quad (5.27)$$

Where $Z' = U$ is the slider vertical velocity and Z'' its acceleration. We discretize time by some constant time step Δt with $t_n = n\Delta t$, and for any function $f(t)$ we denote $f^n = f(t_n)$. And we discretize the Newton Equation (5.25) in time by using the next Newmark scheme for integration (which is unconditionally stable on time, e.g., [45] Section 7.2)

$$Z^n = Z^{n-1} + \Delta t U^{n-1} + \frac{\Delta t^2}{2} \frac{W^{h,n} - W_a}{m}, \quad (5.28)$$

$$U^n = U^{n-1} + \Delta t \frac{W^{h,n} - W_a}{m}. \quad (5.29)$$

Observe that $\frac{W^{h,n} - W_a}{m}$ is the acceleration at time t_n . This numerical integration is implicit in time, so the iterative procedure will include an update of the partial solution $Z^{n,k}$ of Z^n at each step. The Gauss-Seidel like algorithm resulting from including dynamics through this Newmark scheme is described in Algorithm 4, at the end of this section. A convergence result of it can be found in a recent work made by Buscaglia and Talibi [17].

A simple example simulation

We will present a simulation done to exemplify the incorporation of dynamics in the lubrication problem of the traveling pocket.

The scales used in this section are described in Table 5.2. The values of the basic scales are $U = 10[\text{m/s}]$, $H = 10^{-6}[\text{m}]$ and $L = 10^{-3}[\text{m}]$. The non-dimensional mass corresponds to 2×10^{-5} and the non-dimensional applied load was $W^a = 1.666 \times 10^{-4}$. The length of the pocket is $\ell = 0.2$ and its depth $d = 1$. The number of volumes was chosen to be $N = 512$ over $]0, 1[$ and the time step $\Delta t = 2\Delta x/S$ (Courant number equal to 1).

The initial conditions for the slider position are $Z(t = 0) = 1$ and $Z'(t = 0) = 0$. And at $t = 0$ the pocket is just entering into the domain, i.e., the right side of the pocket is at $x = 0$.

In Figure 5.10 we show the numerical solutions of p and θ obtained for different time instants t_i , $i = 1 \dots 7$. In blue, we plot the mass quantity $h\theta$ present at each point of the domain. In red, we present the non-dimensional pressure amplified 200 times.

Quantity	Scale	Name
x	L	Horizontal coordinate
S	U	Relative velocity
t	$\frac{L}{U}$	Time
h	H	Gap thickness
Z, d	H	Slider vertical position, texture depth
p	$\frac{6\mu UL}{H^2}$	Pressure
W^a, W^h	$\frac{6\mu UL^2}{H^2}$	Applied and hydrodynamic forces
m	$\frac{6L^4\mu}{H^3U}$	Slider mass

TABLE 5.2: Basic and derived scales.

Let us remember that d_1 denotes the position of the left side of the pocket while d_2 denotes its right side. It can be observed that at time $t_1 = 0.19$ a cavitated zone is present at the very left of d_2 due to the divergent geometry of the pocket. There, the value of θ is approximated 1/2 as predicted by equation (4.32). This *cavitation bubble* travels along the domain coupled to the divergent zone of the pocket and being expanded since the transport velocity ($S/2$) is minor than the pocket velocity S . Also, we can observe a small pressure profile due to the slow downward movement of the slider ($Z' < 0$).

At $t_2 = 0.29$ the convergent part of the pocket generates a pressurized region that produces a small lifting of the slider ($Z \approx 1.05$), this also causes the appearance of a cavitated zone all along the interval $]d_2, 1[$.

The upward movement of the slider between $t_2 = 0.29$ and $t_3 = 0.59$, which corresponds to a positive squeeze, produces the pressure profile to diminish and a cavitated zone appears at the left side of the pressurized zone. Moreover, at $t_4 = 0.68$ we observe cavitation happening at almost the entire domain.

This lack of hydrodynamic support makes the slider to fall again as there is no force to compensate the negative applied load. In fact, $Z(t_4) = 1.54$ while $Z(t_5) = 1.44$. Because of this fall, the slider makes contact again with the fluid and new pressurized zones appear due to a negative squeeze contribution. Interestingly, the slider does not fall enough as to make contact with the fluid at the convergent zone of the pocket, and so the pocket does not give any hydrodynamic support after approximately $t_4 = 0.68$. The last two frames, allow us to observe the cavitated zones traveling to the left and a slow downward movement of the slider that produces a small pressure profile.

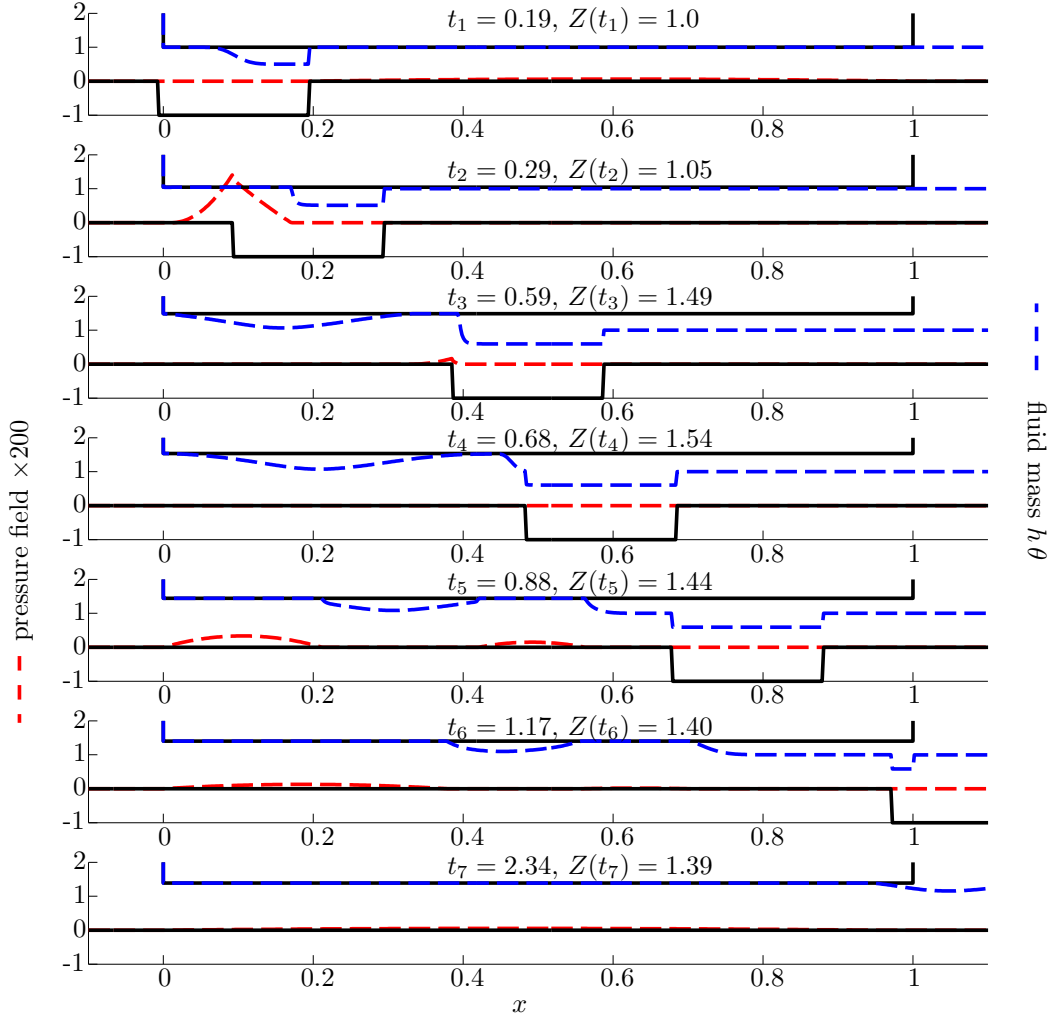


FIGURE 5.10: Scheme of the traveling pocket with a dynamic dependence of the upper surface.

Remark 5.3. It is difficult, maybe not possible, to generate analytic solutions for the simulation we have just shown. In Chapter 6 we will perform even more complicated simulations where the textures will have a sinusoidal profile.

Remark 5.4. To perform such simulations we require suitable computational techniques that allow us to accelerate the convergence speed of the algorithms presented. Multigrid and Parallel Computing Techniques are example of this and the interested reader may review [20] and [23].

Algorithm 4: Dynamic Gauss-Seidel for Reynolds equation with Elrod-Adams cavitation model

Input: h^n : gap function, (P^0, θ^0) : initial guess, tol : for stop criterion, m : slider mass, W^a : applied load, Z^0, V^0 : initial position and vertical velocity of the slider resp.: NT : number of time steps to simulate

Output: P, θ, Z, V pressure, saturation, slider position and slider velocities in time

begin

```

for  $n = 1 \dots NT$  do
     $k = 0$ 
     $P^{n,k} = P^{n-1}, \theta^{n,k} = \theta^{n-1}$ 
    while  $change > tol$  do
         $k = k + 1$ 
         $W^{n,k-1} = \Delta x \sum_{i=1}^N p_i$ 
         $Z^{n,k} = Z^{n-1} + \Delta t V^{n-1} + \frac{\Delta t^2}{2m} (W^{n,k-1} - W^a)$ 
         $h_i^{n,k} = Z^{n,k} - h_L(x_i)$ 
        for  $i = 1 \dots N$  do
            if  $P_i^{n,k-1} > 0$  or  $\theta_i^{n,k-1} == 1$  then
                Compute  $P_i^{n,k}$  using equation (5.22)
                if  $P_i^{n,k} \geq 0$  then
                     $\theta_k^{n,k} = 1$ 
                else
                     $P_i^{n,k} = 0$ 
                end if
            end if
            if  $P_i^{n,k} \leq 0$  or  $\theta_i^{n,k} < 1$  then
                Compute  $\theta_i^{n,k}$  using equation (5.23)
                if  $\theta_i^{n,k} < 1$  then
                     $P_i^{n,k} = 0$ 
                else
                     $\theta_i^{n,k} = 1$ 
                end if
            end if
        end for
         $change = \|P^{n,k} - P^{n,k-1}\|_\infty + \|\theta^{n,k} - \theta^{n,k-1}\|_\infty + \|Z^{n,k} - Z^{n,k-1}\|_\infty$ 
    end while
     $Z^n = Z^{n,k}$ 
     $V^n = V^{n-1} + \frac{\Delta t}{m} (W^{n,k-1} - W^a)$ 
    for  $i = 1 \dots N$  do
         $p_i^n = p_i^{n,k}$ 
         $\theta_i^n = \theta_i^{n,k}$ 
    end for
end for
return  $(P, \theta, Z, V)$ 
end

```

Chapter 6

Application: a study of sinusoidal textured slider bearings

6.1 Introduction

During the last decade several studies have been done addressing the possibility of improving the tribological behavior of hydrodynamic bearings with the use of surface texturing technologies. Experimental and theoretical studies have shown reduction of friction by the introduction of textured surfaces, e.g., [33, 44, 39, 21], but the mechanisms behind this improvements are not yet well understood.

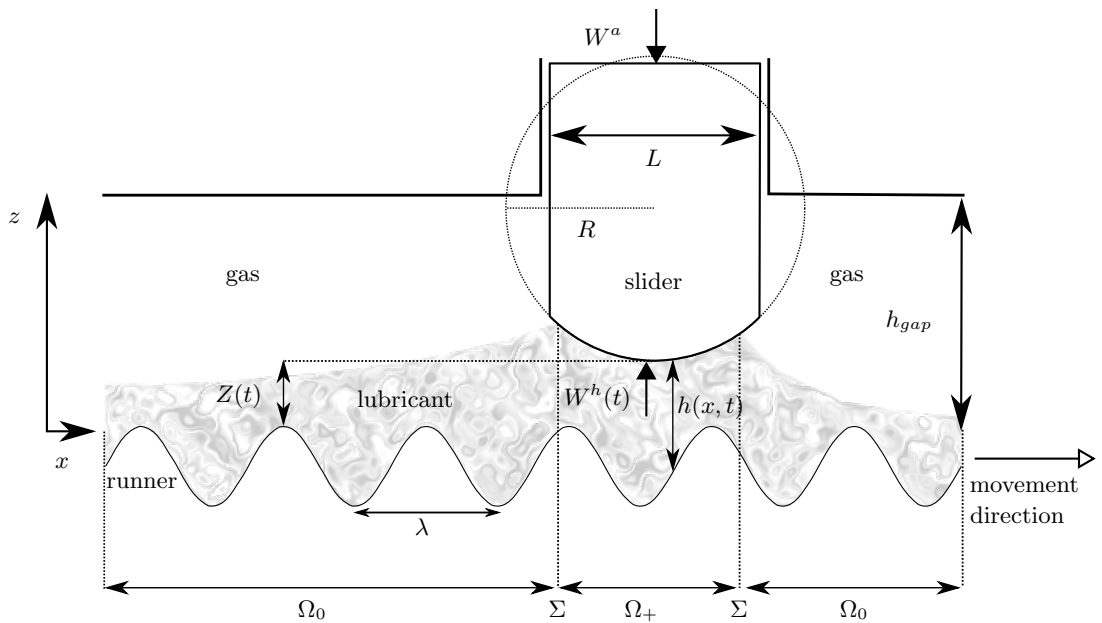


FIGURE 6.1: Slider bearing over and a sinusoidal textured runner scheme.

In [16], by using Homogenization Technique, it is shown that if cavitation is not taken into account, the introduction of textures only augment friction and diminishes the minimal distance between surfaces (so-called *minimum clearance*). This means that for having an improvement of the tribological behavior either, the perturbation of the surface must be outside the validity of the Homogenization Theory employed (an example of this is the Rayleigh step shown in Section §2.5), or other physical phenomenon such as cavitation must be considered.

Recalling Figure 1.4, the degree of conformity between the bearing and the liner, for the slider bearing (Figure 6.1), is computed by R/L . Making use of Reynolds model, Gadeschi et al. [44], and later Checo et al. [21] employing Elrod-Adams model, showed that for a fixed load it is possible to obtain a configuration that minimizes the friction only for moderate R/L (≈ 10) or higher. These results are in agreement with pioneering experiments made by Costa & Hutchins [31], and with latter studies by Tomanik [85, 86], Kovalchenko et al [60], Yin et al [90], Scaraggi et al [81], among others [33, 2, 50].

In this chapter we show that making use of the theory presented in the previous chapters, and keeping the characteristics of the slider bearing as simple as we can, we are able to perform interesting simulations whose results can reveal part of the nature of friction reduction mechanisms. Thus, focusing in simple hypotheses, we choose to *texturize* the runner with a sinusoidal shape of periodicity λ and depth d , as in Figure 6.1. Also, we assume the profile of the slider to have a circular shape of curvature radius R .

In the next section we setup the simulations details and establish the range chosen for the parameters λ , d , R/L , applied load W^a and mass m of the slider.

6.2 Simulation details and untextured cases

The values chosen for the different basic scales were: runner velocity $U = 10[\text{m/s}]$, slider length $L = 10^{-3}[\text{m}]$, $H = 1\mu[\text{m}]$ (1 micron), fluid viscosity $\mu = 4 \times 10^{-3}[\text{Pa}\cdot\text{s}]$ and for the mass of the slider $m = 0.048[\text{kg/m}]$ per unit width. Those values are typical for compression rings of car engines [22, 44]. We also chose the applied load as being $W_a = 40[\text{N/m}]$ per unit length, this value was selected as to assure Hydrodynamic Lubrication conditions. The non-dimensionalization used are showed in Table 6.1.

For sake of clarity, we summarize the mathematical problem to be solved during the simulations as:

Quantity	Scale	Name
x, λ	L	Horizontal coordinate, texture period
S	U	Relative velocity
R	L	Slider curvature radius
t	$\frac{L}{U}$	Time
h	H	Gap thickness
Z, d	H	Slider vertical position, texture depth
p	$\frac{6\mu UL}{H^2}$	Pressure
W^a, W^h	$\frac{6\mu UL^2}{H^2}$	Applied and hydrodynamic forces
F	$\frac{\mu UL}{H}$	Friction force per unit width
m	$\frac{6L^4\mu}{H^3U}$	Slider mass

TABLE 6.1: Basic and derived scales for the dynamic slider with sinusoidal textures.

Find the trajectory of the slider $Z(t)$, and fields pressure $p(t)$ and saturation $\theta(t)$, defined on $\Omega = [0, 1]$, satisfying

$$\frac{\partial}{\partial x} \left(h^3 \frac{\partial p}{\partial x} \right) = S \frac{\partial h\theta}{\partial x} + 2 \frac{\partial h\theta}{\partial t}, \quad (6.1)$$

$$m \frac{d^2 Z}{dt^2} = W^h(t) - W^a, \quad (6.2)$$

along with the initial, boundary and complementary conditions

$$\begin{cases} Z(t=0) = Z_0, Z'(t=0) = V_0, \\ p = 0, & \text{in } \partial\Omega, \\ \theta = 1, & \text{in } x = 0, \\ p \geq 0, 0 < \theta \leq 1, & \text{in } \Omega, \\ p(1-\theta) = 0, & \text{in } \Omega, \end{cases} \quad (6.3)$$

where

$$W^h(t) = \int_0^1 p(x, t) dx, \quad (6.4)$$

$$h(x, t) = Z(t) + h_U(x) - h_L(x - St), \quad (6.5)$$

$$h_L(x) = -\frac{d}{2} (1 - \cos(2\pi x/\lambda)), \quad h_U(x) = \frac{L}{H} \left(R - \sqrt{R^2 - (x - 0.5)^2} \right). \quad (6.6)$$

and Z_0, V_0 are the initial position and velocity of the slider resp. assumed to be known. In fact, through all this Chapter we will take $V_0 = 0$ and $Z_0 = 4$.

The non-dimensional friction force per unit width is computed as (see equation (2.26)):

$$F(t) = \int_0^1 \left(6p \frac{\partial h_L}{\partial x} - 3h \frac{\partial p}{\partial x} - \frac{\mu S}{h} g(\theta) \right) dx, \quad (6.7)$$

where g is taken as

$$g(\theta) = \begin{cases} \theta, & \text{if } \theta > \theta_s \\ 0, & \text{otherwise.} \end{cases} \quad (6.8)$$

This parameter θ_s is a threshold for the onset of friction, it can be interpreted as the minimum lubricant fraction for shear forces to be transmitted from one surface to the other. Here, we set $\theta_s = 0.95$, in [21] it is observed that when choosing another value for θ_s the behavior of the contact is not altered significantly.

Notice that the boundary condition $\theta(0, t) = 1$ implies that the fluid film is always complete at the entrance of the domain. This implies the fully-flooded condition (see Section §1.2.5) and it guarantees, along with the applied-load chosen low enough, that we will work in the Hydrodynamic Lubrication Regime.

As we consider the hydrodynamic regime, there is no necessity of including some model for *contact pressure*, which only appears when considering mixed regimes of lubrication or similar. The interested reader may review [86] where the Greenwood-Williamson [51] model for contact pressure is used.

6.2.1 Quantities of interest

The simulations were done in such a way that a stationary state is reached at some time T , after that time, the variables acquire a periodic behavior on time, that periodicity has length λ equal to the textures period. With this, we denote the time interval where the measures are going to be done as $\mathcal{T} = [T, T + \lambda]$.

This way, from the non-dimensional friction coefficient (see Section §2.5.1)

$$f(t) = \frac{H}{6L} \frac{F(t)}{W^a}, \quad (6.9)$$

which varies through time, we define the average friction coefficient as

$$\bar{f} = \frac{1}{\lambda} \int_{\mathcal{T}} f(t) dt, \quad (6.10)$$

which characterizes the power lost due to friction. Observe the factor $\frac{H}{6L}$ appears since F and W^a are measured with different scales (see Table 6.1).

We also define the *minimum clearance*

$$C_{\min} = \min_{x \in \Omega, t \in \mathcal{T}} h(x, t), \quad (6.11)$$

which can be used to characterize surfaces wear in tribological systems.

6.2.2 Untextured cases

The first simulations we run are in absence of texture ($d = 0$). This way, varying R (which is equal to R/L since we fix the length of the slider to $L = 1$) as $R = 2^n$, $n = 2 \dots 10$, we obtain basis measures of \bar{f} and C_{\min} that will be compared later with the textured cases.

As an example, for $R = 32$, $Z_0 = 4$ and $V_0 = 0$, we show in Figure 6.2 the evolution of $Z(t)$, the friction coefficient $f(t)$ and $W^h(t)/W^a$. It can be observed that $W^h(t)$ starts being 8 times greater than the applied load so the slider tends first to rise, after that, $W^h(t)$ remains being a bit small than W^a . In fact, $W^h(t)$ converges to W^a while the slider decelerate and tend to the equilibrium position $Z(t > T) = 7.408$. On the other hand, the friction coefficient has no abrupt change while converging to $\bar{f} = 9.56 \times 10^{-2}$.

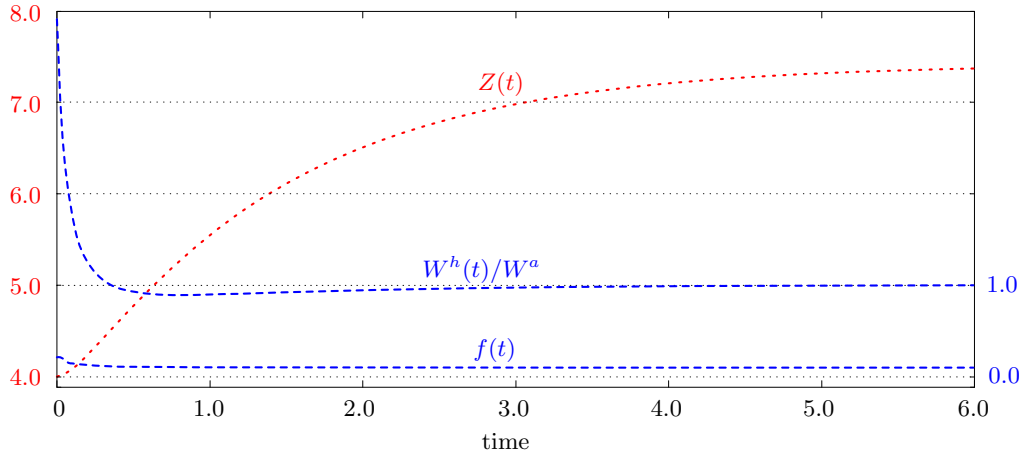


FIGURE 6.2: Slider evolution for the untextured case for load W^a and $R = 32$.

R	4	8	16	32	64	128	256	512	1024
C_{\min}	6.36	7.81	8.02	7.41	6.36	5.23	4.33	3.70	3.32
$\bar{f} \times 10^2$	7.61	7.45	8.12	9.56	11.9	15.4	20.3	26.1	28.7

TABLE 6.2: Friction coefficient \bar{f} and clearance C_{\min} for several values of R once they reached the stationary state.

Making the simulations for the values of R selected above, we obtain the reference values showed in Table 6.2 for C_{\min} and \bar{f} (amplified by a factor of 100). We remark that there seems to be an optimal value for R in the sense that the maximum value of C_{\min} is reached at $R = 16$, this is congruent with the existence of a shape of the liner that maximizes the load-carrying capacity, as it was shown in Section §2.5.1 for the Rayleigh step wedge. It is also in line with a similar analysis made in Section 5.7 of [18] for pad bearings.

6.3 Textures effects

Here we select values of λ around 1, more precisely $\lambda \in \{0.1 + k\Delta\lambda, k = 0 \dots 47\}$, $\Delta\lambda = 0.04$, with maximum value 1.98. For the depth $d \in \{k\Delta d, k = 1 \dots 51\}$, $\Delta d = 0.2$, with maximum value 10.2.

It is convenient to define the relative difference V_f between the friction coefficients for the untextured and textured cases, which reads

$$V_f(d, \lambda) = \frac{\bar{f}(d, \lambda) - f_{\text{untextured}}}{f_{\text{untextured}}}.$$

Analogously, the relative difference V_C of the minimal clearance is defined as

$$V_C(d, \lambda) = \frac{C_{\min}(d, \lambda) - C_{\min, \text{untextured}}}{C_{\min, \text{untextured}}}.$$

We select a moderate-conforming radius $R=32$ and a highly-conforming radius $R=256$.

The associated results for both curvatures are shown in Figure 6.3.

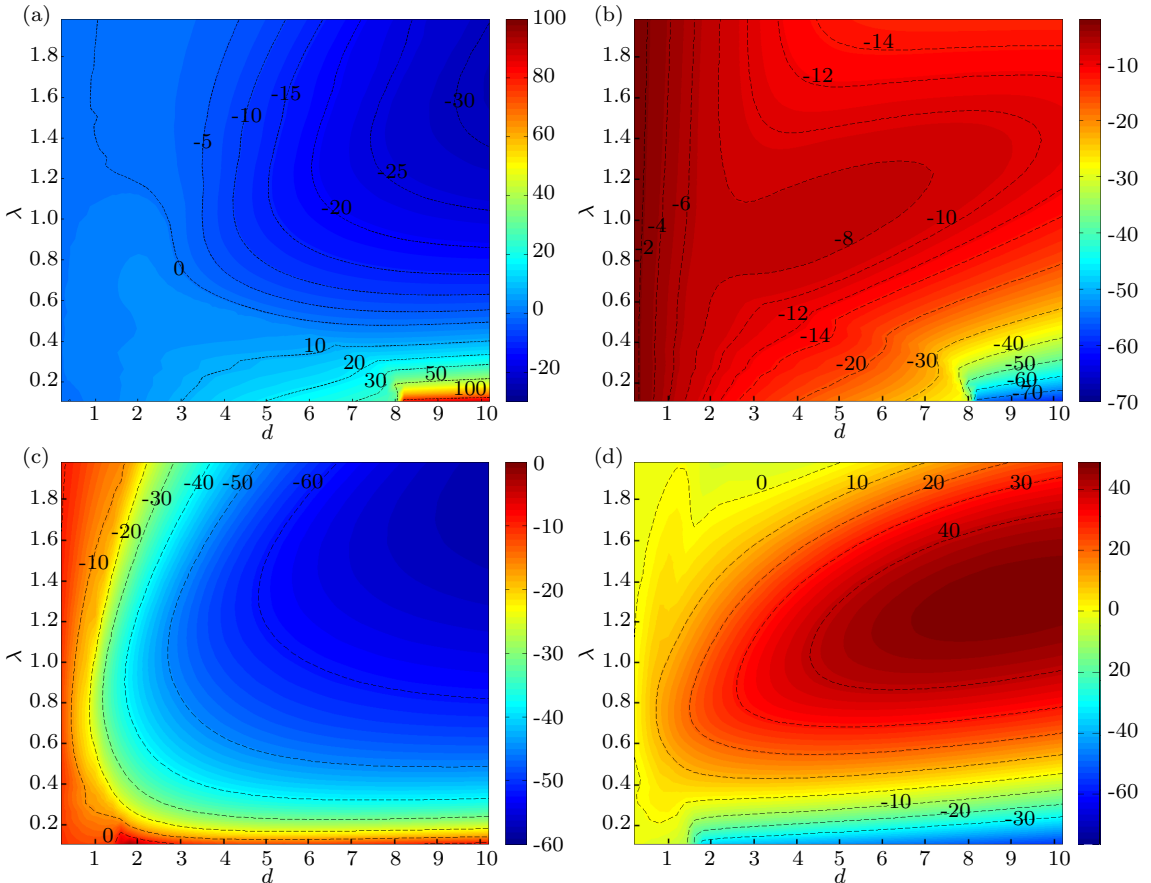


FIGURE 6.3: Comparison of C_{\min} and \bar{f} for several values of λ and d by relative differences V_f (left side) and V_C (right side) for $R=32, 256$ (upper and lower figures resp.).

6.3.1 General observations

As it can be observed, for the two curvatures selected there exist configurations of the textures that diminish friction and there are other configurations that augment it. The same can be observed for the minimum clearance. A smooth behavior of these quantities is observed. Also, when d tends to zero both $C_{\min}(d, \lambda)$ and $\bar{f}(d, \lambda)$ tend to the respective values of the untextured case. In fact, additional simulations have shown that, for a fixed depth d , both V_C and V_f tend to zero as the period λ grows.

As mentioned in this chapter's introduction, these results are in line with the existing literature. In fact, the bigger R/L , the bigger the set of textures that allows an improvement in friction and minimum clearance is. These results were recently published in [22], where a more extensive analysis can be found.

6.3.2 An effect of the traveling bubbles

Although both V_C and V_f have a smooth dependence on the parameters, a discontinuous behavior can be observed for small values of λ and $d \approx 8$ in both Figure 6.3(a) and Figure 6.3(b). To understand what happens there, we need to observe closer the behavior of p and θ when the periodic state has been reached.

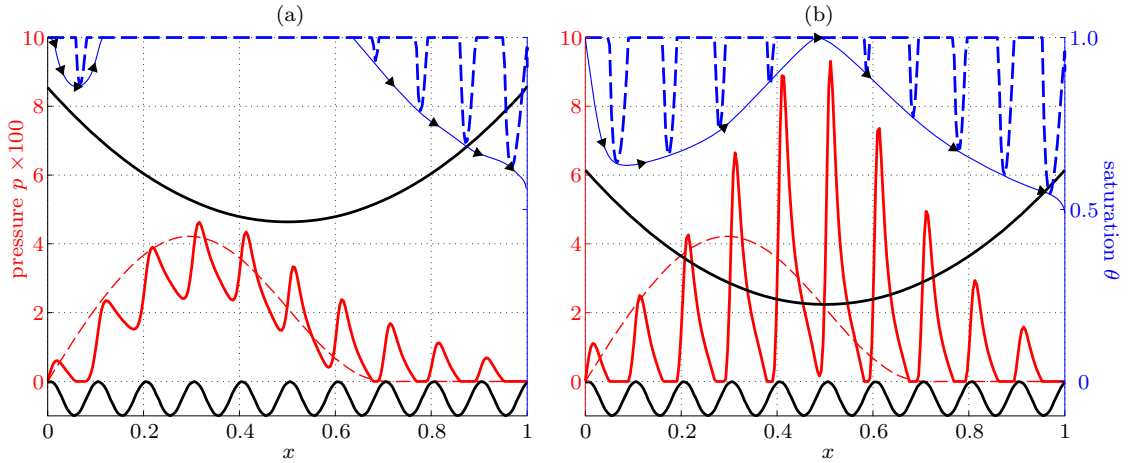


FIGURE 6.4: Sudden change of p and θ with a small change of d ($d = 8.1$ on the left and $d = 8.2$ on the right). Both with fixed curvature $R = 32$ and an arbitrary time $t > T$. The red line is the pressure field amplified 100 times, the red dashed line corresponds to the pressure of the untextured case. The blue continuous line corresponds to the path the minimum value of θ makes when *traveling* along the domain.

We fix the value of the periodicity as $\lambda = 0.1$ and select some arbitrary time $t > T$. The resulting fields p and θ are shown in Figure 6.4(a) for $d = 8.1$ and in Figure 6.4(b) for $d = 8.12$. In both figures the blue continuous lines (with arrows) represent the path the minimum value of θ (which depends on x) follows in time. Let us analyze both cases.

For $d = 8.1$, it is observed the presence of *cavitation bubbles* in two very separated areas. In the very left of the domain, a bubble grows and collapses almost immediately, while a second bubble appears around $x = 0.65$ and instead of collapsing it is transported outside the domain. As a consequence, the convergent region of the slider affects importantly the buildup of pressure. In fact, the pressure profile area is similar to the one generated in the untextured case (represented by the continuous red line), to which is summed up the effects of each convergent region of the “sinusoidal pockets”.

For $d = 8.2$, we observe the bubbles generated in the left side of the domain travel all along collapsing near $x = 0.5$, immediately after this collapse, a new bubble appears and travels outside the domain. This presence of cavitation on most part of the domain affects the pressure buildup. Thus, this time the convergence of the slider has less influence in the pressure profile, it only modulates the peak of the pressurized zones generated by the convergent parts of each sinusoidal pocket. This affects the load-carrying capacity and, in order to support the applied load, the slider equilibrium position diminishes dramatically.

6.3.3 Hysteresis of the slider

Would this abrupt change in the equilibrium position of the slider occurs if we change the system configuration by successive approximations? For instance, if once the slider reaches the stationary state we diminish d slightly, and diminish it again after reaching the new stationary state. What would be the final equilibrium variables?.

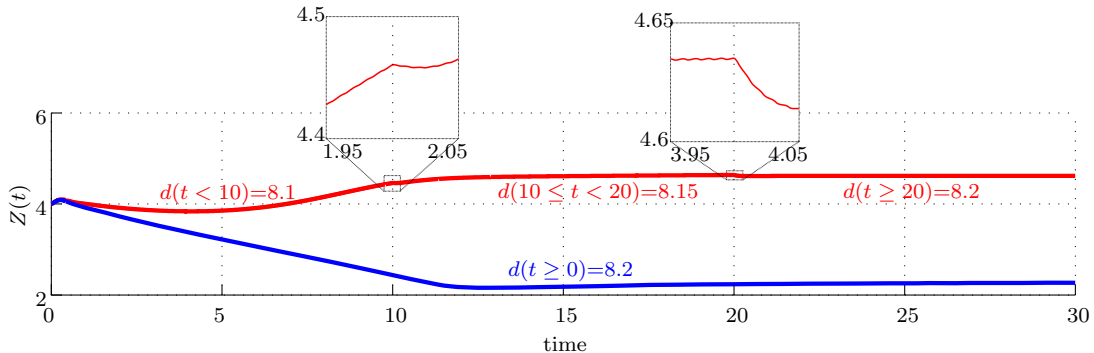


FIGURE 6.5: Hysteresis of the statationary state.

Two different simulations for a fixed curvature $R = 32$ are shown in Figure 6.5. The first simulation, Case A with result in blue, is made with a constant depth $d = 8.2$. The second simulation, Case B with result in red, is such that $d(t) = 8.1$ for $0 \leq t < 10$, $d(t) = 8.15$ for $10 \leq t < 20$ and $d(t) = 8.2$ for $20 \leq t$. For the former case the stationary

average position is equal to $\bar{Z} = 2.27$; for the latter case, after the changes of d are done and the stationary state is reached, the stationary average position is equal to $\bar{Z} = 4.62$.

This unexpected fact is known as Hysteresis, which means that the state of the slider at a particular time t depends on the history of the system.

6.3.4 Cavitation induced oscillations

Observing Figure 6.4, it can be noticed that for both cases considered, $d = 8.1, 8.2$, the cavitation bubbles collapse in different places. For $d = 8.1$ the cavitation bubble collapses at the left of the domain, near the entrance of fluid, and there exists a pressurized zone that extends through more than half of the domain (among other small pressurized zones). On the contrary, for $d = 8.2$ the bubble collapses at the middle of the domain and the cavitation bubble reappears almost immediately, and so there are present many pressurized zones with extension of order $1/\lambda$.

These observations are also valid for both cases A and B presented in the last section. These bubbles collapse were observed to occur during a very small lapse of time. The last creates a sudden expansion of the pressurized zone located at the right of the bubble just collapsed. This sudden change in pressure affects the hydrodynamic force creating oscillations of the position of the slider. These oscillations are shown in Figure 6.6 for the stationary state.

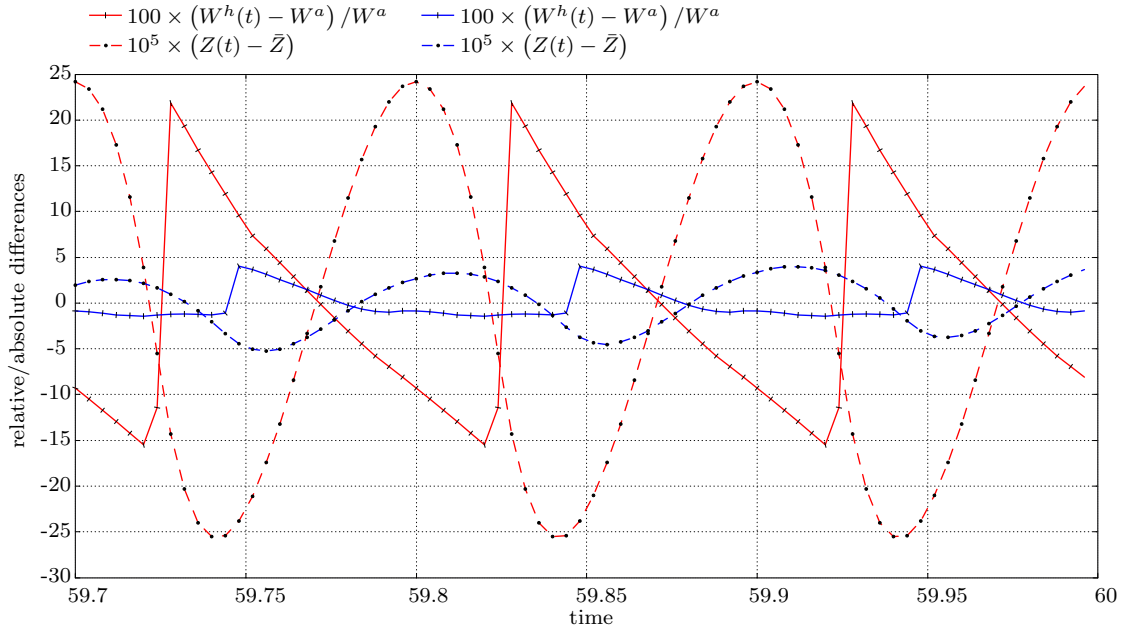


FIGURE 6.6: Hydrodynamic force and slider position oscillations induced by sudden cavitation bubbles collapse for both cases A (in blue) and B (in red).

Please note that the amplitude of the oscillations of the hydrodynamic force $W^h(t)$ is about 5% and 20% of the applied charge W^a for case A and B respectively. These differences may be explained by observing that the pressurized zone placed at the right of the collapsed bubble is around 6 times bigger for Case B than for Case A, which leads to a bigger pressure build-up in Case B. On the other hand, the oscillations of $Z(t)$ are negligible since those are of order $1 \times 10^{-5}[\mu\text{m}]$. Nevertheless, these oscillations associated to sudden collapses of the cavitation bubbles may be an interesting source of future work. Particularly, it would be interesting to address the dependence of these oscillations with the mass of the slider.

Chapter 7

Conclusions and future work

In this work we have done a systematic compilation of theoretical and practical aspects of Lubrication Theory. These studies have involved Fluid Mechanics, Lubrication Theory, Elliptic PDE's from Functional Analysis, Calculus of Variations, and Numerical Analysis from varied aspects like numerical convergence, stability, simulations setup and results interpretation. Nowadays, the organization made here cannot be found in other publications. Therefore, this document could be used by undergraduate/graduate students who want to have a global understanding of the theoretical and practical subjects of the theory addressing modeling and simulation of lubricated contacts. Next, we present particular conclusions from the contents.

We have seen in Chapter 2 that Reynolds equation for the stationary case is satisfied by the limit solutions of the Stokes equations when the proximity parameter H/L goes to zero. This interesting point of view gives more insight into the nature of Reynolds equation when compared to just dropping the terms of order H/L (or higher), as is done in Section §2.1, Lubrication Hypothesis in Navier-Stokes equation.

When considering discontinuities in the gap function h , the mathematical tools needed rely on the theory of PDE's from the Functional Analysis Theory, as it was shown in Chapter 3. In this way, it is possible not just to study the well-posedness of Reynolds equation in the presence of discontinuities but also to give a first approach to a cavitation model by imposing an obstacle to the pressure solution (see Section §4.2, Reynolds model).

The Reynolds cavitation model does not enforce mass-conservation. This key issue can be tackled with the Elrod-Adams cavitation model as presented in Chapter 4. The Elrod-Adams model introduces a change in the type of PDE that models the fluid's

behavior. The analysis of the problem with that change in the PDE type is hard to do, in such a way that nowadays only an existence result is available.

In Chapter 6 we have shown that the models and resolution algorithms presented and studied along the previous chapters of this document can be used effectively for the simulation of one-dimensional slider bearings. It is observed that these results are in line with the literature. Moreover, interesting phenomena can be revealed, such as the catastrophic event depending on the collapse of the cavitation bubbles, and the hysteresis of the stationary state. Also, we have seen how the convergent-divergent geometries of the sinusoidal pockets plays different roles depending on the size of the pressurized zone. Nevertheless, we must emphasize that such discoveries depend upon the models used, as neither the Reynolds model nor the Elrod-Adams model are free of criticism (see for instance [68, 15]).

Next, we present different possibilities to continue the present work.

Limit equations

In Chapter 3 we discussed the work of Bayada and Chambat [8] where it is rigorously proved that Reynolds equation is fulfilled by the limit solutions (in the sense of the proximity of the surfaces) of the Stokes system. However, the hypothesis made on the regularity of the domain, being of class C^1 , is very strong. Also, the gap function h is supposed to be continuously differentiable over the closure of the domain, a hypothesis that is not compatible with real applications as they might involve discontinuous surfaces. It would be interesting to study the possibility of extending this work for weaker regularity hypothesis and, moreover, seek for a similar result for the limit formulas of friction, which were found in Chapter 2 by making use of an asymptotic limit.

Elrod-Adams extensions

The Elrod-Adams model, as discussed by Buscaglia et al. [15] and also by Checo [20], assume the transport velocity of the fluid in the cavitated zone to be $S/2$, i.e., equal to the transport velocity that is obtained when the fluid film is complete. This assumption is not realistic enough for the cases considered in this work, in which most of the lubricant lies on the moving surface (the runner). To extend Elrod-Adams for allowing transport greater than $S/2$ is a challenging problem, lack of uniqueness of solution is one of its difficulties; and an algorithm that automatically keeps track of the cavitation boundary (so-called front-capturing algorithms, e.g., Elrod-Adams algorithm) is not available yet (some efforts on this issue can be found in [20]).

Discontinuous Galerkin

Currently the adopted method has poor mesh flexibility, since it is based on a rectangular grid. Its convergence order is also low, as shown in Section §5.2 Numerical implementation of Reynolds equation and cavitation models, because it assumes a piecewise constant interpolation of the variables. Standard high order methods cannot be applied because of the spontaneously-generated discontinuities at cavitation boundaries. With this perspective, it would be interesting to set focus on Discontinuous Galerkin (DG) Methods, which overcome these issues for elliptic problems [29], hyperbolic problems [27, 28], and elastohydrodynamic lubrication problems [63].

A deep study of DG methods can be found in [3]. The change of type of PDE, from elliptic to hyperbolic at the cavitation boundaries, makes it an interesting application of DG approximation techniques. Further, the generalized cavitation model developed by Buscaglia et al [15, 4], which allows to vary the transport velocity, requires the imposition of inflow boundary conditions at the cavitation boundary. This would certainly require some specific development of DG techniques.

Boundary conditions for pressure

The current cavitation models only admit a constant cavitation pressure, and it must be equal to the surrounding pressure. This has been questioned by several researchers [82] and is a source of inaccuracy. At some instants in the engine cycle the pressure difference between both sides of the ring pack can reach 100 [atm]. Therefore, it is interesting to include this consideration when developing new cavitation models.

Appendix A

Second order MAC scheme for Navier-Stokes equations

The finite volume method is presented here along with a staggered MAC (marker-and-cell) mesh. The adopted notation corresponds to Chapter 2 of *Computational Methods for Multiphase Flow*, Prosperetti and Tryggvason (2009). Further details can be found in the referenced book.

The 2D Navier-Stokes equations (2.28) and (2.29) and the incompressibility condition (2.30) resp. are written in the discrete version ($dx \equiv h$)

$$\frac{\mathbf{u}^{n+1} - \mathbf{u}^n}{\Delta t} + \mathbf{A}_h(\mathbf{u}^n) = -\frac{1}{\rho} \nabla_h p + \mu \mathbf{D}_h \mathbf{u}^n, \quad (\text{A.1})$$

$$\nabla_h \cdot \mathbf{u}^{n+1} = 0, \quad (\text{A.2})$$

where n is the index of the time step and Δt its length. \mathbf{A}_h , \mathbf{D}_h and ∇_h are approximations of the advection, diffusion and gradient operators resp..

Figure A.1 shows the discretization scheme used for solving the Navier Stokes equations in Section §2.4. The first step is to generate an approximated version Ω_h of the domain Ω (see Figure A.1). The volume schematized in Figure A.1 is used to determine the equation involving the unknown pressure $p_{i,j}$. The same is done to determine the equation for the velocity $u_{i+\frac{1}{2},j}$, but this time the control volume is shifted as the left scheme of Figure A.2 shown. At the right side of that figure the scheme of the control volume for $v_{i,j+\frac{1}{2}}$ is shown.

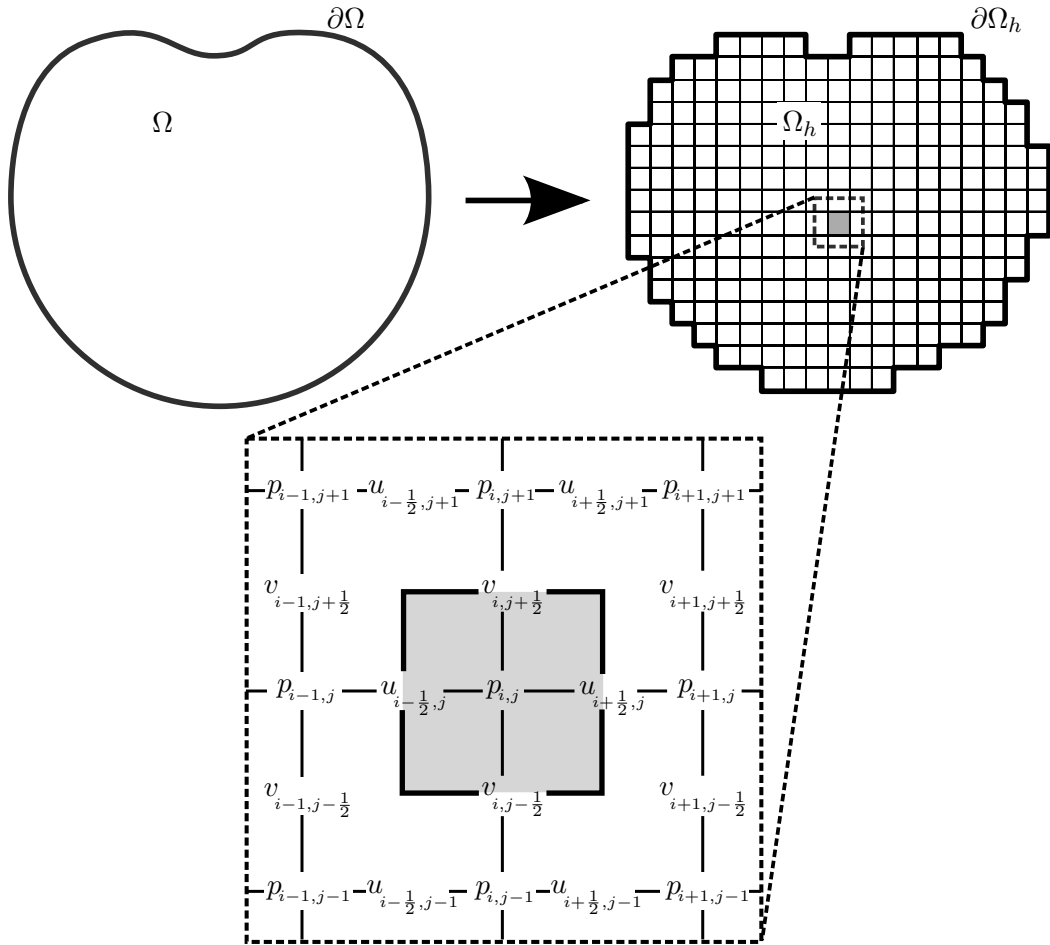


FIGURE A.1: Staggered MAC discretization by Finite Volume Methods. Control volume for pressure.

A.1 Discretization of advection and diffusion

Over an arbitrary control volume, the advection of \mathbf{u}^n can be approximated by the average

$$\mathbf{A}(\mathbf{u}^n) = \frac{1}{\Delta V} \int_V \nabla \cdot (\mathbf{u}^n \otimes \mathbf{u}^n) dv = \frac{1}{\Delta V} \oint_{\partial V} \mathbf{u}^n (\mathbf{u}^n \cdot \hat{n}) ds \quad (\text{A.3})$$

Now, based on the corresponding control volume for $u_{i+\frac{1}{2},j}$ and $v_{i,j+\frac{1}{2}}$, the discrete versions of $\mathbf{A}_x(\mathbf{u}^n)$ and $\mathbf{A}_y(\mathbf{u}^n)$ can be written resp. as

$$\begin{aligned} (\mathbf{A}_x)_{i+\frac{1}{2},j}^n &= \frac{1}{h} \left\{ \left(\frac{u_{i+\frac{3}{2},j} + u_{i+\frac{1}{2},j}}{2} \right)^2 - \left(\frac{u_{i+\frac{1}{2},j} + u_{i-\frac{1}{2},j}}{2} \right)^2 \right. \\ &\quad + \left(\frac{u_{i+\frac{1}{2},j+1} + u_{i+\frac{1}{2},j}}{2} \right) \left(\frac{v_{i+1,j+\frac{1}{2}} + v_{i,j+\frac{1}{2}}}{2} \right) \\ &\quad \left. - \left(\frac{u_{i+\frac{1}{2},j} + u_{i+\frac{1}{2},j-1}}{2} \right) \left(\frac{v_{i+1,j-\frac{1}{2}} + v_{i,j-\frac{1}{2}}}{2} \right) \right\}, \\ (\mathbf{A}_y)_{i,j+\frac{1}{2}}^n &= \frac{1}{h} \left\{ \left(\frac{u_{i+\frac{1}{2},j} + u_{i+\frac{1}{2},j+1}}{2} \right) \left(\frac{v_{i,j+\frac{1}{2}} + v_{i+1,j+\frac{1}{2}}}{2} \right)^2 \right. \\ &\quad - \left(\frac{u_{i-\frac{1}{2},j+1} + u_{i-\frac{1}{2},j}}{2} \right) \left(\frac{v_{i,j+\frac{1}{2}} + v_{i-1,j+\frac{1}{2}}}{2} \right) \\ &\quad \left. + \left(\frac{v_{i,j+\frac{3}{2}} + v_{i,j+\frac{1}{2}}}{2} \right)^2 - \left(\frac{v_{i,j+\frac{1}{2}} + v_{i,j-\frac{1}{2}}}{2} \right)^2 \right\}, \end{aligned}$$

and the diffusion of \mathbf{u}_n can be approximated by the average

$$\mathbf{D}(\mathbf{u}^n) = \frac{1}{\Delta V} \int_V \nabla^2 \mathbf{u}^n dv. \quad (\text{A.4})$$

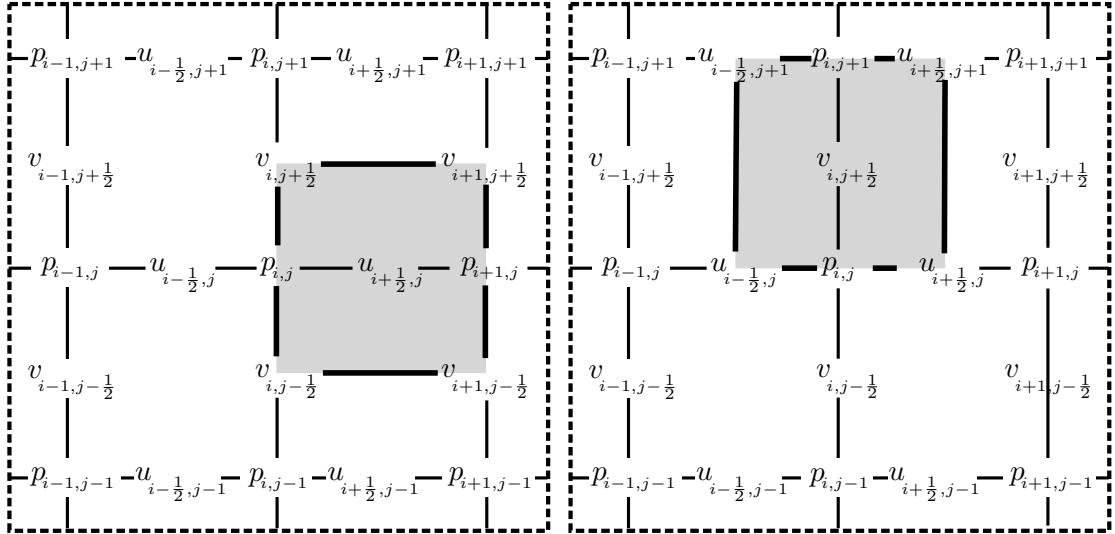


FIGURE A.2: Control volumes for u (left) and v (right). Adapted from [73].

This way, the discrete version of the diffusion on $u_{i+\frac{1}{2},j}$ and $v_{i,j+\frac{1}{2}}$ is given resp. by

$$\begin{aligned} (\mathbf{D}_x)_{i+\frac{1}{2},j}^n &= \frac{u_{i+\frac{3}{2},j}^n + u_{i-\frac{1}{2},j}^n + u_{i+\frac{1}{2},j+1}^n + u_{i+\frac{1}{2},j-1}^n - 4u_{i+\frac{1}{2},j}^n}{h^2}, \\ (\mathbf{D}_y)_{i,j+\frac{1}{2}}^n &= \frac{v_{i+1,j+\frac{1}{2}}^n + v_{i-1,j+\frac{1}{2}}^n + v_{i,j+\frac{3}{2}}^n + v_{i,j-\frac{1}{2}}^n - 4v_{i,j+\frac{1}{2}}^n}{h^2}. \end{aligned}$$

A.2 Projection Method

The Projection Method was introduced by Chorin [24] and Yanenko [89]. In this approach the velocity is first advanced without taking into account the pressure, resulting into a velocity field that, in general, does not accomplish the non-compressibility condition. After that, the pressure necessary to make the velocity field accomplish with the non-compressibility condition is found, and the velocity field is corrected by adding the pressure gradient.

For this, the momentum equation is split into two parts by introducing a temporal velocity \mathbf{u}^* such that

$$\mathbf{u}^{n+1} - \mathbf{u}^n = (\mathbf{u}^{n+1} - \mathbf{u}^*) + (\mathbf{u}^* - \mathbf{u}^n).$$

Now, a predictor step is made (we adopt a second order Crank-Nicholson scheme [62]) such that the temporary velocity field is found by ignoring the pressure effects:

$$\frac{\mathbf{u}^* - \mathbf{u}^n}{\Delta t} = -\frac{3}{2}\mathbf{A}_h(\mathbf{u}^n) + \frac{1}{2}\mathbf{A}_h(\mathbf{u}^{n-1}) + \frac{\mu}{2}(\mathbf{D}_h\mathbf{u}^n + \mathbf{D}_h\mathbf{u}^*). \quad (\text{A.5})$$

Next, the correction step is

$$\frac{\mathbf{u}^{n+1} - \mathbf{u}^*}{\Delta t} = -\nabla_h \phi^{n+1}, \quad (\text{A.6})$$

where ϕ is related to the pressure by the equation

$$-\nabla \phi^{n+1} = -\frac{1}{\rho} \nabla p^{n+1} + \frac{\mu}{2} (\mathbf{D}_h \mathbf{u}^{n+1} - \mathbf{D}_h \mathbf{u}^*). \quad (\text{A.7})$$

Using central finite differences for the gradient of ϕ , the discrete version of equation (A.6) is written

$$u_{i+\frac{1}{2},j}^{n+1} = u_{i+\frac{1}{2},j}^* - \frac{\Delta t}{\rho h} (\phi_{i+1,j}^{n+1} - \phi_{i,j}^{n+1}), \quad (\text{A.8})$$

$$v_{i,j+\frac{1}{2}}^{n+1} = v_{i,j+\frac{1}{2}}^* - \frac{\Delta t}{\rho h} (\phi_{i,j+1}^{n+1} - \phi_{i,j}^{n+1}). \quad (\text{A.9})$$

Deriving equation (A.6) and using (A.2) we get the next Poisson equation for ϕ

$$\nabla_h^2 \phi^{n+1} = \frac{\nabla \cdot \mathbf{u}^*}{\Delta t}. \quad (\text{A.10})$$

By using an analogous approximation used before for the velocity diffusion in equation (A.4), this time equation (A.10) is discretized as

$$\frac{\phi_{i+1,j}^{n+1} + \phi_{i-1,j}^{n+1} + \phi_{i,j+1}^{n+1} + \phi_{i,j-1}^{n+1} - 4\phi_{i,j}^{n+1}}{h^2} = \frac{\rho}{\Delta t} \left(\frac{u_{i+\frac{1}{2},j}^* - u_{i-\frac{1}{2},j}^* + v_{i,j+\frac{1}{2}}^* + v_{i,j-\frac{1}{2}}^*}{h} \right). \quad (\text{A.11})$$

Summarizing, once the initial and boundary conditions are established, the steps of the method are:

1. Find the temporal velocity \mathbf{u}^* by solving the equation (rearranging equation (A.5)):

$$\left(\frac{1}{\Delta t} \mathbb{I} - \frac{\mu}{2} \mathbf{D}_h \right) \mathbf{u}^* = -\frac{3}{2} \mathbf{A}_h(\mathbf{u}^n) + \frac{1}{2} \mathbf{A}_h(\mathbf{u}^{n-1}) + \frac{\mu}{2} \mathbf{D}_h \mathbf{u}^n + \frac{1}{\Delta t} \mathbf{u}^n,$$

where \mathbb{I} is the identity operator.

2. Solve the Poisson equation (A.11) for finding the *pseudo-pressure* ϕ .
3. Find the velocity at time $n + 1$ by using equations (A.8) and (A.9).

Remark A.1. If needed, at some time step the pressure p can be obtained by solving equation (A.7).

Appendix B

Mathematical background

In this Appendix Ω will represent a Lebesgue-measurable subset of \mathbb{R}^n .

Let us make some basic definitions:

Definition B.1. If $\alpha = (\alpha_1, \dots, \alpha_n)$ is an n -tuple of nonnegative integers, we call α a *multi-index* and denote by x^α the monomial $x_1^{\alpha_1} \cdots x_n^{\alpha_n}$, which has degree $|\alpha| = \sum_{i=1}^n \alpha_i$. Similarly, if $D_j = \frac{\partial}{\partial x_j}$ for $1 \leq j \leq n$, then

$$D^\alpha = D_1^{\alpha_1} \cdots D_n^{\alpha_n}$$

denotes a differential operator of order $|\alpha|$, with $D^{(0, \dots, 0)}u = u$.

Definition B.2. We denote as $C_B^j(\Omega)$ the next class of differentiable functions

$$C_B^j(\Omega) = \{u \in C^j(\Omega) : D^\alpha u \text{ is bounded on } \Omega \text{ for } |\alpha| \leq j\}.$$

Definition B.3. Let $0 < \lambda \leq 1$, the Hölder space $C^{m,\lambda}(\overline{\Omega})$ is the subspace of $C^m(\overline{\Omega})$ of functions ϕ for which, for $0 \leq |\alpha| \leq m$, there exists a constant K such that

$$|D^\alpha \phi(x) - D^\alpha \phi(y)| \leq K \|x - y\|^\lambda, \quad x, y \in \Omega.$$

Definition B.4. Given a point x in \mathbb{R}^n , an open ball B_1 with center at x and an open ball B_2 not containing x , the set $C_x = B_1 \cap \{x + \lambda(y - x) : y \in B_2, \lambda > 0\}$ is called a *finite cone* in \mathbb{R}^n having as vertex the point x .

B.1 Duality and Reflexivity

Let E be a normed linear space. A functional on E is a mapping from E into \mathbb{R} . The space of all bounded linear on E is called the *dual space* of E and is denoted by E^* . It can be shown that E^* is a Banach space under the norm:

$$\|f\|_{E^*} = \sup_{x \neq 0} \frac{|f(x)|}{\|x\|}.$$

The second dual $E^{**} = (E^*)^*$ is called the *bidual space* of E^* . If E^{**} isomorphic to E , then E is called *reflexive*.

B.2 Hilbert Spaces

A mapping $x * y = (x, y)$ from $E \times E$ to \mathbb{R} is an *inner product* on E if it satisfies

- (i) $(x, y) = (y, x)$ for all $x, y \in E$,
- (ii) $(\alpha x + \beta y, z) = \alpha(x, z) + \beta(y, z)$ for all $\alpha, \beta \in \mathbb{R}, x, y, z \in E$,
- (iii) $(x, x) > 0$ for all $x \neq 0, x \in E$.

Definition B.5. Let H be a Hilbert space and $x, y \in H$, we say x is orthogonal to y if $(x, y) = 0$, and we denote it $x \perp y$. A subset $V \subset H$ is orthogonal to some element $x \in H$ if $x \perp y$ for any $y \in V$.

A linear space E equipped with an inner product is called an *inner product space*. Writing $\|x\| = (x, x)^{\frac{1}{2}}$ for $x \in E$, we have

Schwarz inequality

$$|(x, y)| \leq \|x\| \|y\|, \quad (\text{B.1})$$

Triangle inequality

$$\|x + y\| \leq \|x\| + \|y\|, \quad (\text{B.2})$$

Parallelogram law

$$\|x + y\|^2 + \|x - y\|^2 = 2(\|x\|^2 + \|y\|^2). \quad (\text{B.3})$$

As we can see, every inner product space is also a normed space. A *Hilbert space* is defined to be a complete inner product space.

The next are two basic properties of a bilinear form.

Definition B.6. Let $a : H \times H \rightarrow \mathbb{R}$ be a bilinear form, with H a real Hilbert space, then we say a is *continuous* if there exists a constant $C > 0$ such that

$$|a(x, y)| \leq C \|x\| \|y\|, \quad \forall x, y \in H.$$

Definition B.7. Let H be a real Hilbert space. A bilinear form $a : H \times H \rightarrow \mathbb{R}$ is *coercive* if there exists a constant $\alpha > 0$ such that

$$a(x, x) \geq \alpha \|x\|^2, \quad \forall x \in H.$$

The Stampacchia and Lax-Milgram Theorems

Stampacchia and Lax-Milgram Theorems are very important analysis tools that permit us to study the well-posedness of a large group of Partial Differential Equations (see, for instance, Chapter 9 and 10 in [13]). Addressing well-posedness of problems for which its variational formulation concerns a variational inequality we have the next

Theorem B.8 (Stampacchia). *Assume that a is a continuous coercive bilinear form on the Hilbert space $(H, (\cdot, \cdot))$. Let $K \subset H$ be a nonempty closed and convex subset. Then, given any $\phi \in H^*$, there exists a unique element $u \in K$ such that*

$$a(u, v - u) \geq (\phi, v - u), \quad \forall v \in K. \tag{B.4}$$

As a consequence of this theorem, we have

Corollary B.9 (Lax-Milgram Theorem). *Assume that a is a continuous coercive bilinear form on the Hilbert space $(H, (\cdot, \cdot))$. Then, given any $\phi \in H^*$, there exists a unique element $u \in H$ such that*

$$a(u, v) = (\phi, v), \quad \forall v \in H. \tag{B.5}$$

Moreover, if a is symmetric, then u is characterized by the property

$$u \in H \text{ and } \frac{1}{2}a(u, u) - (\phi, u) = \min_{v \in H} \left\{ \frac{1}{2}a(v, v) - (\phi, v) \right\}.$$

For a proof of Stampacchia and Lax-Milgram Theorems see [13].

B.3 L^p spaces

Definition and some basic properties

Definition B.10. Given a real number $1 \leq p < \infty$, we define the space $L^p(\Omega)$ by

$$L^p(\Omega) = \{f : \Omega \rightarrow \mathbb{R} \text{ measurable such that } \int_{\Omega} |f|^p d\mu < \infty\}.$$

And the next quantity can be proved to be a norm on $L^p(\Omega)$

$$\|f\|_{L^p(\Omega)} = \left(\int_{\Omega} |f|^p d\mu \right)^{\frac{1}{p}}.$$

Definition B.11. Let f be a function from *essential supremum* of f as

$$\text{ess sup}_{x \in \Omega} f(x) = \inf_{\mu(A)=0} \left(\sup_{x \in \Omega \setminus A} f(x) \right) = \inf \{M \in \mathbb{R} : f(x) \leq M \text{ a.e. in } \Omega\}.$$

Definition B.12. We denote by $L^\infty(\Omega)$ the set of measurable functions from Ω to \mathbb{R} such that their essential supremum is finite. Moreover, it can be proved that

$$\|f\|_{L^\infty(\Omega)} = \text{ess sup}_{x \in \Omega} f(x)$$

is a norm on $L^\infty(\Omega)$.

We call *Hölder conjugate* of p , $1 < p < \infty$, the number p' such that $\frac{1}{p} + \frac{1}{p'} = 1$. If $p = 1$ we take $p' = \infty$ and if $p = \infty$ we take $p' = 1$.

Lemma B.13 (Hölder's Inequality). *Let $p \in [1, \infty]$ and p' be its Hölder conjugate. Let $f \in L^p(\Omega)$ and $g \in L^{p'}(\Omega)$. Then $f g \in L^1(\Omega)$ and*

$$\|fg\|_{L^1(\Omega)} \leq \|f\|_{L^p(\Omega)} \|g\|_{L^{p'}(\Omega)}.$$

As immediate consequences of Hölder's Inequality we have

Lemma B.14. *Let $1 < p \leq q \leq \infty$, $\Omega \subset \mathbb{R}^n$, $\mu(\Omega) < \infty$. Then*

- $L^q(\Omega) \subset L^p(\Omega)$,
- $\|f\|_{L^p(\Omega)} \leq C \|f\|_{L^q(\Omega)}$, where C only depends on Ω .

Definition B.15. We define the class of locally integrable functions on Ω as

$$L^1_{\text{loc}}(\Omega) = \{f : f \in L^1(\omega) \text{ } \forall \omega \text{ compact measurable subset of } \Omega\}.$$

As a consequence of $L^1_{loc}(\Omega)$ definition and Lemma B.14 we have the next

Lemma B.16. *For any p , $1 \leq p \leq \infty$ we have*

$$L^p(\Omega) \subset L^1_{loc}(\Omega).$$

Lemma B.17. *Let $f \in L^1_{loc}(\Omega)$ such that*

$$\int_{\Omega} f \phi dx = 0, \quad \forall \phi \in C_0^\infty(\Omega),$$

then $f = 0$ a.e. on Ω .

Lemma B.18. *Let $f \in L^1_{loc}(\Omega)$ such that*

$$\int_{\Omega} f \phi dx \geq 0, \quad \forall \phi \in C_0^\infty(\Omega) : \phi \geq 0,$$

then $f \geq 0$ a.e. on Ω .

Completeness and reflexivity

Theorem B.19 (Fischer-Riez). *Let $p \in [1, \infty]$, $\Omega \subset \mathbb{R}^n$, $\mu(\Omega) > 0$. Then $L^p(\Omega)$ is a Banach space with the corresponding norm defined above.*

Theorem B.20. *The next identification holds*

$$(L^1(\Omega))^* = L^\infty(\Omega).$$

Theorem B.21. *$L^p(\Omega)$ is reflexive if and only if $1 < p < \infty$. Moreover, the next identification holds*

$$(L^p(\Omega))^* = L^{p'}(\Omega).$$

Remark B.22. *From this last theorem we have that $L^2(\Omega)$ is a Hilbert space.*

The proofs of all these results concerning L^p spaces can be found in Chapter 4 of [13].

B.4 Sobolev Spaces

This section starts introducing the concept of *weak derivative*. For this, let $I = [0, 1] \subset \mathbb{R}$, take some function $f \in C^1(I)$ and suppose the function g is such that

$$\frac{df}{dx} = g \quad \text{on } I. \tag{B.6}$$

Multiplying this last equation by some arbitrary function $\phi \in C_0^\infty(I)$, and integrating on I we have

$$\int_0^1 \phi \frac{df}{dx} dx = \int_0^1 \phi g dx,$$

$$(\phi f) |_0^1 - \int_0^1 f \frac{d\phi}{dx} dx = \int_0^1 \phi g dx,$$

and as $\phi(0) = \phi(1) = 0$ we obtain

$$\int_0^1 f \frac{d\phi}{dx} dx = - \int_0^1 \phi g dx, \quad \forall \phi \in C_0^\infty(I). \quad (\text{B.7})$$

We see that for any function $f \in C^1(I)$, if g accomplishes equation (B.6) it will accomplish equation (B.7), and the inverse calculations are also true (using Lemma B.17 and some facts from Integration Theory), i.e., for any function $f \in C^1(I)$ for which g accomplishes equation (B.7), then g will accomplish equation (B.6). In other words, g will be the *classical derivative* of f . However, we can ask for solving equation (B.7) when f have less regularity.

Take this time $I = [-1, 1]$ and the function $q(x) = |x|$, we have $q \in L^2(I)$ but $q \notin C^1(I)$. We ask for a function $Q \in L_{\text{loc}}^1(I)$ that solves the equation

$$\int_I q \frac{d\phi}{dx} dx = - \int_I \phi Q dx, \quad \forall \phi \in C_0^\infty(I). \quad (\text{B.8})$$

For this, consider the function $Q \in L^2(I)$ such that

$$Q(x) = \begin{cases} -1 & \text{if } -1 \leq x \leq 0, \\ +1 & \text{if } 0 \leq x \leq 1, \end{cases}$$

It can be easily proved that Q accomplish equation (B.8) for q ; moreover, as $Q \in L_{\text{loc}}^1(I)$, by using Lemmas B.14 and B.17, it can be easily proved that Q is the only function in $L_{\text{loc}}^1(I)$ having that property (up to a set of zero measure). Thus, the discontinuous function Q is some sort of “new derivative” for the continuous and not classically differentiable function q . At the same time, we try to look for some function $Q \in L_{\text{loc}}^1(I)$ accomplishing now the equation

$$\int_I Q \frac{d\phi}{dx} dx = - \int_I \phi Q dx, \quad \forall \phi \in C_0^\infty(I). \quad (\text{B.9})$$

But this time this will not be possible if we find for $Q \in L_{\text{loc}}^1(I)$. In fact, equation (B.9) can be solved in an even more general sense, but this is beyond the scope of this text. The interested reader can look for Section “Distributions and Weak Derivatives”, Chap. I of [1] and also in [30].

Definitions

As we discussed above, there are cases where this new sense of derivative can be found for functions in $L^1_{\text{loc}}(\Omega)$ and others where it cannot. With this in mind, we write down the next

Definition B.23. Let $f \in L^1_{\text{loc}}(\Omega)$, we say that $g_\alpha \in L^1_{\text{loc}}(\Omega)$ is the *weak partial derivative of f* if it satisfies

$$\int_{\Omega} f D^\alpha \phi \, dx = (-1)^{|\alpha|} \int_{\Omega} g_\alpha \phi \, dx, \quad \forall \phi \in C_0^\infty(\Omega). \quad (\text{B.10})$$

Definition B.24 (Sobolev Spaces). We denote as $W^{m,p}(\Omega)$ the class of weakly differentiable functions in $L^p(\Omega)$ such that

$$W^{m,p}(\Omega) = \{u \in L^p(\Omega) : D^\alpha u \in L^p(\Omega) \text{ for } 0 \leq |\alpha| \leq m, D^\alpha u: \text{weak derivatives of } u\},$$

$$W_0^{m,p}(\Omega) = \text{the closure of } C_0^\infty(\Omega) \text{ in } W^{m,p}(\Omega).$$

$(W^{m,p}(\Omega), \|\cdot\|_{m,p})$ are called Sobolev Spaces over Ω with

$$\|u\|_{m,p} = \begin{cases} \left(\sum_{0 \leq |\alpha| \leq m} \|D^\alpha u\|_p^p \right)^{\frac{1}{p}} & \text{if } 1 \leq p < \infty, \\ \max_{0 \leq |\alpha| \leq m} \|D^\alpha u\|_\infty & \text{if } p = \infty. \end{cases} \quad (\text{B.11})$$

Also, we denote $H^m(\Omega) = W^{m,2}(\Omega)$, $H_0^m(\Omega) = W_0^{m,2}(\Omega)$, $H^{-m}(\Omega) = (H^m(\Omega))^*$ and $H_0^{-m}(\Omega) = (H_0^m(\Omega))^*$.

Next, we mention some important properties of Sobolev Spaces.

Theorem B.25. $W^{m,p}(\Omega)$ is a Banach space, $H^m(\Omega)$ is a Hilbert space.

Theorem B.26. Let $u, v \in H^1(\Omega) \cap L^\infty(\Omega)$, then $uv \in H^1(\Omega) \cap L^\infty(\Omega)$ and

$$\frac{\partial}{\partial x_i}(uv) = v \frac{\partial u}{\partial x_i} + u \frac{\partial v}{\partial x_i} \quad i = 1, 2 \dots n.$$

For the case $\Omega =]a, b[$ an open subset of \mathbb{R} , the hypothesis can be relaxed to $u, v \in H^1(\Omega)$ (see Corollary 8.8 in [13]).

Theorem B.27. $W^{m,p}(\Omega)$ is separable for $1 \leq p < \infty$; also, it is uniformly convex, and thus reflexive if $1 < p < \infty$. In particular, $W^{m,2}(\Omega)$ is a separable Hilbert space with inner product

$$(u, v)_m = \sum_{0 \leq |\alpha| \leq m} (D^\alpha u, D^\alpha v),$$

where $(u, v) = \int_{\Omega} uv \, dx$ is the inner product in $L^2(\Omega)$.

Once the well-posedness of a problem is established, we may ask for the regularity of the solution. Sobolev Imbeddings are a set of results addressing that kind of question. Before presenting Sobolev Imbeddings, we need to talk about regularity of the domain $\Omega \subset \mathbb{R}^n$ on which the problem is being studied:

Definition B.28. Ω is said to have the *cone property* if there exists a finite cone C such that each point $x \in \Omega$ is the vertex of a finite cone C_x contained in Ω and congruent to C .

Definition B.29. Ω bounded is said to have the *local Lipschitz property* if at each point x on the boundary of Ω there is a neighborhood U_x such that $\partial\Omega \cap U_x$ is the graph of a Lipschitz continuous function.

Sobolev Imbeddings and Trace Theory

A deep study of these Imbeddings can be found in [1], the interested reader can review that work for the proofs of the next results.

Definition B.30. Let X, Y be two normed spaces, a linear application $A : X \rightarrow Y$ is called *compact* if for any sequence $(x_n) \subset X$ there exists a subsequence (x_{n_k}) such that the sequence (Ax_{n_k}) is convergent in Y . We also say that X is *imbedded* in Y and it is denoted $X \subset\subset Y$. This also means that there is a constant K , named the *imbedding constant* such that, for any $y \in X$ we have

$$\|y\|_X \leq K \|Ay\|_Y.$$

Theorem B.31. Let Ω be a domain in \mathbb{R}^n having the cone property.

- If $mp < n$, then $W^{m,p}(\Omega) \subset\subset L^q(\Omega)$ for $p \leq q \leq np/(n - mp)$.
- If $mp = n$, then $W^{m,p}(\Omega) \subset\subset L^q(\Omega)$ for $p \leq q < \infty$.
- If $mp > n$, then $W^{j+m,p}(\Omega) \subset\subset C_B^j(\Omega)$.

The imbedding constants may be chosen to depend only on m, p, n, q and the cone C determining the cone property for Ω .

Theorem B.32. Let Ω be a bounded domain in \mathbb{R}^n having the local Lipschitz property, and suppose that $mp > n \geq (m - 1)p$. Then $W^{m,p}(\Omega) \subset\subset C^{0,\lambda}(\bar{\Omega})$ with

- $0 < \lambda \leq m - n/p$ if $n > (m - 1)p$,
- $0 < \lambda < 1$ if $n = (m - 1)p$,

- $0 < \lambda \leq 1$ if $p = 1$, $n = m - 1$.

In particular $W^{m,p}(\Omega) \subset\subset C^0(\bar{\Omega})$. The imbedding constants depend on m , p and n .

Definition B.33 (Fractional Sobolev Spaces). Take $\Omega \subset \mathbb{R}^n$ finite measurable subdomain, $s, p \in \mathbb{R}$, $0 < s < 1$ and $1 \leq p < \infty$, the fractional Sobolev Space $W^{s,p}(\Omega)$ as

$$W^{s,p}(\Omega) = \left\{ u \in L^p(\Omega) : \frac{|u(x) - u(y)|}{\|x - y\|^{s+n/p}} \in L^p(\Omega \times \Omega) \right\},$$

equipped with the natural norm. And set $H^s(\Omega) = W^{s,2}(\Omega)$.

We have the next fundamental

Lemma B.34. Let $1 \leq p < \infty$. Let $\Omega = \mathbb{R}_+^n$. There exists a constant C such that

$$\left(\int_{\mathbb{R}^{n-1}} |u(x', 0)|^p dx' \right)^{\frac{1}{p}} \leq C \|u\|_{W^{1,p}(\Omega)}.$$

From this Lemma it can be deduced that the map $u \rightarrow u|_{\partial\Omega} = \mathbb{R}^{n-1} \times \{0\}$ defined from $C_0^1(\mathbb{R}^n)$ into $L^p(\Omega)$ extends, by density, to a bounded linear operator of $W^{1,p}(\Omega)$ into $L^p(\partial\Omega)$. We call this operator the *trace* of u on $\partial\Omega$, denoted by $u|_{\partial\Omega}$. Assuming Ω accomplishes the local Lipschitz property, we have the next important properties of the trace:

- If $u \in W^{1,p}(\Omega)$, then in fact $u|_{\partial\Omega} \in W^{1-1/p,p}(\partial\Omega)$. Furthermore, the trace operator $u \rightarrow u|_{\partial\Omega}$ is surjective from $W^{1,p}(\Omega)$ onto $W^{1-1/p,p}(\partial\Omega)$.
- The kernel of the trace operator is $W_0^{1,p}(\Omega)$, i.e.,

$$W_0^{1,p} = \{u \in W^{1,p}(\Omega) : u|_{\partial\Omega} = 0\}.$$

- We have Green's formulas, for any $u, v \in H^1(\Omega)$

$$\begin{cases} \int_{\Omega} v \frac{\partial u}{\partial x} dx = - \int_{\Omega} u \frac{\partial v}{\partial x} + \int_{\partial\Omega} u v \cos(\hat{\mathbf{n}}, \hat{\mathbf{e}}_1) d\sigma \\ \int_{\Omega} v \frac{\partial u}{\partial y} dx = - \int_{\Omega} u \frac{\partial v}{\partial y} + \int_{\partial\Omega} u v \cos(\hat{\mathbf{n}}, \hat{\mathbf{e}}_2) d\sigma, \end{cases} \quad (\text{B.12})$$

where $\hat{\mathbf{n}}$ is the outward unit vector normal to $\partial\Omega$ and $\hat{\mathbf{e}}_1, \hat{\mathbf{e}}_2$ are the unitary vector pointing positively along x and y resp.. Note that the surface integral have sense since $u, v \in L^2(\partial\Omega)$.

Regularity results

Consider the following PDE

$$\begin{cases} Lu = f_0 + \sum_{i=1}^n \frac{\partial f_i}{\partial x_i}, & \text{on } \Omega \\ u = 0, & \text{on } \partial\Omega, \end{cases} \quad (\text{B.13})$$

where Ω is an open set in \mathbb{R}^n and L is a uniformly elliptic of the form

$$Lu = - \sum_{i,j=1}^n \frac{\partial}{\partial x_i} \left(a_{ij} \frac{\partial u}{\partial x_j} \right)$$

We have the following theorem (see for example [78], section 5.7)

Theorem B.35. *Assume that $a_{ij} \in L^\infty(\Omega)$, $f_i \in L^p(\Omega)$, $f_0 \in L^{p/2}(\Omega)$, for $p > n \geq 2$ and Ω a bounded set with Lipschitz-boundary. If $u \in H_0^1(\Omega)$ is a weak solution of (B.13) then $u \in C^{0,\alpha}(\bar{\Omega})$, and*

$$\|u\|_{C^{0,\alpha}(\bar{\Omega})} \leq C \left(\|f_0\|_{L^{p/2}(\Omega)} + \sum_{i=1}^n \|f_i\|_{L^p(\Omega)} \right)$$

where the constant C depends only on n, p, α, Ω and a_{ij} .

Consider now the corresponding obstacle problem in the variational inequality form

$$u \in K_\psi : a(u, v - u) \geq \int_{\Omega} f_0(v - u) - \sum_{i=1}^n \int_{\Omega} f_i \frac{\partial}{\partial x_i} (v - u) \quad (\text{B.14})$$

where $a(u, v) = \sum_{i,j=1}^n a_{ij} \partial_{x_i} u \partial_{x_j} v$ and

$$K_\psi = \{v \in H^1(\Omega) : v \geq \psi \text{ in } \Omega\}. \quad (\text{B.15})$$

We have the next regularity result (see for instance [78], section 5.7)

Theorem B.36. *Under the same assumptions of Theorem B.35, assume in addition that for some $0 < \beta < 1$, $\psi \in C^{0,\beta}(\Omega)$. Then the unique solution of (B.14) is such that*

$$u \in C^{0,\gamma}(\bar{\Omega}) \cap K_\psi$$

with $0 < \gamma < 1$.

We have a stronger result for the one-dimensional obstacle problem. Suppose $\Omega =]a, b[$ is an open interval of \mathbb{R} , then we have the next result

Theorem B.37. *Under the same assumptions of Theorem B.35, assume in addition that*

$$\psi \in H^1(a, b), \quad \max_{]a,b[} \psi > 0, \quad \psi(a) < 0, \psi(b) < 0$$

and that ψ' has only discontinuities of the form

$$\psi'(x^-) \leq \psi'(x^+).$$

Then u' is continuous.

The proof of this theorem can be found in Section 7, Chapter II of [58].

Bibliography

- [1] Adams, R. A. *Sobolev Spaces*. Academic Press, 1st edition, 1975.
- [2] Ali, F., Křupka, I., and Hartle, M. Analytical and experimental investigation of friction of non-conformal point contacts under starved lubrication. *Meccanica*, (48):545–553, October 2012.
- [3] Arnold, D., Brezzi, F., Cockburn, B., and Marini, L. Unified Analysis of Discontinuous Galerkin Methods for Elliptic Problems. *SIAM J. Numer. Anal.*, 39(5):1749–1779, 2001.
- [4] Ausas, R., Jai, M., Ciuperca, I. S., and Buscaglia, G. C. Conservative one-dimensional finite volume discretization of a new cavitation model for piston-ring lubrication. *Tribol. Int.*, 57:54–66, 2013.
- [5] Ausas, R., Ragot, P., Leiva, J., Jai M. Bayada, G., and Buscaglia, G. The impact of the Cavitation model in the Analysis of Micro-Textured Lubricated Journal bearings. *ASME J. Tribol.*, 129:868–875, 2007.
- [6] Ausas, R., Sousa, F. S., and Buscaglia, G. C. An improved finite element space for discontinuous pressures. *CMAME, in press, DOI: 10.1016/j.cma.2009.11.011*, 2009.
- [7] Bayada, G. and Chambat, M. Nonlinear Variational Formulation for a Cavitation Problem in Lubrication. *Journal of Mathematics Analysis and Applications*, 89:286–298, 1982.
- [8] Bayada, G. and Chambat, M. The transition between the Stokes equations and the Reynolds equation: A mathematical proof. *Applied Mathematics & Optimization*, 14(1):73–93, 1986.
- [9] Bayada, G. and Chambat, M. New models in the theory of the hydrodynamic lubrication of rough surfaces. *ASME J. Tribol.*, 110(3), 1988.
- [10] Bonito, A., Devore, R. A., and Nochetto, R. H. Adaptive finite element methods for elliptic problems with discontinuous coefficients. *SIAM J. Numer. Anal.*, 51(6):24, 2013.

- [11] Braun, M. and Hannon, W. Cavitation formation and modelling for fluid film bearings: A review. *J. Engineering Tribol.*, 224:839–863, 2010.
- [12] Brenner, S. C. and Scott, R. *The Mathematical Theory of Finite Element Methods*. Springer, 2nd edition, 2002.
- [13] Brezis, H. *Functional Analysis, Sobolev Spaces and Partial Differential Equations*. Springer, 1st edition, 2011.
- [14] Buscaglia, G. C. and Ausas, R. Variational formulations for surface tension, capillarity and wetting. *Computer Methods in Applied Mechanics and Engineering*, 70:829–850, 2012.
- [15] Buscaglia, G. C., Ciuperca, I., Dalissier, E., and Jai, M. A new cavitation model in lubrication: the case of two-zone cavitation. *Journal of Engineering Mathematics*, 83:57–79, 2013.
- [16] Buscaglia, G. C., Ciuperca, I., and Jai, M. The effect of periodic textures on the static characteristics of thrust bearings. *ASME J. Tribol.*, 127:899–902, 2005.
- [17] Buscaglia, G. C. and Talibi Mohamed E. Jai, M. Mass-conserving cavitation model for dynamical lubrication problems. Part I: Mathematical analysis. *Mathematics and Computers in Simulation*, December 2014.
- [18] Cameron, A. *Basic lubrication theory*. Longman Group Ltd., 1971.
- [19] Céa, J. *Optimization - Theory and Algorithms*. Tata Institute of Fundamental Research, 1978.
- [20] Checo, H. M. Models and methods for the direct simulation of rough and micropatterned surfaces. PhD thesis. Instituto de Ciências Matemáticas e de Computação, USP, forthcoming.
- [21] Checo, H. M., Ausas, R., Jai, M., Cadalen, J., Choukroun, F., and Buscaglia, G. C. Moving textures: Simulation of a ring sliding on a textured liner. *Tribol. Int.*, 72:131–142, 2014.
- [22] Checo, H. M., Jaramillo, A., Jai, M., and Buscaglia, G. C. Texture-Induced cavitation bubbles and friction reduction in the Elrod-Adams Model. *Proc. Inst. Mech. Eng. J. J. Eng. Tribol.*, 229(4):478–492, 2015.
- [23] Checo, H. M., Jaramillo, A., Jai, M., and C., Buscaglia G. Tribological Performance of Textured Surfaces in the Piston Ring/Liner Contact using the Elrod-Adams Model. *XXI Congreso sobre Métodos Numéricos y sus Aplicaciones, ENIEF 2014. Instituto Balseiro - Centro Atómico Bariloche*, 2014.
- [24] Chorin, A. J. Numerical solution of the Navier-Stokes equations. *Math. Comput.*, 22(104):745–762, 1968.

- [25] Christopherson, D. G. A new mathematical method for the solution of film lubrication problems. 1941.
- [26] Cimatti, G. On a problem of the theory of lubrication governed by a variational inequality. English. *Applied Mathematics and Optimization*, 3(2-3):227–242, 1976.
- [27] Cockburn, B. Devising discontinuous Galerkin methods for non-linear hyperbolic conservation laws. *Journal of Computational and Applied Mathematics*, 128(1-2):187–204, 2001.
- [28] Cockburn, B. Discontinuous Galerkin Methods. *AMS*:1–25, 2003.
- [29] Codina, R. and Badia, S. On the design of discontinuous Galerkin methods for elliptic problems based on hybrid formulations. *Computer methods in applied mechanics and engineering*, 263:158–168, 2013.
- [30] Cordaro, P. D. and Kawano, A. *O delta de Dirac: uma introdução a teoria das distribuições para a Engenharia*. Livraria da Física, 2002.
- [31] Costa, H. L. and Hutchings, I. M. Hydrodynamic lubrication of textured steel surfaces under reciprocating sliding conditions. *Tribol. Int.*, 40:1227–1238, 2007.
- [32] Cryer, C. W. The method of Christopherson for solving free boundary problems for infinite journal bearings by means of finite differences. *Mathematics of Computation*, 25(115):435–435, September 1971.
- [33] Dobrica, M. B., Fillon, M., Pascoivici, M. D., and Ciccone, T. Optimizing surface texture for hydrodynamic lubricated contacts using a mass-conserving numerical approach. *Proc. IMechE*, 224:737–750, 2010.
- [34] Dobrica, M. and Fillon, M. About the validity of Reynolds equation and inertia effects in textured sliders on infinite width. *Proc. IMechE*, 223:69–78, 2008.
- [35] Dowson, D. and Taylor, C. Cavitation in bearings. *Annu. Rev. Fluid Mech.*, 11:35–66, 1979.
- [36] Elrod, A. A general theory for laminar lubrication with Reynolds roughness. *J. Lubric. Tech-T ASME*, 101:8–14, 1988.
- [37] Elrod, H. G. and Adams, M. A computer program for cavitation. Technical report 190. *1st LEEDS LYON Symposium on Cavitation and Related Phenomena in Lubrication, I.M.E.*, 103:354, 1974.
- [38] Etsion, I. State of the art in laser surface texturing. *J. Tribol.: Trans. ASME*, 127:248–253, 2005.
- [39] Etsion, I. Modeling of surface texturing in hydrodynamic lubrication. *Friction*, 1(3):195–209, July 2013.

- [40] Floberg, L. On journal bearing lubrication considering the tensile strength of the liquid lubricant. *Transactions of the Machine Elements Division, Lund Technical University*:1–26, 1973.
- [41] Floberg, L. Cavitation boundary conditions with regard to the number of streamers and tensile strength of the liquid. *Proceedings of the 1st Leed-Lyon Symposium on Tribology*:31–36, 1974.
- [42] Fortier, A. E. and Salant, R. F. Numerical Analysis of a Journal Bearing With a Heterogeneous Slip/No-Slip Surface. *ASME J. Tribol.*, 127(4):820, 2005.
- [43] Fulton, S. R., Ciesielski, P. E., and Schuber, W. H. Multigrid Methods for Elliptic Problems: A Review. 1986.
- [44] Gadeschi, G. B., Backhaus, K., and Knoll, G. Numerical Analysis of Laser-Textured Piston-Rings in the Hydrodynamic Lubrication Regime. *ASME J. Tribol.*, 134:1–8, October 2012.
- [45] Geradin, M. and Rixen, D. J. *Mechanical Vibrations: Theory and Application to Structural Dynamics*. John Wiley & Sons, 3rd edition, 2015.
- [46] Gherca, A., Fatu, A., Hajjam, M., and Maspeyrot, P. Effects of surface texturing in steady-state and transient flow conditions: Two-dimensional numerical simulation using a mass-conserving cavitation model. *Proc. Inst. Mech. Eng. J. J. Eng. Tribol.*, July 2014.
- [47] Girault, V. and A., Raviart P. *Finite Element Approximation of the Navier-Stokes Equations*. Springer, 1981.
- [48] Glowinski, R. *Lectures on Numerical Methods For Non-Linear Variational Problems*. Tata Institute of Fundamental Research, 1980.
- [49] Golub, G. H. and Van Loan, C. F. *Matrix computations*. Johns Hopkins University Press, 3rd edition, 1996.
- [50] Grabon, W., Koszela, W., Pawlus, P., and Ochwat, S. Improving tribological behaviour of piston ring–cylinder liner frictional pair by liner surface texturing. *Tribol. Int.*, (61):102–108, 2013.
- [51] Greenwood, J. A. and Tripp, J. H. The Contact of Two Nominally Flat Rough Surfaces. *Proceedings of the Institution of Mechanical Engineers*, 185(1):625–633, 1970.
- [52] Greenwood, J. and Williamson, J. Contact of Nominally Flat Surfaces. *Proceedings of the Royal Society of London. Series A, Mathematical and Physical Sciences*, 295:300–319, 1966.

- [53] Güm̄bel, L. K. R. Vergleich der ergebnisse der rectinerischen behandlung des lagerschmieran-gsproblem mit neueren veisuchsergebnissen. *Monatsbl. Berliner Bez. Ver. Dtsch. Ing.*:125–128, September 1921.
- [54] Herbin, R. A Monotonic Method for the Numerical Solution of Some Free Boundary Value Problems. *SIAM Journal on Numerical Analysis*, 40(6):2292–2310, 2002.
- [55] Herbin, R. and Marchand, E. Finite volume approximation of a class of variational. *IMA Journal of Numerical Analysis*, 21:553–585, 2001.
- [56] Holmberg, K., Andersson, P., and Erdemir, A. Global energy consumption due to friction in passenger cars. *Tribol. Int.*, 47:221–234, 2012.
- [57] Jakobson, B. and Floberg, L. The Finite Journal Bearing Considering Vaporization. *Tran. Chalmers University of Technology*, 190:1–119, 1957.
- [58] Kinderlehrer, D. and Stampacchia, G. *An Introduction to Variational Inequalities and Their Applications*. Academic Press, 1st edition, 1980.
- [59] Knapp, R. T., Daily, J. W., and Hammit, F. G. *Cavitation*. McGraw-Hill, 1st edition, 1970.
- [60] Kovalchenko, A., Ajayi, O., Erdemir, A., and Fenske, G. Friction and wear behavior of laser textured surface under lubricated initial point contact. *Wear*, 271:1719–1725, 2011.
- [61] Leveque, R. J. *Finite Volume Methods for Hyperbolic Problems*. Cambridge University Press, 1st edition, 2002.
- [62] Leveque, R. J. *Finite Difference Methods for Ordinary and Partial Differential Equations*. Society for Industrial and Applied Mathematics (SIAM), Philadelphia, 1st edition, 2007.
- [63] Li, H., Berzins, M., Goodyer, C., and Jimack, P. Adaptive high-order Discontinuous Galerkin solution of elastohydrodynamic lubrication point contact problems. *Advances in engineering software*, 45(1):313–324, 2012.
- [64] Medina, S., Fowell, M. T., Vladescu, S., Reddyhoff, T., Pegg, I., Olver, A. V., and Dini, D. Transient effects in lubricated textured bearings. *Proc. Inst. Mech. Eng. J. J. Eng. Tribol.*:1–15, 2015.
- [65] Mezghani, S., Demirci, I., Zahouani, H., and El Mansori, M. The effect of groove texture patterns on piston-ring pack friction. *Precision Engineering*, 36(2):210–217, April 2012.
- [66] Olsson, K. Cavitation in dynamically loaded bearings. *Tran. Chalmers University of Technology*, 308, 1965.

- [67] Optasanu, V. and Bonneau, D. Finite Element Mass-Conserving Cavitation Algorithm in Pure Squeeze Motion. Validation/Application to a Connecting- Rod Small End Bearing. *ASME J. Tribol.*, 122(1):162–169, 2000.
- [68] Organisciak, M. Optimisation de la microgeometrie des chemises de moteurs a combustion interne. PhD thesis. Lyon, France: l’Institut National des Sciences Appliquées de Lyon, 2007.
- [69] Panayi, A. and Schock, H. Approximation of the integral of the asperity height distribution for the Greenwood–Tripp asperity contact model. *Proc. Inst. Mech. Eng. J. J. Eng. Tribol.*, 222:165–169, 2008.
- [70] Phan-Tien, N. On the effects of the reynolds and stokes surface roughnesses in a two- dimensional slider bearing. *Proceedings of the Royal Society of London. Series A, Mathematical and Physical Sciences*, 377(1770):349–362, 1981.
- [71] Priest, M., Dowson, D., and M., Taylor C. Theoretical modelling of cavitation in piston ring lubrication. *Proc. Instn. Mech. Engrs*, 214(1):435–447, 2000.
- [72] Profito, F., Tomanik, E., and Zachariadis, D. Effect of Cylinder Liner Wear on the Mixed Lubrication Regime of TLOCRs. *Tribol. Int.*, 2015.
- [73] Prosperetti, A. and Tryggvason, G. *Computational Methods for Multiphase Flow*. Cambridge University Press, 2009.
- [74] Qiu, Y. and Khonsari, M. On the Prediction of Cavitation in Dimples Using a Mass-Conservative Algorithm. *ASME, J. of Trib.*, 131:041702–1, 2009.
- [75] Rahmani, R., Shirvani, A., and Shirvani, H. Analytical analysis and optimisation of the Rayleigh step slider bearing. *Tribol. Int.*, 42(5):666–674, May 2009.
- [76] Rayleigh, Lord. Notes on the theory of lubrication. *Philosophical Magazine Series 6*, 35(205):1–12, January 1918.
- [77] Reynolds, O. On the Theory of Lubrication and Its Application to Mr. Beauchamp Tower’s Experiments, Including an Experimental Determination of the Viscosity of Olive Oil. *Phil. Trans.*, 177:157–234, 1886.
- [78] Rodrigues, J. F. *Obstacle Problems in Mathematical Physics*. North-Holland: Mathematics Studies, 1987.
- [79] Ryk, G. and Etsion, I. Testing piston rings with partial laser surface texturing for friction reduction. *Wear*, 261:792–796, 2006.
- [80] Salant, Richard F. and Fortier, A. E. Numerical Analysis of a Slider Bearing with a Heterogeneous Slip/No-Slip Surface. *Tribology Transactions*, 47(3):328–334, 2004.
- [81] Scaraggi, M., Mezzapesa, F. P., Carbone, G., Ancona, A., and Tricarico, L. Friction Properties of Lubricated Laser-MicroTextured-Surfaces: An Experimental Study from Boundary- to Hydrodynamic-Lubrication. *Tribol. Lett.*, 49:117–125, 2013.

- [82] Shen, C. and Khonsari, M. M. Effect of Dimple's Internal Structure on Hydrodynamic Lubrication. *Tribol. Lett.*, 52:415–430, 2013.
- [83] Sommerfeld, A. Zur hydrodynamiscien theorie der schmiermittehreibung. *Z. Math. Phys.*:97–155, 1904.
- [84] Song, D. J., Seo, D. K., and Schultz, W. W. A comparison study between navier-stokes equation and reynolds equation in lubricating flow regime. *KSME International Journal*, 17(4), 2003.
- [85] Tomanik, E. Friction and wear bench test of different engine liner surface finishes. *Tribol. Int.*, 41:1032–1038, 2008.
- [86] Tomanik, E. Modelling the hydrodynamic support of cylinder bore and piston rings with laser textured surfaces. *Tribol. Int.*, 59:90–96, 2013.
- [87] Trudinger, N. S. and Gilbar, D. *Elliptic Partial Differential Equations of Second Order*. Springer-Verlag, 2nd edition, 1983.
- [88] Wang, Q. J. and Chung, Y. *Encyclopedia of Tribology*. Springer, 1st edition, 2013.
- [89] Yanenko, N. N. *The method of fractional steps, the solution of problems of mathematical physics in several variables*. Spriger-Verlag, 1971.
- [90] Yin, B., Li, X., Fu, Y., and Yun, W. Effect of laser textured dimples on the lubrication performance of cylinder liner in diesel engine. *Lubrication Science*, 24:293–312, 2012.
- [91] Zhang, J. and Meng, Y. Direct observation of cavitation phenomenon and hydrodynamic lubrication analysis of textured surfaces. *Tribol. Lett.*, 46:147–158, 2012.

Asociación Argentina

de Mecánica Computacional



Mecánica Computacional Vol XXXIII, págs. 129-145 (artículo completo)
Graciela Bertolino, Mariano Cantero, Mario Storti y Federico Teruel (Eds.)
San Carlos de Bariloche, 23-26 Setiembre 2014

TRIBOLOGICAL PERFORMANCE OF TEXTURED SURFACES IN THE PISTON RING/LINER CONTACT USING THE ELROD-ADAMS MODEL

Hugo M. Checo^a, Alfredo Jaramillo^a, Mohammed Jai^b and Gustavo C. Buscaglia^a

^aInst. de Ciências Matemáticas e de Computação, Universidade de São Paulo, 13560-970 São Carlos,
Brazil, <http://www.icmc.usp.br>

^bInstitut Camille Jordan, INSA de Lyon , 69621 Villeurbanne, France, <http://math.univ-lyon1.fr>

Keywords: Friction reduction, textured surfaces, piston ring, Elrod-Adams model.

Abstract. The possibility of improving the performance of lubricated surfaces through surface texturing has been a topic of intense research in the latest years. Considerable efforts in both experimental and numerical works have been made to study the effects of micro-textures in load capacity, friction and wear. In the industry it has been known for a long time that some texturing is required in the liners of combustion engines to avoid stiction with the piston rings. The numerical simulation of that problem poses a challenge in modeling the intervening phenomena (cavitation, starvation, ring dynamics) and solving it efficiently.

In this work we present numerical simulations of the piston ring/liner problem in the hydrodynamic lubrication regime using the Elrod-Adams model and a mass-conserving algorithm. Realistic values are assumed for the parameters defining the problem. The formation of cavitation bubbles and its relation with the load-carrying capacity, friction and clearance is analyzed by considering different texture configurations and shapes in one-dimensional tests. Afterwards, two-dimensional dimpled surfaces are simulated for more than a hundred different texture configurations in the hydrodynamic lubrication regime for several Stribeck numbers. A robust code accelerated by means of a multigrid implementation allowed the realization of this extensive study. Results show that friction and wear reduction are attainable by virtue of dimples of the size of the contact, although the gain decreases or disappears as the mixed lubrication regime is approached.

Original Article




Texture-induced cavitation bubbles and friction reduction in the Elrod–Adams model

*Proc IMechE Part J:
J Engineering Tribology
0(0) 1–15
© IMechE 2014
Reprints and permissions:
sagepub.co.uk/journalsPermissions.nav
DOI: 10.1177/1350650114550012
pij.sagepub.com*



Hugo M Checo¹, Alfredo Jaramillo¹, Mohammed Jai² and Gustavo C Buscaglia¹

Abstract

A thrust bearing consisting of an infinitely wide pad, subject to a constant load and sliding at constant speed on a runner with transverse sinusoidal textures is considered. The analysis method consists of time- and mesh-resolved simulations with a finite volume approximation of the Elrod–Adams model. Friction and clearance contours as functions of the texture depth and wavelength are built by performing more than 10,000 simulations. Conclusions are drawn for bearings of low, moderate and high conformity, unveiling basic mechanisms of friction reduction and global quantitative trends that are useful for texture selection.

Keywords

Textured bearings, Elrod–Adams model, friction reduction, cavitation, numerical simulation

Date received: 16 December 2013; accepted: 7 August 2014

Introduction

Textured tribological surfaces have attracted much attention of the research community lately. After a significant number of experimental and theoretical studies, the possibility of reducing friction by means of microtextures has been established, together with a basic understanding of why this happens (at least in the hydrodynamic regime).^{1–4}

That certain textures reduce friction in some hydrodynamic bearings is by no means an obvious phenomenon. Buscaglia et al.^{5,6} performed asymptotic analyses of general smooth (i.e., untextured) surfaces by introducing short-wavelength periodic perturbations of arbitrary shape and obtained that the untextured shape *always* (in the hydrodynamic regime) maximizes the load carrying capacity and minimizes the friction coefficient. This implies that, for friction reduction to take place, there exist two possibilities: It can be a consequence of a *finite* perturbation (outside the validity of asymptotic theory), or involve physical mechanisms which were not considered in the aforementioned mathematical studies, such as *cavitation*.

In a recent study, Checo et al.⁴ discussed several hundred numerical simulations and concluded that in fact *both* of the previous possibilities hold true in

textured bearings that exhibit less friction than their untextured counterparts. As had already been advanced by Etsion,³ friction reduction only occurs in high-conformity bearings, in which the surfaces are so parallel that a texture of some suitable size and depth manages to produce local cavitation.

High-conformity bearings are not infrequent in technology. Assuming a bearing of length L with a nominally planar surface opposing a surface with curvature radius R , the degree of conformity can be measured by the quotient R/L . For the compression ring of an internal combustion engine R/L is already quite high (up to 52 in diesel engines, as discussed by Gadeschi et al.²), and it is much higher for other piston rings (oil rings in particular) and for other contacts such as seals.

It was numerically shown by Gadeschi et al.² with a non-mass-conserving model, and later by Checo et al.⁴ with a mass-conserving model, that for a

¹Inst. de Ciências Matemáticas e de Computação, Univ. São Paulo, São Carlos, Brazil

²ICJ, INSA de Lyon (Pôle de Mathématiques), Villeurbanne, France

Corresponding author:
Gustavo C Buscaglia, University of São Paulo, 400, Av. Trab. São-carlense, São Carlos 13560-970, Brazil.
Email: gustavo.buscaglia@icmc.usp.br